Accessible Optogenetic Technologies for Non-human Primate Research

Devon J. Griggs

A dissertation

submitted in partial fulfilment of the

requirements for the degree of

Doctor of Philosophy

University of Washington

2022

Reading Committee:

Azadeh Yazdan-Shahmorad, Chair

Chet Moritz

Ruikang Wang

Program Authorized to Offer Degree:

Electrical and Computer Engineering

University of Washington

Abstract

Accessible Optogenetic Technologies for Non-human Primate Research

Devon J. Griggs

Chair of the Supervisory Committee:

Azadeh Yazdan-Shahmorad

Department of Electrical and Computer Engineering

Neurological diseases, disorders, and injuries have profound negative impacts on patients, communities, and nations. To address this staggering need, engineers and experts from a variety of backgrounds have dedicated themselves to studying the brain in both healthy and diseased states. Neurostimulation has been a promising avenue for generating therapies, and in recent years optogenetic stimulation has piqued the interest of researchers because of its unique neurostimulation advantages, such as cell-type specificity. To bring optogenetic neurostimulation therapies to the clinic, optogenetic research in highly translational non-human primates (NHPs) is essential. This is a growing field of research. Unique challenges have been identified by early adopters of optogenetics in NHPs, particularly at the cm^2-scales necessary to probe or stimulate multiple brain regions and understand the brain in the context of its internal interconnectivity. In this work, I describe a collection of methods designed to make optogenetic technologies more accessible to NHP researchers. My methods address NHP surgical planning for NHPs, optically-oriented electrode array design for NHPs, chronic optogenetic NHP experiments, models of optogenetic viral vector convection-enhanced delivery for NHPs, and a behavioral training system for NHPs.

Acknowledgement

First and foremost, I thank God for calling me to this work and carrying me through this challenge. Secondly, I thank my lovely wife Michaela Griggs for her endless support, my advisor Dr. Azadeh Yazdan-Shahmorad for her dedicated training, and my PhD committee members Drs. Chet Moritz, Ruikang Wang, and Nicholas Steinmetz for their guidance. Next, I thank the many colleagues and collaborators who helped to make my work a success, especially William Ojemann, Karam Khateeb, Jasmine Zhou, Dr. Ruikang Wang, Julien Bloch, Dr. Tiphaine Belloir, Aaron Garcia, Wing Yun Au, Dr. Elizabeth Buffalo, and Kelly Morrisroe. I also thank many friends, faculty, and staff from past institutions who have helped me and encouraged me to continue my studies. Of these, I especially thank, from University of Washington, Seattle: Dr. Eric Klavins, Brenda Larson, Jennifer Huberman, and Stephanie Swanson; from University of Washington, Bothell: Dr. Pierre Mourad, Dr. Hung Cao, Dr. Tadesse Ghirmai, and Sharon Meriwether; from University of Portland: Blair Pearson, Logan Adams, Dr. John Orr, Dr. Joseph Hoffbeck, Dr. Peter Osterberg, Dr. Mark Utlaut, Michele Leasor, and Kitty Harmon; from Green River Community College: Dr. Trysteen Tran, Dr. Keith Clay, Dr. Sue Critchlow, and the Running Start staff. I also thank The Boeing Company for granting me an educational leave of absence to pursue this dream, and especially Boeing's Bob Shoup and Joel Ramgattie for supporting me in my pursuit of further education. I thank my family and friends for their support, as well as the churches which have helped sustain me through my academic journey: New Life Church, Renton, WA; Mosaic, Portland, OR; and Reach Church, Kirkland, WA. Last but not least, I thank the research animals for their invaluable service and I thank my funders.

This work was funded in part by the Washington National Primate Research Center (WaNPCR, P51 OD010425), the Center for Neurotechnology (CNT, a National Science Foundation Engineering Research Center under Grant EEC-1028725), the National Institute of Neurological Disorders and Stroke of the National Institute of Health (1R01NS116464-01, R01 NS119395), the University of Washington Rushmer Innovator Fellowship, and the University of Washington GSFEI Top Scholar Recruitment Fellowship.

Contents

Table of Figures

Table of Tables

Chapter 1: Introduction

Neurological diseases, disorders, and injuries come in many varieties. These issues directly affect roughly one billion people throughout the world (WHO, 2006), and indirectly affect countless others such as family members and caregivers. Given this staggering amount of need and suffering, many physicians, scientists, engineers, and others are seeking solutions by studying the brains of humans and animals in both healthy and unhealthy states.

One promising avenue of therapy for adverse neurological conditions is neurostimulation. Electrical neurostimulation techniques such as cochlear implants and deep brain stimulation implants have been used in hundreds and tens of thousands of people, respectively (Lozano *et al.*, 2019; NIDCD, 2021). Other neurostimulation techniques such as magnetic (Chail *et al.*, 2018) and ultrasonic (Olmstead *et al.*, 2018; Wang *et al.*, 2020) stimulation are at varying stages of development. In 2005, a novel neurostimulation technology was introduced which involves optical stimulation of genetically altered neurons (Boyden *et al.*, 2005), a technology now referred to as optogenetics.

Optogenetics is a powerful tool for neuroscience because it has a number of advantages over other neurostimulation techniques. Optogenetics offers cell type specificity, spatial and temporal control, both excitatory and inhibitory modulation of neurons, and artifact-free stimulation during electrophysiological recordings (Yizhar *et al.*, 2011). Since its original demonstration, the optogenetic toolbox has been widely expanded and used to study neural systems in a collection of non-human species (Yizhar *et al.*, 2011), and recently the first neurotherapeutic use of optogenetics in a human was published (Sahel *et al.*, 2021), which sets the stage for future optogenetic therapies in humans.

Optogenetics has developed alongside a growing appreciation for the link between the brain's functionality and neuronal interconnectivity. For example, a stroke in one region of the brain can cause malfunction in distant regions of the brain, a process called diaschisis (Carrera and Tononi, 2014). Given that simultaneous study of multiple brain regions is paramount for the brain and its conditions to be understood comprehensively, development of large-scale neural interfaces is crucial. However, optogenetic implementations of such interfaces are not trivial: For optogenetics to be employed in cortical regions at these large-scales, the necessity of equally large regions of optical access through the cranium becomes apparent. Recent development of large-scale optical techniques for rodents has been encouraging (Renz *et al.*, 2020), but more work is needed for large-animal models.

To spur the development of human optogenetic neurotherapies, optogenetic research in non-human primates (NHPs) is essential (Camus *et al.*, 2015; Harding, 2017; Mitchell *et al.*, 2018). NHPs are critical for translational medicine because they are evolutionary similar to humans and they can be trained to perform complex cognitive and behavioral tasks. Additionally, individual NHPs can be studied for many years, making them more relevant to long-term human neurological conditions than typical neuroscience rodent species. This niche field of optogenetic NHP research is promising (Tremblay *et al.*, 2020), yet nascent (Bliss-Moreau, Costa and Baxter, 2022). Indeed, the progress of research has been hindered by the challenges that come with optogenetics in NHPs. In comparison with popular neuroscientific animal models like rodents, NHPs are especially precious and scarce resources for the scientific community. NHPs have slow reproduction rates, which make transgenic animal lines impractical. NHPs also can have large brains, which means that technologies need to cover large neural areas to probe or stimulate multiple brain regions. This poses a particular challenge for chronic optical experiments, as is made apparent by the paucity of large-scale optogenetic studies in NHPs (Yazdan-Shahmorad *et al.*, 2015; Azadeh Yazdan-Shahmorad *et al.*, 2016; S L Macknik *et al.*, 2019; Rajalingham *et al.*, 2021). Despite the tantalizing research

remaining to be performed with large-scale optogenetics in NHPs, research progress will be hindered without technological developments bringing greater accessibility to the field.

In this work, I aim to bolster large-scale optogenetic research in NHPs by proposing methods designed to be accessible to NHP researchers. I begin in Chapter 2, which details the surgical planning techniques I developed to aid researchers in preparing for optogenetic surgeries for NHPs. I mentored an undergraduate researcher (William K. S. Ojemann) through multiple steps of visualizing the surgical planning process which will make surgical planning more accessible to NHP researchers. I heavily contributed to modeling NHP skulls and craniotomies, which was the most computationally-oriented part of the work and proved to be a crucial building-block to the cranial chamber design process I present in Chapter 4. This work was performed in collaboration with the lab of Dr. Stephen Macknik, from SUNY Downstate, as well as other members of the lab of Azadeh Yazdan-Shahmorad, my advisor. This work is peer-reviewed and published in *Journal of Visualized Experiments*: my undergraduate mentee is first author, and I am second author (Ojemann *et al.*, 2020).

In Chapter 3, I present my novel electrocorticography (ECoG) array designed to provide large-scale (>1 cm^2) electrophysiological and optical access to the brain. This array is designed to replace the opaque native dura mater, thus placing the electrodes directly on the surface of the brain, and is called a multi-modal artificial dura (MMAD). I designed the MMAD in close collaboration with Ripple Neuro, our industry partner, who printed the MMADs. The MMAD is commercially available, which contributes to my work's accessibility to the community. I led the validation efforts of the MMAD in both bench-side and acute *in vivo* NHP experiments. This work included optical and electrical characterization, spectral analysis of cortical NHP electrophysiology, and analysis of electrical stimulation. This work also included performing optical coherence tomography angiography (OTCA) through the MMAD *in vivo*, in collaboration with Dr. Ruikang Wang lab, from University of Washington, which further validated the large-scale optical access to the cortex provided by the MMAD. I also collaborated with other members of the lab of Dr. Azadeh Yazdan-Shahmorad. I first authored this work, which has been peer-reviewed and published in the *Journal of Neural Engineering, Special Issue "Neuroelectronic Interfaces"* (Griggs *et al.*, 2021a). While not presented in this dissertation, I also was a partial author on a project I supported that used my MMAD to develop and study an acute photothrombotic cortical lesioning technique in NHPs (Khateeb *et al.*, 2022), which speaks to my technology's applicability to study adverse neural conditions.

In Chapter 4, I present my work leading the development and implementation of a novel, large-scale optogenetic cortical interface for chronic NHP experimentation. This work builds upon the surgical preparation methods presented in Chapter 2, and chronically implements the MMAD presented in Chapter 3. In Chapter 4, I present methods for molding the MMAD into a chronically implantable form, a cranial chamber with designs based off the skull modeling methods presented in Chapter 2, surgical implantation steps for the chamber and MMAD, and cleaning processes for chronic maintenance. I also present components designed to support electrophysiological data collection and optogenetic stimulation, and I present data analysis suggesting that I have successfully performed large-scale optogenetic modulation in NHP cortex. I present data showing large-scale (tens of mm^2) optogenetic expression across NHP cortex produced with convection-enhanced delivery (CED) methods similar to that which I have published (Karam Khateeb, Griggs, *et al.*, 2019). I also demonstrate 3+ months of optical access to the cortex, which had previously not been achieved with an electrode array in NHPs. Importantly, the methods presented in this work are designed to be approachable to NHP researchers who may have modest engineering expertise, and this work is compatible with a photothrombotic cortical lesioning method that I participated in developing (Khateeb *et al.*, 2022). While not yet fully published, this chapter is built off of three peer-reviewed conference publications which I first-authored (Griggs, Khateeb, Philips, Chan, Ojemann, Yazdan-Shahmorad, *et al.*, 2019; Griggs, Belloir and Yazdan-Shahmorad,

2021; Griggs, Bloch, *et al.*, 2022), and this chapter is representative of a manuscript I am preparing, as first-author, for submission to a peer-reviewed journal in 2022. This work was performed in collaboration with other members of the lab of Dr. Azadeh Yazdan-Shahmorad. While not presented in this dissertation, I am also partial author on a manuscript under review, which reviews large-scale multimodal surface neural interfaces for NHPs. This is an invited paper for *iScience* that outlines advancements and opportunities relevant to my work.

Chapter 5 is based on an infusion process known as convection enhanced delivery (CED). CED is a pressure-based approach of spreading optogenetic viral vectors or other agents throughout large regions (hundreds of µL) of the brain or other soft tissues. I present my work leading the development of methods relevant to genetically altering neural tissue in the brain for optogenetics. This work is a quantitative, data-driven extension of the qualitative, agar-based infusion modeling presented in Chapter 2. My lab had previously collected live *in vivo* magnetic resonance imaging (MRI) CED data of viral vectors in NHP brains, and I led the development of an agar-based method to quantitively replicate the data bench-side. Additionally, this chapter presents post-operative MRI methods of infusion validation, as led by my co-first author (Aaron D. Garcia). I contributed to the generation of these data and I led the efforts of modifying my agar model to account for post-operative effects on the infused agent. Collectively, this work is designed to provide researchers quantitative and accessible bench-side methods of planning infusion protocols specific to their needs, practicing CED infusions prior to surgery, and validating CED results post-surgery. I co-first authored this work, which is published in *Pharmaceutics, Special Issue "Brain-Targeted Drug Delivery"* (Griggs, Garcia, *et al.*, 2022). While not presented in this dissertation, I have also made other efforts to disseminate the CED technology: I am co-first author on an invited book chapter titled "Convection enhanced delivery of viral vectors" for *Vectorology for Optogenetics and Chemogenetics,* a book which is now with the publishers at Springer Nature; and I am second author on a peer-reviewed journal paper explaining methods for CED in NHPs (Karam Khateeb, Griggs, *et al.*, 2019).

Chapter 6 is inspired by a need to train NHPs to perform behavioral tasks related to brain areas of interest. In this chapter, I present my work proposing an automated cage-side training system (ACTS) for NHPs. I led the development and implementation of ACTS, which provides an inexpensive and accessible method for researchers to train NHPs to perform behavioral tasks without removing the NHPs from their cages. This is more convenient for researchers, who would traditionally transport NHPs to an experimental rig for training, and this is convenient for the NHPs, who get to stay in a familiar environment while training. In this work I detail the methods for building and running ACTS and I demonstrate its utility in training NHPs. I first-authored this work, which has been peer-reviewed and published in the *Journal of Neuroscience Methods* (Griggs *et al.*, 2020).

To conclude, Chapter 7 comments on future directions of my work.

Chapter 2: A MRI based toolbox for neurosurgical planning in non-human primates

This chapter is representative of work which is complete and published. Reprinted with permission. Please cite the final published version of this work:

> Ojemann W, **Griggs DJ**, Ip Z, Caballero O, Jahanian H, Martinez-Conde S, Macknik S, Yazdan-Shahmorad A. 'A MRI-based toolbox for neurosurgical planning in nonhuman primates,' *J. Vis. Exp.* (161), e61098, doi:10.3791/61098 (2020).

2.0 Abstract

In this paper, we outline a method for surgical preparation that allows for the practical planning of a variety of neurosurgeries in NHPs solely using data extracted from magnetic resonance imaging (MRI). This protocol allows for the generation of 3D printed anatomically accurate physical models of the brain and skull, as well as an agarose gel model of the brain modeling some of the mechanical properties of the brain. These models can be extracted from MRI using brain extraction software for the model of the brain, and custom MATLAB code for the model of the skull. The preparation protocol takes advantage of state-of-the-art 3D printing technology to make interfacing brains, skulls, and molds for gel brain models. The skull and brain models can be used to visualize brain tissue inside the skull with the addition of a craniotomy in the custom code, allowing for better preparation for surgeries directly involving the brain. The applications of these methods are designed for surgeries involved in neurological stimulation and recording as well as injection, but the versatility of the system allows for future expansion of the protocol, extraction techniques, and models to a wider scope of surgeries.

2.1 Introduction

Primate research has been a pivotal step in the progression of medical research from animal models to human trials (Phillips *et al.*, 2014; Stephen L. Macknik *et al.*, 2019). This is especially so in the study of neuroscience and neural engineering as there is a large physiological and anatomical discrepancy between rodent brains and those of non-human primates (NHP) (Seok *et al.*, 2013; Phillips *et al.*, 2014; Stephen L. Macknik *et al.*, 2019). With emerging genetic technologies such as chemogenetics, optogenetics, and calcium imaging that require a genetic modification of neurons, neural engineering research studying neural function in NHP's has gained special attention as a preclinical model for understanding brain function (Han, 2012; May *et al.*, 2014; Yazdan-Shahmorad *et al.*, 2015; Ledochowitsch *et al.*, 2015; Acker *et al.*, 2016; Azadeh Yazdan-Shahmorad *et al.*, 2016; A Yazdan-Shahmorad, Silversmith and Sabes, 2018; Yao and Yazdan-Shahmorad, 2018; Yazdan-Shahmorad, Silversmith, *et al.*, 2018; Yazdan-Shahmorad, Tian, *et al.*, 2018; Ju *et al.*, 2018; Griggs, Khateeb, Philips, Chan, Ojemann, Yazdan-Shahmorad, *et al.*, 2019; Karam Khateeb, Griggs, *et al.*, 2019; Stephen L. Macknik *et al.*, 2019). In most NHP neuroscience experiments, neurosurgical measures are required for the implantation of various devices such as head posts, stimulation and recording chambers, electrode arrays and optical windows (Jackson, Mavoori and Fetz, 2006; Lucas and Fetz, 2013; May *et al.*, 2014; Ledochowitsch *et al.*, 2015; Yazdan-Shahmorad *et al.*, 2015; Acker *et al.*, 2016; Azadeh Yazdan-Shahmorad *et al.*, 2016; Yazdan-Shahmorad, Tian, *et al.*, 2018; Ju *et al.*, 2018; Yazdan-Shahmorad, Silversmith, *et al.*, 2018; Griggs, Khateeb, Philips, Chan, Ojemann, Yazdan-Shahmorad, *et al.*, 2019).

Current NHP labs use a variety of methods that often include ineffective practices including sedating the animal in order to fit the legs of a head post and approximate the curvature of the skull around the craniotomy site. Other labs fit the head post to the skull in surgery or employ more advanced methods of gaining the necessary measurements for implantation like analyzing an NHP brain atlas and magnetic

resonance (MR) scans to try to estimate skull curvatures (Yazdan-Shahmorad *et al.*, 2015; Azadeh Yazdan-Shahmorad *et al.*, 2016; Karam Khateeb, Griggs, *et al.*, 2019; Stephen L. Macknik *et al.*, 2019). Neurosurgeries in NHPs also involve fluid injections, and labs often have no way to visualize the projected injection location within the brain (May *et al.*, 2014; Acker *et al.*, 2016; Ju *et al.*, 2018; Yazdan-Shahmorad, Tian, *et al.*, 2018; Stephen L. Macknik *et al.*, 2019) relying solely on stereotaxic measurements and comparison to MR scans. These methods have a degree of unavoidable uncertainty from not being able to test the physical compatibility of all the complex components of the implant.

Therefore, there is a need for an accurate non-invasive method for neurosurgical planning in NHPs. Here, we present a protocol and methodology for the preparation of implantation and injection surgeries in these animals. The whole process stems from MRI scans, where the brain and skull are extracted from the data to create three dimensional (3D) models that can then be 3D printed. The skull and brain models can be combined to prepare for craniotomy surgeries as well as head posts with an increased level of accuracy. The brain model can also be used to create a mold for the casting of an anatomically accurate gel model of the brain. The gel brain in combination alone and in combination with an extracted skull can be used to prepare for a variety of injection surgeries. Below we will describe each of the steps required for the MRI based toolbox for neurosurgical preparation.

2.2 Protocol

All animal procedures were approved by the University of Washington Institute for Animal Care and Use Committee. Two male rhesus macaques (monkey H: 14.9 kg and 7 years old, monkey L: 14.8 kg and 6 years old) were used.

2.2.1. Image acquisition

We transported the monkey to a 3T MRI scanner and placed the animal in an MR-compatible stereotaxic frame. We record the standard T1 (flip angle = 8°, repetition time/ echo time = 7.5/3.69 s, matrix size = 432 x 432 x 80, acquisition duration = 103.7 s, Multicoil (Table of Materials), number of averages = 1, slice thickness = 1 mm) anatomical MR images. We selected MRI parameters to maximize separation between skull and brain, which was helpful with skull isolation describe in subsequent steps.

2.2.2. Brain extraction

We loaded the T1 Quick Magnetization Prepared Rapid Gradient Echo (MPRAGE) scan. To extract the brain, we used the Extract Brain (BET) plugin. We performed the extraction at an intensity threshold around 0.5− 0.7 and set the threshold gradient value to 0. We repeatedly use the extraction function at successively lower intensity thresholds until the scan contained only the cortical anatomy (Figure 1B). This was an iterative process because the software is not designed for NHP brains and thus extraction is not precise. Next we applied a threshold to the ROI and selected the option for Shrink Wrap and 3D to create a bitmap of the brain. This converted the volume to binary bits from a gradient, which streamlines future model generation processes. We chose a threshold around 600 based on gray matter values to isolate the brain from the surrounding tissue, then formed a bitmap. Next we created a surface using the previous threshold value. The resulting surface was used as a reference for adjusting the threshold value to produce the highest quality representation of the targeted anatomy (Figure 1C). We saved the extracted brain ROI as a .nii or .nii.gz file for use in creating the model of the brain.

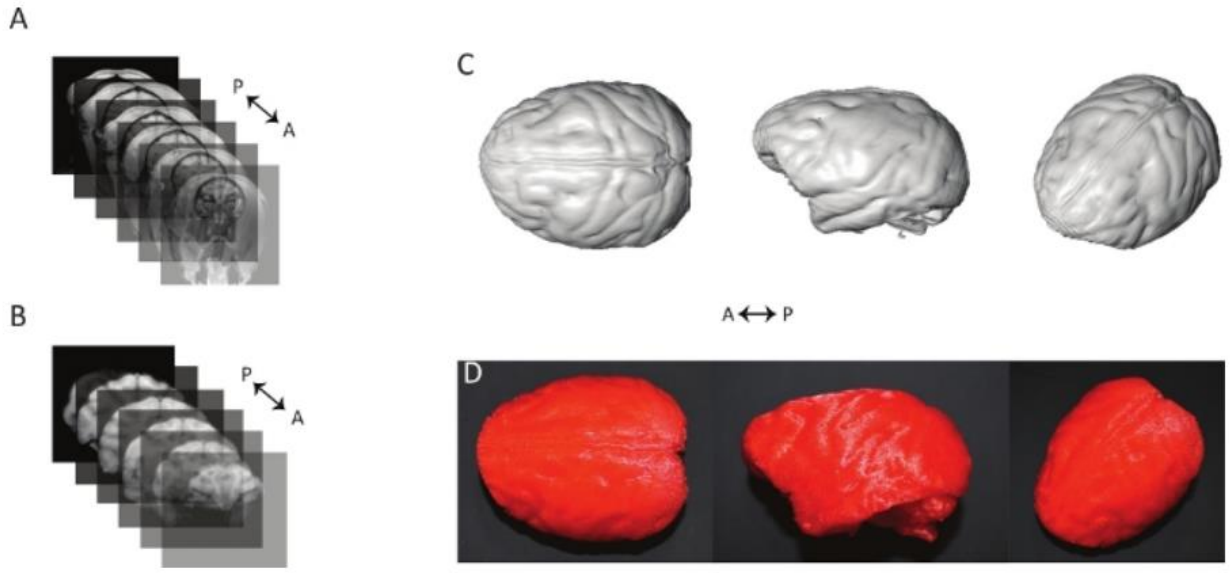

Figure 2.1: Models of extracted brain. (A) Layered series of T1-QuickMPRAGE coronal slices of the brain of Monkey H. (B) Layered series of MR slices of the extracted brain of Monkey H using the BET plugin and Mango software as outlined in the Methods section. (C) Axial, sagittal, and skewed view of a model of the gray matter of Monkey H created using the surface building functionality in Mango. (D) Axial, sagittal, and skewed view of a 3D printed model of the gray matter of Monkey H created using a Dremel 3D45 extruding printer. Reprinted from (Ojemann *et al.*, 2020) *with permission.*

2.2.3. Brain modeling

We loaded the extracted brain saved in the .nii or .nii.gz file type into medical image processing software. We adjusted the threshold range sliders so the portion of the bitmap containing the brain was highlighted in all three slices. Note that when loading a bitmap, adjusting both sliders to a value of 1 selected the whole brain. Once applied, we created a volume from the bitmap file generated previously , and saved the file in .stl format. To further modify the brain model, we loaded the .stl file as a Graphics body in computer aided design software. This was a slow process due to the complexity of the imported mesh brain surface. Once imported, we suppressed unnecessary Graphic features until only the features containing the brain are remaining in the file. Finally, we saved the remaining file as a .prt for further manipulation and as an .stl for 3D printing.

2.2.4. Brain molding

Load the extracted brain model from section 3 to the computer aided design software by opening the .prt file. Under the features section of the insert menu, select Convert to Mesh body. Select the Graphic body of the brain and convert it. To create a right and left mold of the full brain, click the Sketch button and select the top plane as the sketch plane. Draw a rectangle containing either the entirety of the right or left hemisphere of the brain. Select the extrude boss/base feature while in the sketch and extrude a cubic rectangle to contain the top part of the brain. The cube may have to be extruded in two directions in order to contain the entire hemisphere. This is because the zero point, where the plane of extrusion is located, may fall inside the brain model. Extruding in both directions ensures that the mold will encompass the whole volume of interest. To create the negative space, subtract the model of the brain from the newly extruded cube using the Combine feature and selecting the subtract option. Under the features section of the 'insert' menu, select Convert to Mesh body. Select the extruded cube in the Solid bodies folder and convert it. Repeat for the other hemisphere of the brain (left or right) and save the resulting files as a .stl for 3D printing and a .prt for further manipulation.

To create a right and left mold of the upper half of the brain, we extruded a cuboid containing either the entirety of the right or left hemisphere of the brain. We offset the extrusion up to a distance where there were no overhanging contours in the brain anatomy, capturing just the upper anatomy. Then we converted the brain and the extruded cube to separate Mesh bodies. To create the negative space, we subtracted the model of the brain from the newly extruded cube. To complete the mold design, we extruded a solid body approximately 5 mm thick to completely enclose the subtracted brain anatomy in the mold. We repeated the above steps for the other hemisphere of the brain and saved the resulting files as a .stl for 3D printing and a .prt for further manipulation. By changing the dimensions and location of the cuboid and following the same protocol, we created molds that contain different parts of the brain. For 3D printing, we used ~70% infill density and increased the thickness of the outer shell of the print in order to minimize leakage of the molding material. We filled gaps and defects in the print with nail polish or another binding agent.

2.2.5. Skull modeling

We imported the QUICK MPRAGE MRI into the matrix manipulation software as a DICOM file. If the DICOM file was divided into several 2D coronal frames, we combined all frames into a 3D matrix. We created a binary mask by thresholding the 3D matrix and we adjusted the threshold such that the skull anatomy was captured by the mask. The mask contained four distinct layers. From the outside in, the layers will be referred to as “outside”, “musculature”, "skull”, and “brain” for the purposes of this paper. At this stage, “outside” and “skull” were 0’s in the mask, and “musculature” and “brain” were 1’s.

To remove the “musculature” layer, we processed each frame from the 3D mask separately by iteratively grabbing a 2D slice from the mask. For each frame, we selected 0 pixels from the corners of the frame in the “outside” layer as the “seed”. Then we searched neighboring 0’s until encountering a 1 pixel. We continued searching until no more 0’s could be found, and then converted all connected 0’s to 1’s. Some skull information was be lost during this step. To mitigate the information loss, we performed the previous step in all three dimensions of the data, and kept the results separate. At this point both “outside” and “musculature” are 1’s, and will be collectively referred to as “outside.” Next we inverted the values of the mask such that “skull” was 1’s and “outside” and “brain” were 0’s. We refer to 1’s that are touching each other in each mask as “objects,” and we created an index of all objects in each mask. For each mask, we removed all objects except for the one containing the most voxels by setting the values of the smaller objects to 0’s. Then we added the masks created from each pass together.

Next, we scaled the brain to a consistent resolution. From the DICOM header, we compared the step size between each frame of the MRI to the dimensions of each pixel. If these values were different, we defined a scale factor to compensate for the difference in resolution between step size and pixel size for each voxel. In our case, each frame was 1 mm apart, and the pixel dimension was 0.33 mm x 0.33 mm, and thus we selected a scale factor of 3. We added additional empty voxels to the 3D mask until the lowest resolution dimension of the mask was larger by a factor defined by the scale factor. We linearly interpolated values in the mask until the mask filled the new space. Finally, we export skull as an .stl file for 3D printing.

2.2.6. Craniotomy creation in the 3D skull model

Using the MRI file, we manually identified the approximate location of the craniotomy from anatomical landmarks found in the macaque brain atlas (e.g., central sulcus)(Paxinos, Petrides and Toga, 2008). We saved the frame number as the z coordinate of the center of the craniotomy. We saved the x and y coordinates of a single point on this frame for the craniotomy center. Nex we converted the radius of the intended craniotomy from mm to voxels using the information in the DICOM header. Using the point previously specified as a centerpoint, we set all voxels within the radius to zero in the mask. We did not

perform multiple craniotomies, but if we had had a need we would have repeated the steps for each unique craniotomy. Finally, we exported the skull as an .stl for 3D printing.

2.2.7. 3D printing

We produced physical prototypes with two types of 3D printers. For the following specifications, all 3D printer and printing software settings were default unless otherwise mentioned. To print the prototypes and molds, we used a standard PLA printer and created the G-Code necessary for the printer with the following printer and software settings: inner density >50% (this is especially important for the molds as they must hold liquid), fast honeycomb internal fill pattern, rectilinear external fill pattern, plate temperature = 50 °C, and extruder temperature = 230 °C. To print higher fidelity models of the brain and skull we used an industrial-grade printer to make a combined print of acrylonitrile butadiene styrene (ABS) for the model and a dissolvable support material. In this case, we created the G-Code used the following printer settings: fill style Sparse - High Density. All other settings were be automatically set to the appropriate default setting. We dissolved the model in support solvent for ~12 h after printing. After 3D printing the molds, we patched any visible holes with nail polish to guarantee a tighter seal. The 3D printed brain and skull models could be combined by inserting the brain model into the open bottom of the skull. Removing the eye anatomy eased the placement of the brain model without losing important skull curvature information. When placed inside the skull, the brain naturally aligned to the anatomically correct position.

2.2.8. Preparation of agarose

We mixed the agar powder and locust bean gum powder in a 1:4 ratio by mass, then combined the powder mixture with 1x phosphate buffered solution to a 0.6% concentration solution in an Erlenmeyer flask. Concentrations used by other labs fall in a range of 0.5%-0.6% (Chen *et al.*, 2004; M T Krauze *et al.*, 2005). We set the microwave to max power and placed the flask containing the solution in the microwave for 2 min. When the solution began to bubble, we stopped the microwave and timer, removed the flask, and swirled vigorously. Then we set the flask back in microwave and resumed the microwave and timer. The purpose was to heat the solution without reducing the volume significantly due to evaporation during boiling. We repeated this process until the two minutes was complete, then we removed the flask and maintained swirling to prevent the solution from setting in the flask. We ran cold water on the outside of the flask to cool the solution while swirling. We cooled the solution until the outside of the flask was hot to the touch, yet tolerable and safe, to prevent the solution from deforming the plastic mold in the following steps. We swirled the flask while transporting the solution to the mold to avoid premature hardening.

2.2.9. Agarose molding

The agarose molding process described here was the same for the full hemisphere and upper half hemisphere molds. We poured the agarose solution into one of the brain molds until full while continuing to swirl the remaining solution in the flask. We monitored the level of solution in the mold for leaks and we refilled the mold as necessary. We allowed the solution in the mold to sit unperturbed at room temperature until the solution had set and hardened into a solid. While wait times may vary depending on the volume of solution and other factors, 2 h was found to be a reliable wait time. We used a spatula to gently remove the gel model from the mold. We were strategic with the location of spatula insertion into the mold in order to prevent potential deformations to the surface of the mold. To slow the natural

evaporation process and exposure to biological agents, we placed the gel model in a sealed container in a refrigerator when not in use.

2.2.10. Injection into agarose gel model

We prepared the pump for infusion and fixed it in a stereotaxic arm on a stereotaxic frame. We positioned the pump to the correct injection trajectory and location normal to the surface of the transparent gel model. We filled a 250 µL syringe with DI water and mounted the syringe onto the pump. Before drawing any dye, we completely filled the injection cannula with DI water. This ensured when the dye was drawn up through the cannula there was no compression or expansion of air by the plunger that might impact the injection volume. We used the pump driver to withdraw the food coloring into the syringe to the target volume for injection. We injected the food coloring slowly until a small bead formed at the tip of the cannula to prevent air bubbles from being injected into the gel, and we dried the bead off the tip of the cannula. After positioning the gel model under the cannula, we lowered the cannula until the tip touched the surface of the gel model. We noted the measurements on the stereotaxic arm and lowered the cannula into the gel model quickly and smoothly to the target injection depth and ensured that the surface of the gel sealed around the cannula. Next, we ran the pump and observe the spread of the food coloring until the target volume was injected. We started with a flowrate of 1 µL/min and increase to 5 µL/min with 1 µL/min steps every minute. The spread of the food coloring in the gel was an approximation of the spread of a viral vector in the brain. Once complete, we removed the cannula from the gel quickly and smoothly. We captured images of the spread of the food coloring with a camera and measured the dimensions of the embolism to approximate the ellipsoid volume of the injection.

2.3 Representative results

The manipulation and analysis of MRIs scans as a preoperative craniotomy planning measure has been used successfully in the past (Azadeh Yazdan-Shahmorad *et al.*, 2016; Yazdan-Shahmorad, Tian, *et al.*, 2018; Karam Khateeb, Griggs, *et al.*, 2019; Stephen L. Macknik *et al.*, 2019). This process, however, has been greatly enhanced by the addition of our 3D modeling of the brain, skull, and craniotomy. We were able to successfully create an anatomically accurate physical model of the brain that reflected the area of interest for our studies (Figure 1). We were similarly able to create an anatomically accurate physical model of the primate skull extracted from the MR images (Figure 2).

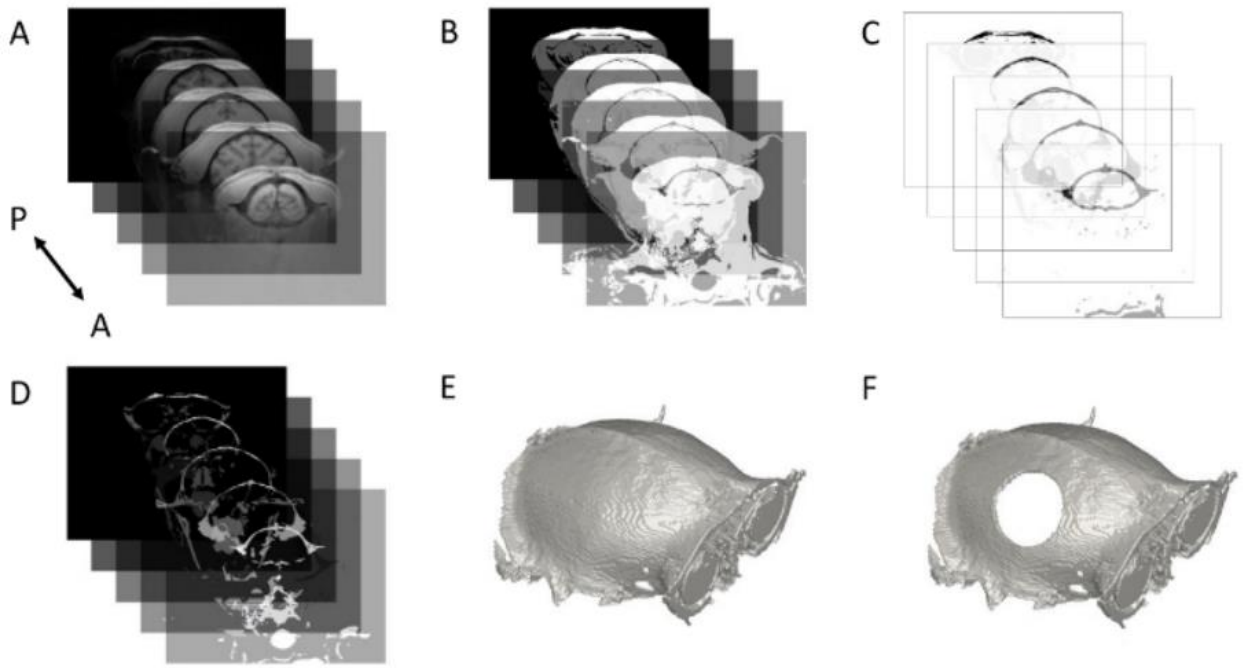

Figure 2.2: Skull extraction. (A) Layered series of T1-QuickMPRAGE coronal slices of the brain of Monkey H. (B) Layered series of binary mask after simple thresholding MR slices. (C) Layered series of binary mask after removing "musculature layer". (D) Layered series of binary mask of skull after processing as outlined in the Methods section. (E) 3D model generated from binary mask. (F) 3D model with simulated craniotomy removed. Reprinted from (Ojemann *et al.*, 2020) *with permission.*

The two physical models of the skull and brain combined with a tight interference fit, validating the accuracy of the two models relative to each other, and legitimizing the extrapolated MRI analysis data (Figure 3A-B). With the combined model we were able to insert a craniotomy into the skull prior to printing and visualize the predicted anatomy in the craniotomy (Figure 3). The accuracy of the predicted anatomy in the craniotomy was validated through a comparison of the physical model and the predicted craniotomy from MRI analysis (Figure 3B). Additionally, we were able to combine all of the parts of our example interface and evaluate the geometry of the various components in relation to the skull and brain (Figure 3C-D).

In order to test the skull model, a physical model of the skull of Monkey L was extracted using the methods outlined above and 3D printed to plan for a head post implantation surgery. The feet of the head post were then manipulated and fitted to the curvature of the skull at the location of the implantation (Figure 3E). As a result of the preoperative fitting of the head post, the surgery time was reduced from approximately 2.5 hours to 1 hour (216% faster) from opening to implantation, greatly reducing the risk of operative complications (Cheng *et al.*, 2018).

By manipulating the 3D model of the brain in SolidWorks, we were able to create a mold that accurately reflected the anatomy of both the printed brain, and the brain model extracted from the MRI (Figure 4A-C). This mold was used to cast an agarose mixture model of the brain (Figure 4D,E). Using these molds of the brain, we were able to inject in different areas of the brain and estimate the volume of the infusion of an injection procedure modeled with a yellow dye. The half-hemisphere gel model of the brain was successfully used to capture a clear view of the spread of the dye in a model virus injection, allowing us to measure an approximate volume of the dye over time as it was injected (Figure 5A). Injection of dye into the brain model was combined with a 3D printed skull to model an example viral vector injection surgery (Figure 5B,C). This was combined with an electrocorticography array placement on top of the

injection to guide the implantation in preparation for surgery (Ledochowitsch *et al.*, 2015; Azadeh Yazdan-Shahmorad *et al.*, 2016).

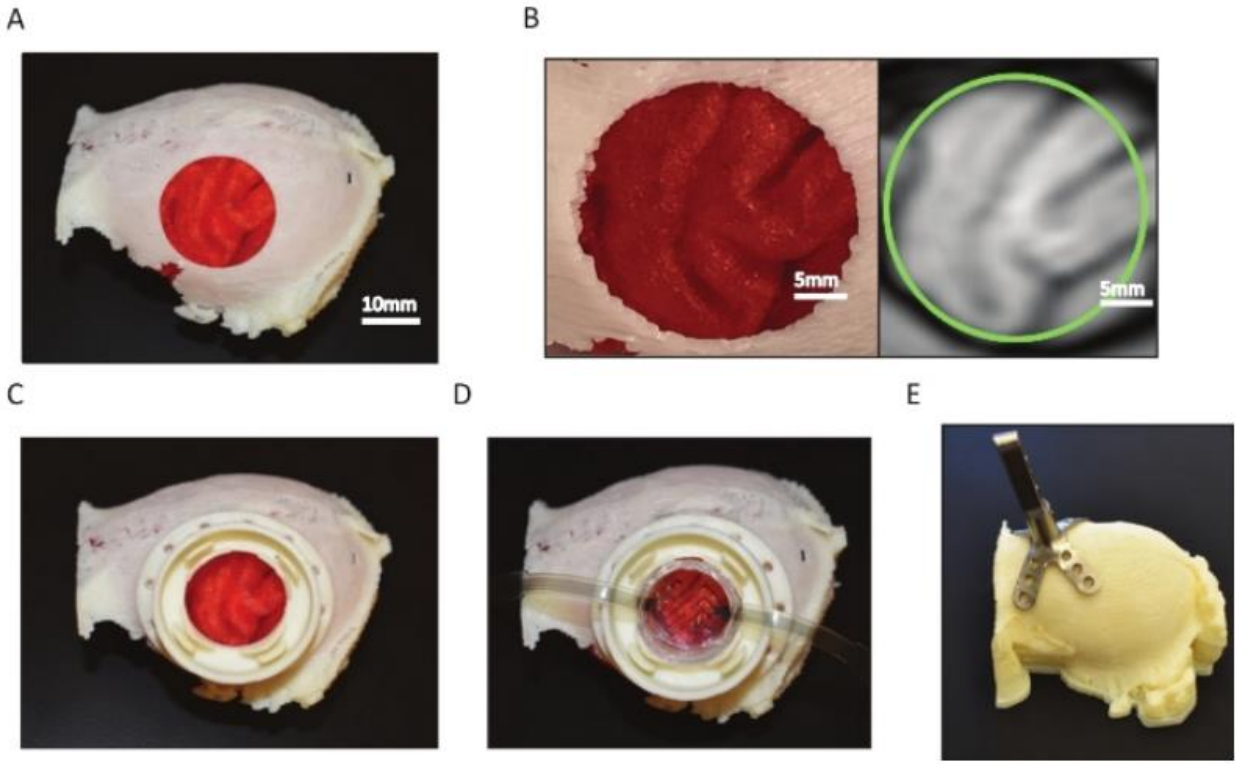

Figure 2.3: Surgical preparation using 3D printed prototypes. (A) Combination of the 3D printed brain extracted with Mango inside of a 3D printed skull extracted from MRI of Monkey L as outlined in the Methods section. (B) Comparison of craniotomy targeting between our 3D models and MR planning in Monkey L. (C,D) An example of using our toolbox to prepare for chamber (C) and array (D) implantation[15] . (E) 3D printed model of the skull of Monkey L used for pre-bending the head-post prior to surgery. Reprinted from (Ojemann *et al.*, 2020) *with permission.*

2.4 Discussion

This article describes a toolbox for preparation for neurosurgeries in NHPs using physical and CAD models of skull and brain anatomy extracted from MR scans.

While the extracted and 3D printed skull and brain models were designed specifically for the preparation of craniotomy surgeries and head post implantations, the methodology lends itself to several other applications. It is important to note that the MRI acquisition process required some troubleshooting as it is critical to set the correct parameters as outlined in the protocol. As described before, the physical model of the skull allows for pre-bending of the head post before surgery, which creates a good fit with the skull. Moreover, the extracted skull extraction technology from MRI can be used to generate of a 3D designed head post with a higher fidelity to the skull anatomy.

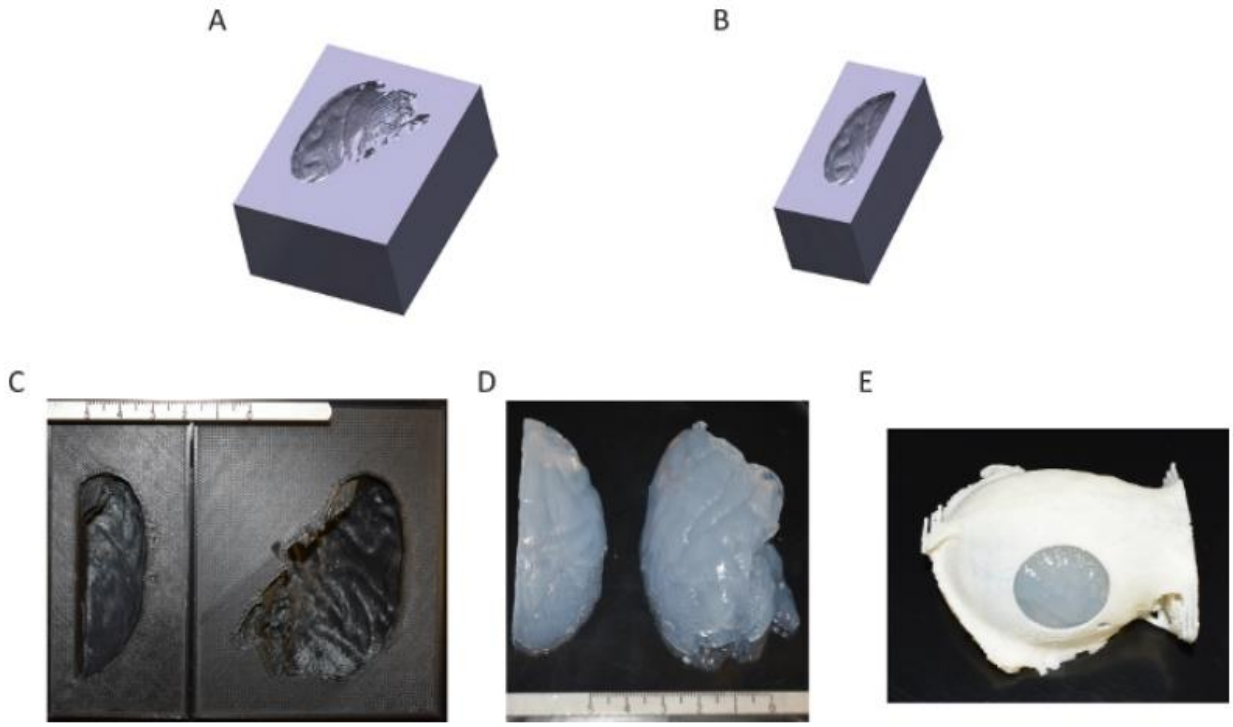

Figure 2.4: Gel brain modeling. (A, B) 3D model of the mold for Monkey H. (C) 3D printed molds from A and B. Pictured left is a mold used to create the upper portion of the right hemisphere. Pictured right is a mold to create the right hemisphere (D) Agarose models of the upper portion of the right hemisphere (left) and the whole right hemisphere (right). (E) Agarose model of the right hemisphere placed inside of a 3D print of an extracted skull from Monkey L, demonstrating the accurate representation of the brain and craniotomy. Reprinted from (Ojemann *et al.*, 2020) *with permission.*

While CT imaging is traditionally a better modality for skull extraction, in our proposed method, the brain and skull anatomy come from the same imaging modality, which could contribute to enhanced anatomical consistency between the bone and soft-tissue models. This anatomical consistency could enhance precision and ensure that the craniotomy will cover the cortical region of interest and that all the implanting components, such as stimulation and recording chambers, fit the skull curvature.

It is important to carefully consider the parameters used to obtain the MRI. Low resolution MRIs will present significant obstacles to cleanly segment the skull from surrounding soft tissue. Specifically, skull segmentation requires that the dura mater has a minimal footprint on the MRI.

This is supported by extant studies that quantitatively compared MRI-extracted skull topography to extractions from other scan types (Michikawa *et al.*, 2017; Soliman *et al.*, 2017). Other work in the field has outlined methods for the creation of models and 3D printed prototypes for head post implantation (Overton *et al.*, 2017; Blonde *et al.*, 2018), but they do not use solely MR scans to create an adaptable model for the preparation for both head posting and craniotomy. Previous work in the field of brain extraction and skull stripping offers alternatives to the widely available BET brain extraction used in this protocol (31434923). Similarly, skull extraction custom scripts exist, however, they require the manual removal of non-skull voxels compared to our completely automated protocol (30232039). While here we show only a few examples, these tools are applicable to a variety of other surgeries such as electrode and chamber implantations in NHPs (Jackson, Mavoori and Fetz, 2006; Nishimura *et al.*, 2013; Ledochowitsch *et al.*, 2015; Seeman *et al.*, 2017; Ju *et al.*, 2018; Yazdan-Shahmorad, Tian, *et al.*, 2018; Griggs, Khateeb,

Philips, Chan, Ojemann, Yazdan-Shahmorad, *et al.*, 2019; Stephen L. Macknik *et al.*, 2019), as well as other animal models (Schweizer-Gorgas *et al.*, 2018; Sedaghat-Nejad *et al.*, 2019).

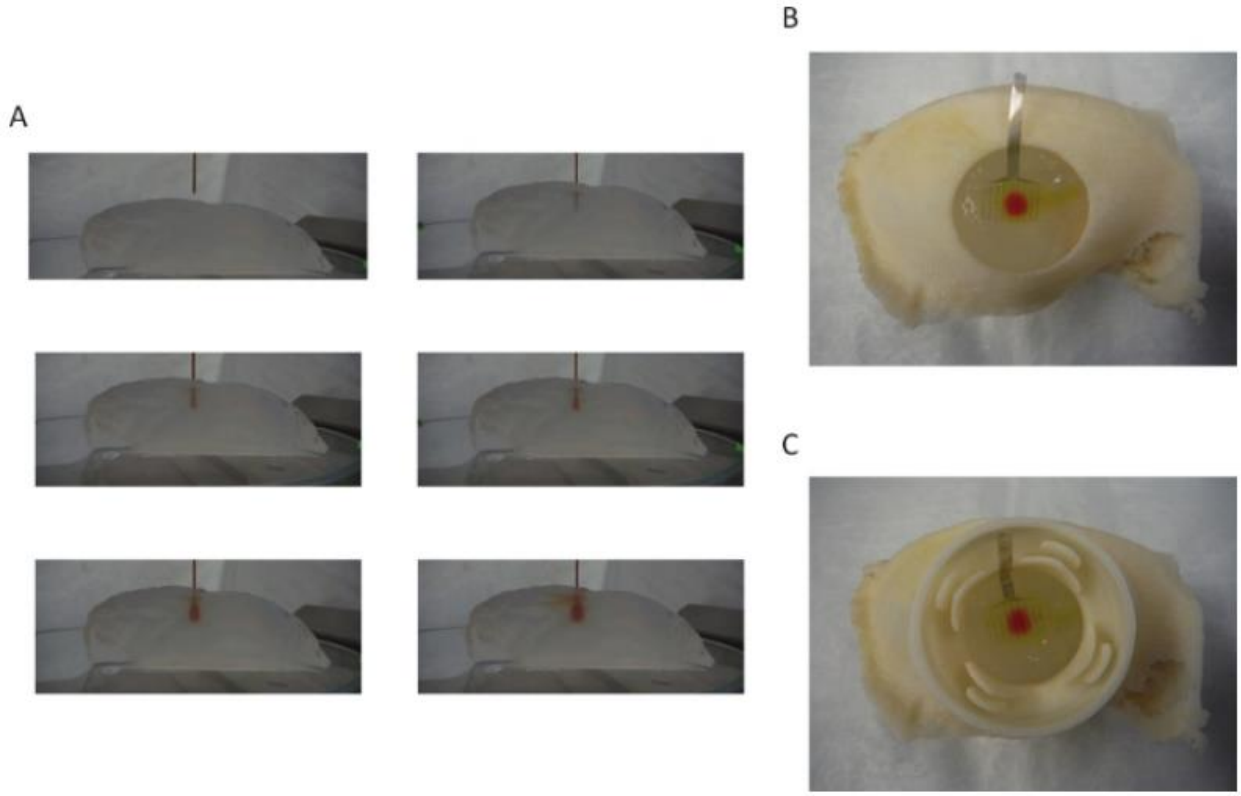

Figure 2.5: Injection modeling. (A) Time lapse images of the injection procedure. Top left panel pre-insertion. Top right panel post-insertion. Lower four panels show the spread of the dye over time. (B) Gel model of a section of the brain positioned within a 3D printed skull with a craniotomy such that injections of food coloring may be observed in relation to the cortical structures and electrode placement. (C) 3D print of a chamber fit to the skull and observed in relation to the electrode array, gel model, and injection. Reprinted from (Ojemann *et al.*, 2020) *with permission.*

When combined with the agarose mixture brain models, the surgical preparation toolbox can be applied to prepare for surgical procedures involving fluid injections such as optogenetics and chemogenetics (Azadeh Yazdan-Shahmorad *et al.*, 2016; Galvan *et al.*, 2017; Galvan, Caiola and Albaugh, 2018; Ju *et al.*, 2018; Yazdan-Shahmorad, Tian, *et al.*, 2018; Stephen L. Macknik *et al.*, 2019). This portion of the protocol is limited by the use of PLA to 3D print the molds instead of an ABS filament, which has a higher glass transition temperature. Changing this in future experiments will make the molding process more efficient and an industrial grade printer would introduce less error in the form of holes. Prior work has proposed agarose gel as an artificial material that can mimic some of the mechanical properties of the brain relevant to fluid infusion (Chen *et al.*, 2004; M T Krauze *et al.*, 2005). However, previous work has not combined the agarose with a brain-realistic mold to provide a surgical preparation tool. The molded agarose mixture gel brains can be used to give qualitative cortical context to the injection location and visualize the volume and location of fluid diffusion. The gel brains can also be used to practice the injection motion and location within the stereotaxic frame. This can be applied not only to optogenetics, but translated into other experiments requiring injection into the brain (Galvan, Caiola and Albaugh, 2018; Ju *et al.*, 2018; Stephen L. Macknik *et al.*, 2019). Modifying the injection-based model as well as the 3D printed brain with a contrast enhanced scan can help give contest to the location of critical vasculature and increase the efficacy of the protocol. The model can also be used to enhance the current CED standard practice by

optimizing injection speed and cannula thickness. This model can also be strengthened by the quantitative validation of the agarose gel mixture to accurately represent diffusive and convective flow in the brain (Azadeh Yazdan-Shahmorad *et al.*, 2016; Yazdan-Shahmorad, Tian, *et al.*, 2018).

2.5 Acknowledgments

This project was supported by the Eunice Kennedy Shiver National Institute of Child Health & Human Development of the National Institutes of Health under Award Number K12HD073945, the Washington National Primate Research Center (WaNPCR, P51 OD010425), the Center for Neurotechnology (CNT, a National Science Foundation Engineering Research Center under Grant EEC-1028725) and University of Washington Royalty Research Funds. Funding to the Macknik and Martinez-Conde labs for this project came from a BRAIN Initiative NSF-NCS Award 1734887, as well as NSF Awards 1523614 & 1829474, and SUNY Empire Innovator Scholarships to each professor. We thank Karam Khateeb for his help with agarose preparation, and Toni J Huan for technical help.

2.6 Disclosures

The authors have no conflicts of interest to disclose at this time.

Chapter 3: Multi-modal artificial dura for simultaneous large-scale optical access and large-scale electrophysiology in non-human primate cortex

This chapter is representative of work which is complete and published. Reprinted with permission. Please cite the final published version of this work:

> **Griggs DJ**, Khateeb K, Zhou J, Liu T, Wang R, Yazdan-Shahmorad A. (2021) 'Multi-modal artificial dura for simultaneous large-scale optical access and large-scale electrophysiology in non-human primate cortex,' *Journal of Neural Engineering, Special Issue 'Neuroelectronic Interfaces'*, 18(5), p. 2021.02.03.429596. doi: 10.1101/2021.02.03.429596.

3.0 Abstract

Objective. Non-human primates (NHPs) are critical for development of translational neural technologies because of their neurological and neuroanatomical similarities to humans. Large-scale neural interfaces in NHPs with multiple modalities for stimulation and data collection poise us to unveil network-scale dynamics of both healthy and unhealthy neural systems. We aim to develop a large-scale multi-modal interface for NHPs for the purpose of studying large-scale neural phenomena including neural disease, damage, and recovery.

Approach. We present a multi-modal artificial dura (MMAD) composed of flexible conductive traces printed into transparent medical grade polymer. Our MMAD provides simultaneous neurophysiological recordings and optical access to large areas of the cortex (~3 cm^2) and is designed to mitigate photo-induced electrical artifacts. The MMAD is the centerpiece of the interfaces we have designed to support electrocorticographic recording and stimulation, cortical imaging, and optogenetic experiments, all at the large-scales afforded by the brains of NHPs. We performed electrical and optical experiments bench-side and *in vivo* with macaques to validate the utility of our MMAD.

Main results. Using our MMAD we present large-scale electrocorticography from sensorimotor cortex of three macaques. Furthermore, we validated surface electrical stimulation in one of our animals. Our bench-side testing showed up to 90% reduction of photo-induced artifacts with our MMAD. The transparency of our MMAD was confirmed both via bench-side testing (87% transmittance) and via *in vivo* imaging of blood flow from the underlying microvasculature using optical coherence tomography angiography.

Significance. Our results indicate that our MMAD supports large-scale electrocorticography, large-scale cortical imaging, and, by extension, large-scale optical stimulation. The MMAD prepares the way for both acute and long-term chronic experiments with complimentary data collection and stimulation modalities. When paired with the complex behaviors and cognitive abilities of NHPs, these assets prepare us to study large-scale neural phenomena including neural disease, damage, and recovery.

3.1 Introduction

Non-human primates (NHPs) are a critical translational model for neuroscience (Camus *et al.*, 2015; Harding, 2017; Mitchell *et al.*, 2018). NHP brains are evolutionarily similar to humans and they can be trained to perform complex cognitive and behavioral tasks. Traditionally, neurophysiological research techniques studying neural phenomena were limited to small brain areas and singular modalities due to technological constraints. Such constraints in turn limited the degree of insight which could be gained. However, in recent years researchers have recognized that neural computations often incorporate multiple brain regions in a wide array of phenomena including post-traumatic stress disorder (Lanius *et al.*, 2015), aging (Li *et al.*, 2015), memory (Huijgen and Samson, 2015; Jeong, Chung and Kim, 2015),

schizophrenia (Dong *et al.*, 2018), creativity (Shi *et al.*, 2018), and others. Studies of large-scale brain activity often employ functional magnetic resonance imaging (fMRI), a modality with low spatial and temporal resolution. Further, fMRI is unable to perform neural stimulation – a critical tool for translational neurotherapeutic research. To increase spatial and temporal resolution and to provide stimulation capabilities at large-scales, modalities beyond fMRI must be considered in translational NHP research.

To study the cortex of NHPs at these large-scales, two key methodologies have been developed over the years: imaging (Shtoyerman *et al.*, 2000; Chen *et al.*, 2002; Slovin *et al.*, 2002; Chen, Friedman and Roe, 2005; Lu *et al.*, 2010; Ruiz *et al.*, 2013; Li *et al.*, 2017; Ju *et al.*, 2018) and electrocorticography (Bosman *et al.*, 2012; Fukushima, Chao and Fujii, 2015; Komatsu *et al.*, 2017; Chao *et al.*, 2018; Miyakawa *et al.*, 2018; Chiang, Lee, *et al.*, 2020; Chiang, Won, *et al.*, 2020; Kaiju *et al.*, 2021). To support cortical imaging, a transparent artificial dura implanted in a cranial chamber is often used to provide optical access (e.g., (Slovin *et al.*, 2002)). This optical window can support months of optical access before tissue growth over the surface of the brain clouds the window. To support chronic electrocorticography, the traditional approach is to close the surgical wound after implanting an electrocorticographic (ECoG) array (e.g., (Komatsu *et al.*, 2017)). Recently, a study has proposed an array integrated with an artificial dura implanted in a cranial chamber (Chiang, Won, *et al.*, 2020). This approach obscured optical access to the brain because of the high density of traces and electrodes laid across the cortex. However, we had previously demonstrated for the first time that chronic large-scale micro-ECoG and optical access to the NHP cortex could be achieved simultaneously with semi-transparent electrode arrays laid underneath an artificial dura (Yazdan-Shahmorad *et al.*, 2015; Azadeh Yazdan-Shahmorad *et al.*, 2016). Specifically, we used our interface to perform large-scale (~3 cm^2) fluorescence imaging and micro-ECoG recording, as well as optogenetic stimulation across large cortical areas. While this setup was effective, we recognized that integrating electrodes directly into an artificial dura optimized for optical access would reduce experimental complexity.

To this end, we present a flexible, transparent artificial dura with embedded electrodes, which we call a multi-modal artificial dura (MMAD). We present both bench-side data and acute *in vivo* data from NHPs under anesthesia highlighting the multi-modal functionality of our MMAD. Our MMAD is designed to be resistant to photo-induced artifact, to be capable of simultaneous surface electrical recording and stimulation, and to provide a large-scale optical window (~3 cm^2) to the cortex. The MMAD has long cables which allow neurophysiology systems acutely attached to the MMAD to be placed away from the optical window. This arrangement provides access for imaging hardware during experiments. The MMAD equips us for large-scale acute optical experiments in NHP cortex, such as optogenetic viral vector construct evaluation, with simultaneous electrophysiological recordings. Our MMAD is also designed to bring improved stability to our previously published chronic neural interfaces (Yazdan-Shahmorad *et al.*, 2015; Azadeh Yazdan-Shahmorad *et al.*, 2016; Griggs, Khateeb, Philips, Chan, Ojemann and Yazdan-Shahmorad, 2019) which would set the stage for optimized large-scale chronic multi-modal experiments with NHPs in the future. We also outline the remaining steps to chronic MMAD implementation.

3.2 Methods

We present an MMAD designed for large-scale *in vivo* optical and electrophysiological experiments in NHPs.

3.2.1 Subjects

Three adult female pig-tailed macaques (*Macaca nemestrina*) were used (Monkey D, 12.8 kg, 14 years; Monkey E, 13.1 kg, 14 years; Monkey F, 13.8 kg, 14 years). All animal care and experiments were approved by the University of Washington's Office of Animal Welfare, the Institutional Animal Care and Use Committee, and the Washington National Primate Research Center (WaNPRC).

3.2.2 Multi-modal Artificial Dura

Our MMAD is composed of an artificial dura made of a medical-grade transparent polymer with embedded electrodes providing surface ECoG recordings (Fig. 1a-b). Ripple Neuro (Ripple Neuro, Salt Lake City, UT) had introduced flexible, biocompatible, and semi-transparent ECoG electrodes, which we custom-designed for our MMADs. These arrays have interleaving opaque conductive layers (250-300 µm trace width with 800 µm pitch) and transparent insulating layers (50-60 µm thick) made of medical grade polymer (Fig. 1a-c). Each array provided a 20 mm diameter circle (314 mm^2) of optical access and 32 platinum electrodes (500 µm diameter, 2mm pitch) which can be used for both electrical recording and stimulation (Fig. 1d). An extra wide polymer skirt surrounded the grid of electrodes to aid in modifying the MMAD for experiment-specific needs (Fig. 1a). The MMAD is ultra-flexible because the conductive material is composed of platinum particles dispersed in a matrix within the polymer. To protect the conductive traces and electrodes from photo-induced artifacts, an additional set of non-recording traces and electrodes were printed directly above the traces and electrodes used for electrophysiology. We refer to this additional layer as the light-blocking layer (Fig. 1d). The light-blocking layer traces used for this iteration of MMADs were printed nominally 4x wider than the underlying traces and slightly larger than the underlying electrodes. These light-blocking layer traces permit optical access to 79% of the electrode recording area and about 76% of the full optical window. The traces extend out from the array through flexible cables and terminate in contacts which serve as an electrical junction between the array and clamp-connectors (Ripple Neuro, Salt Lake City, UT), which contain PCBs (Fig 1e). These clamp-connectors are only necessary during electrophysiological experiments which protects their internal PCBs from corrosion and enables easier storage of the MMADs for chronic *in vivo* experiments. Each clamp connector has a pin for electrical grounding.

3.2.3 Array Impedance

After production of the arrays and before implantation Ripple Neuro measured the impedance of all electrodes of four MMADs (N=128 electrodes, i.e., 4 arrays x 32 electrodes per array; measured dry with Fluke 179 True RMS Multimeter). Additionally, they measured the electrochemical impedance spectroscopy of all electrodes at 10.0 Hz, 100.0 Hz, and 1.0 kHz (electrode sites and leads submerged in normal saline solution). We performed additional impedance testing at 1 kHz with a Grapevine Nomad neurophysiology system at different timepoints post-production (Ripple Neuro, Salt Lake City, UT).

3.2.4 Optical Transmittance

We used white light to measure the optical transmittance of both the traditional transparent silicone-based artificial dura and the MMAD at five different wavelengths throughout the visible and infrared spectra (Thorlabs PM100D Power Meter and S121C Sensor). A mask with a 1 mm pinhole was used to increase the spatial specificity of the light source. We placed the beam in the center of both samples and, in the case of the MMAD, the beam of light was positioned on a transparent region (between the traces and electrodes).

3.2.5 Photo-induced Artifacts

To assess the light-blocking layer's efficacy, we optically stimulated both sides of an MMAD with a laser (Doric, Quebec, QC) via a fiberoptic cable and recorded results. The electrodes of the MMAD as well as the tip of the fiberoptic cable were submerged in normal saline, and the fiberoptic was approximately perpendicular to the surface of the MMAD. We focused the laser, pulsing at 1 Hz and at 1 ms per pulse, on one electrode while simultaneously recording from the array. Then we flipped the MMAD to illuminate the electrode from the light-blocking layer side, which replicates the orientation during *in vivo* experiments, and repeated the illumination and recording process. We performed this entire process for two neighboring electrodes and for both green (520 nm) and red light (638 nm; data not shown). We also

performed this entire process focusing the laser near, but not at, the same electrodes. The optical power of the laser was approximately 51 mW for green light and 104 mW for red light as measured with a photodiode (respectively measured at 535 nm and 635 nm; Thorlabs PM100D Power Meter and S121C Sensor).

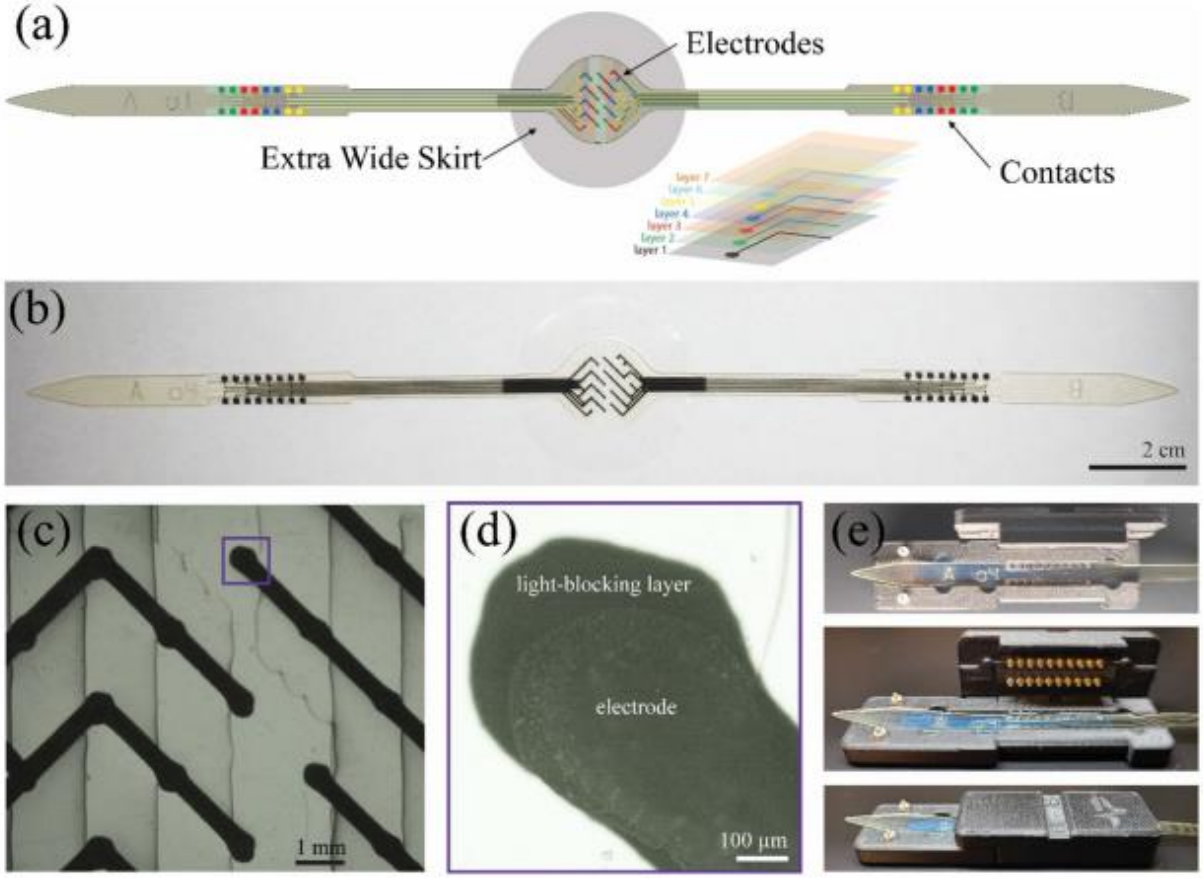

Figure 3.1: Multi-modal artificial dura (MMAD). (a) MMAD schematic. The MMAD is semitransparent and contains individually wired, opaque electrodes in the center with 250–300 µm traces embedded within five layers of a transparent medical grade copolymer. The traces extend down cables on opposite ends of the centered electrode array. The light-blocking layer (layer 1) is furthest from the cortex and mitigates photo-induced artifacts. The layered design causes the cortex to contact several layers. (b) MMAD. (c) Microscopic image of a portion of the electrode array. Edges of the polymer layers are evident. The box indicates the electrode shown in (d). (d) Microscopic image of one electrode (foreground) and its light-blocking layer (background). Due to the plane of focus for this image, the texture of the electrode can be observed near its edges. (e) MMAD cable positioned in a clamp-connector. MMAD contacts are aligned with pads on the printed circuit board. Reprinted from (Griggs *et al.*, 2021a) *with permission.*

3.2.6 Bench-side Electrical Stimulation

To verify our MMAD's capability of performing simultaneous stimulation and recording, we applied bench-side electrical stimulation at a single electrode with all electrode sites submerged in normal saline. We used a stimulation train with 5 Hz biphasic pulses and a 200 ms pulse width. The stimulation amplitude was 10uA for both phases. During each 1-min stimulation session we recorded from all 32 sites on the MMAD.

3.2.7 Connector holder

We designed a connector holder to secure the MMAD on the cortical surface and to hold the clamp-connectors during acute, anesthetized experimentation (Fig. 2a). An intra-cranial rim on the bottom of the connector holder fit inside a craniotomy (see section 2.8). This fit aided in keeping the connector holder stationary as holes were drilled for the skull screws necessary to affix the connector holder to the skull. The connector holder was 3D printed with plastic filament (acrylonitrile butadiene styrene (ABS) with quick support release (QSR) used as supports) which provided flexibility as the fastening of the skull screws warped the connector holder slightly against the curved skull surface. Slots on either side of the cranial window allow the flexible cables of the MMAD to exit the craniotomy and extend to the clamp-connectors (Fig. 2). The clamp-connectors were secured to the arms of the connector holder with rubber bands which hooked onto the crossbars of the arms. The angle of the arms was chosen to provide optimal clearance between the clamp-connectors and the sterile field, while still providing room for imaging equipment. The connector holder also included screw posts to aid in affixing or aligning additional experimental equipment to the connector holder, such as optical stimulation devices we have presented previously (Yazdan-Shahmorad *et al.*, 2015; Azadeh Yazdan-Shahmorad *et al.*, 2016; Griggs, Khateeb, Philips, Chan, Ojemann and Yazdan-Shahmorad, 2019), although these posts were not used in the experiments presented here.

3.2.8 Surgical Preparation

We collected data from all subjects during terminal experiments. The subject's temperature, heart rate, and respiration were monitored throughout the procedure. To begin surgical preparations, the subject was anesthetized with isoflurane and mounted into a stereotactic frame. An incision was made down the midline of the head. The skin and musculature were peeled from the skull laterally with elevators to reveal both sides of the skull. Then we used a trephine to create bilateral 25 mm diameter craniotomies targeting the primary motor and primary somatosensory cortices. We performed a durotomy by raising the dura off of the cortex with a needle and cutting out the dura with ophthalmic scissors. We cut four notches in the extra wide skirt, two adjacent to each MMAD cable, then we placed the MMAD on the cortex. The notches permitted us to insert the extra wide skirt under the skull and native dura while still allowing the cables to extend out of the cable slots in the connector holder. Connector holders were affixed to the skull bilaterally with screws to hold the MMADs in place and support the clamp-connectors. Each connector holder includes four skull screw holes, however only the two medial screw holes for each connector holder were necessary in practice. The arms of the connector holders extended roughly parallel to the midline so that the connector holders would not interfere with each other. We implanted an additional skull screw near the midline and away from the craniotomies to serve as an electrical ground – we connected conductive wires from the grounding pins of each clamp connector to the screw. The subjects were transitioned to urethane anesthesia (1 g/kg dose) prior to electrophysiology recordings and supplemental doses were administered as required to maintain the level of anesthesia.

3.2.9 Electrophysiology

We recorded ECoG data at 30 kHz sampling frequency bilaterally from all three subjects for 30 minutes and performed electrical stimulation in the left hemisphere of Monkey F. All electrophysiology data collection and electrical stimulation were performed with a Grapevine Nomad and Nano front ends (Ripple Neuro, Salt Lake City, UT).

3.2.10 *In Vivo* Electrical Stimulation

We implanted two MMADs bilaterally as described in section 2.8. We performed electrical stimulation delivered through a single electrode on the MMAD implanted on the left hemisphere of Monkey F. Stimulation took place in blocks after 30 minutes of baseline recording. Each of six stimulation blocks

lasted 10 minutes, with 2 minutes of baseline recordings in between the blocks to track changes in electrophysiology. The stimulation trains had a 5 Hz burst frequency with five 1 kHz biphasic pulses within each burst. The stimulation amplitude was set to 65 µA for both phases.

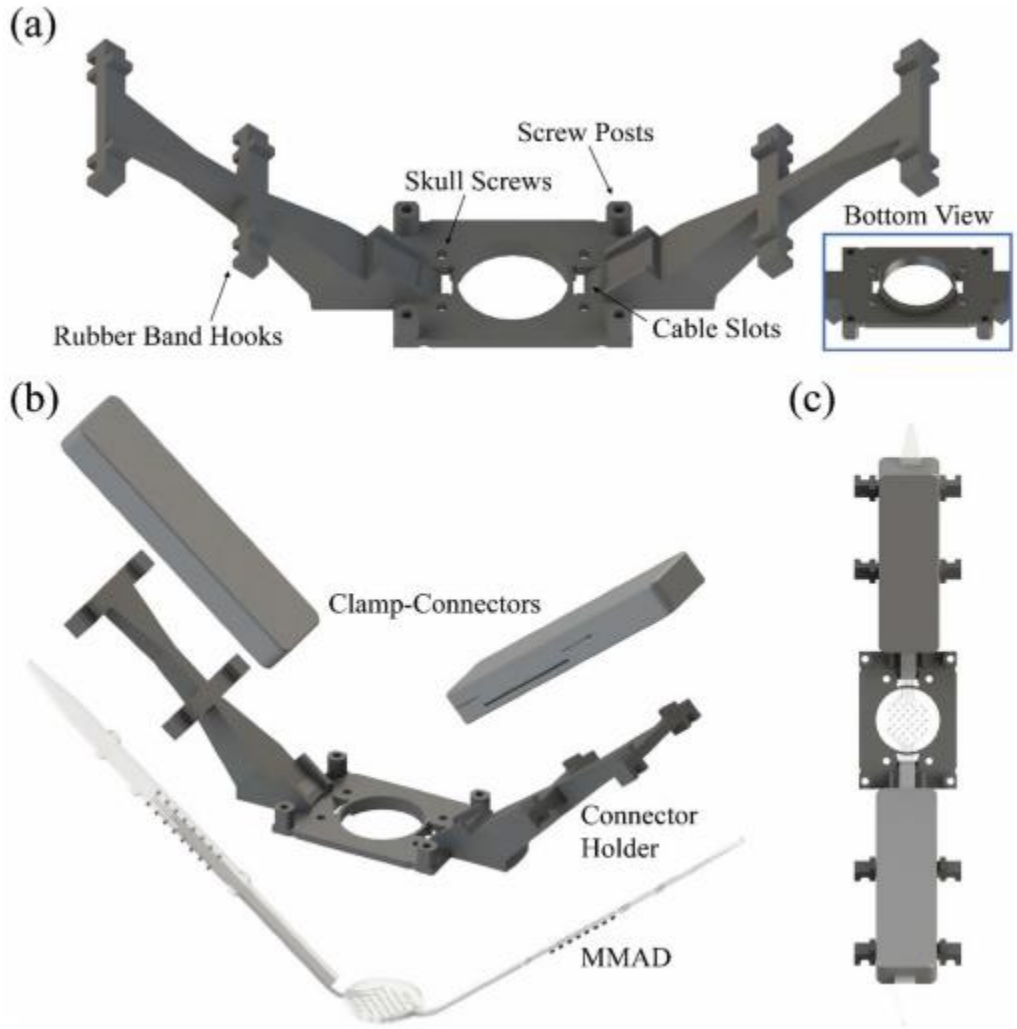

Figure 3.2: Acute interface. (a) Acute interface connector holder. The connector holder secures the MMAD electrode array against the brain and holds the clamp-connectors (b) away from the subject with rubber bands which attach to the rubber band hooks. The cables of the MMAD are passed through the cable slots to interface with the clamp-connectors (b) and (c). The connector holder is secured to the skull with skull screws inserted through holes near the cranial window. Additional equipment may be affixed or aligned to the connector holder with the screw posts. Inset: bottom view of the connector holder revealing the intra-cranial rim which aids in centering the MMAD and connector holder over the craniotomy. (b) and (c) Acute interface stack-up. The MMAD array cables thread through the slots and are secured in the clamp-connectors which rest on either arm of the connector holder. Reprinted from (Griggs *et al.*, 2021a) *with permission.*

3.2.11 Optical Coherence Tomography Angiography

To validate the transparency and imaging capabilities of our MMAD *in vivo*, we performed optical coherence tomography angiography (OCTA) through the MMAD placed on the cortex of the right hemisphere of Monkey D. Imaging and image processing were performed with previously described methods (An, Qin and Wang, 2010; Deegan *et al.*, 2018). We used an articulating arm to position the OCTA probe over the optical window. The low profile of the portion of the connector holder near the craniotomy provided access for the OCTA probe to be positioned near the MMAD. Electrophysiological data were not

collected during this proof-of-concept imaging session. Of note, current OCTA techniques require post-processing which prevents real-time visualization of large-scale images.

3.3 Results

As described above, we validated our MMAD both with bench-side tests and acute *in vivo* experiments.

3.3.1 Bench-side Data

3.3.1.1 Array Impedance

The direct current resistance of the electrodes had a mean of 342.7 Ω and a standard deviation of 21.4 Ω, and all electrodes had an isolation resistance higher than 10 MΩ. The electrochemical impedance spectroscopy of all electrodes at 10.0 Hz, 100.0 Hz, and 1.0 kHz respectively had means of 5.56 MΩ, 1.59 MΩ, and 268.8 kΩ and respective standard deviations of 1.59 MΩ, 0.31 MΩ, and 46.3 kΩ (Fig. 3a).

We used the same two MMADs for all three acute experiments: the first two acute experiments were conducted 5 to 6 months post array production while the third experiment was conducted 15 months post production. Both arrays demonstrated bench-side impedance values within the expected range through the first experiment. However, during and after the third *in vivo* experiment, we found 10 failed electrodes with abnormally high impedance and electrically disconnected recording traces on each array. Further bench-side testing of two unused arrays with the same production date also showed 12 and 8 bad electrodes respectively. Upon further investigation, we found that these failed electrodes were largely printed on the same conductive layer across all 4 arrays.

3.3.1.2 Optical Transmittance

When normalized, the optical transmittance values of the artificial dura and MMAD resulted in approximately 95% and 88%, respectively, across all five wavelengths measured (Fig. 3b). The variance in the MMAD data is greater than that of the artificial dura. We believe the variance in optical properties due to the multi-layering approach of MMAD fabrication accounts for the variation in transmittance.

3.3.1.3 Photo-induced Artifacts

For both electrodes and both light colors we found that the light-blocking layer reduced photo-induced responses by 87–90% (Fig. 3c-d, responses measured peak-to-peak). Since the photo-induced response was limited to the stimulated electrode, we can infer that the induced artifact was caused by the illumination as opposed to electrical noise. The illumination process was repeated with the laser directed near, but not at, the electrode. In this case we found that the light-blocking layer practically eliminated photo-induced artifact. We did not observe any difference between red and green illumination.

3.3.1.4 Stimulation Waveforms

During the bench-side electrical stimulation, we observed rapid signal recovery within 10 ms at all recording channels except the stimulation channel (Fig. 3e). When comparing raw stimulation waveforms at 2 mm, 4 mm, and 8 mm away from the stimulation electrode, we also found that the amplitude of stimulation artifact and signal recovery time both decreased with the distance between our recording and stimulation sites. This fast signal settling suggests that our MMAD is able to simultaneously stimulate and record neural activity across a large area surrounding the stimulation site.

3.3.2 Acute *In Vivo* Data

We validated surface electrical recording and stimulation, as well as cortical imaging through our MMAD *in vivo*.

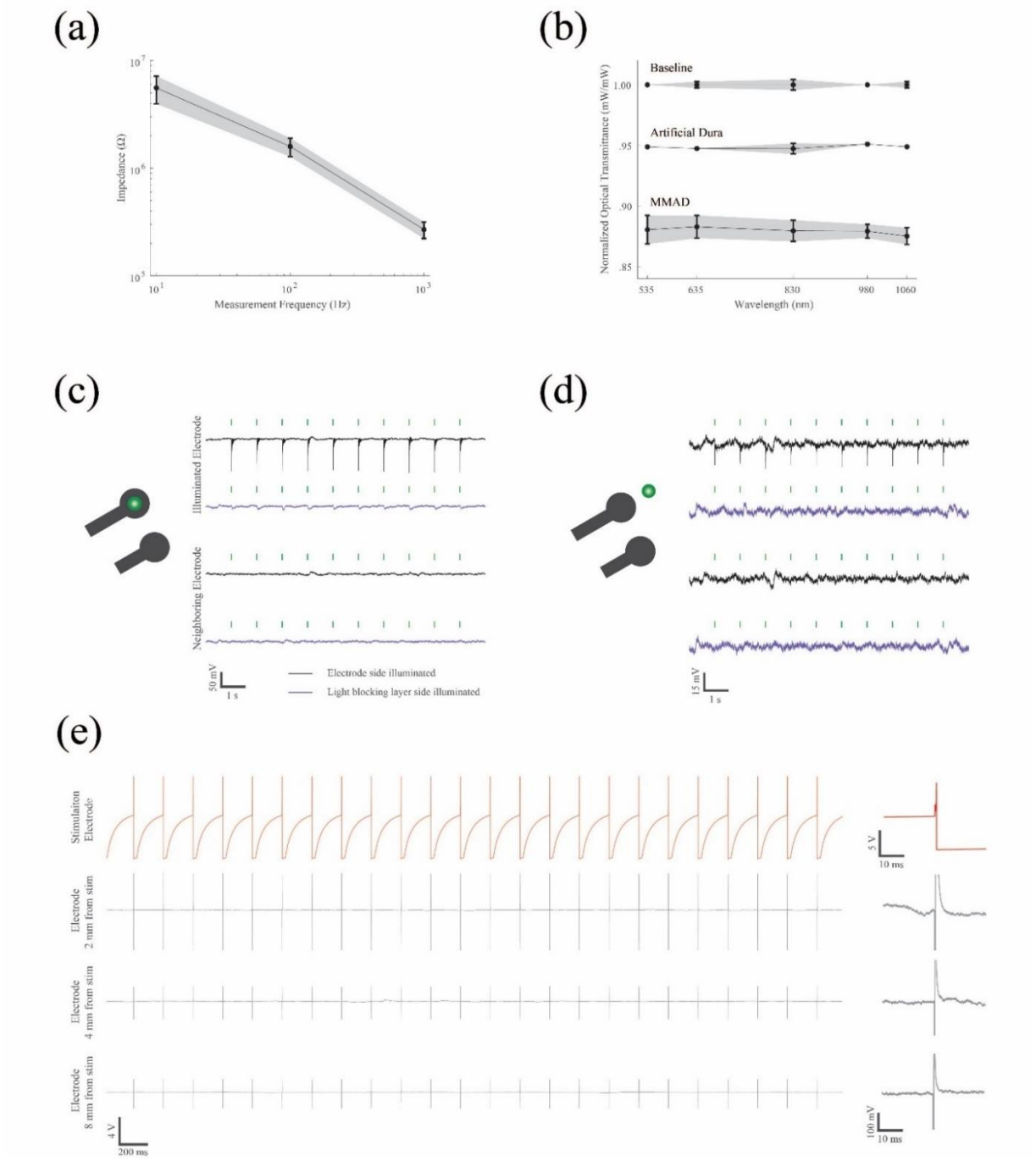

Figure 3.3: Bench-side results. (a) Initial mean impedance and standard deviation of four MMADs with 32 electrodes each (total electrode count N = 128) measured at 10 Hz, 100 Hz, and 1 kHz. (b) Mean and standard deviation optical transmittance of a classic silicone-based artificial dura and our MMAD. A white light source was projected through a mask with a 1 mm pin hole which, in the case of the MMAD, was aligned to project between electrode traces. Results were recorded at five wavelengths within the visible and infrared spectra. (c) Photo-induced artifacts of an electrode illuminated by green light, and a neighboring electrode recorded simultaneously. Black traces indicate when the electrode was illuminated directly (i.e. the MMAD was upside down) and purple traces indicate when the electrode's light-blocking layer was illuminated. Both the tip of the fiberoptic cable and the MMAD were submerged in saline. (d) Photo-induced artifacts as in (c) where the MMAD was illuminated near, but not on, the electrode. (e) Electrical stimulation waveforms. Left panel: stimulation channel (red) and other recording channels (grey) at varying distances away from the stimulation channel. Right panel: example stimulation waveforms for each channel. Reprinted from (Griggs *et al.*, 2021a) *with permission.*

3.3.2.1 Optical Coherence Tomography Angiography

We demonstrated the ability to perform OCTA imaging through the semi-transparent MMAD. Our acute setup permitted us to position imaging hardware close to the MMAD surface. Importantly, the transparency of the MMAD allowed for imaging of blood flow in the underlying microvascular structures down to 600 µm in depth, which is the maximum achieved with OCTA under the current experimental setting (Fig. 4). As expected, the electrodes and traces occluded the OCTA field of view. However, the extent of disruption was minimal and did not prevent imaging in the semi-transparent regions of the MMAD. The data collected through the MMAD were qualitatively similar to data collected through a transparent silicone-based artificial dura (data not shown).

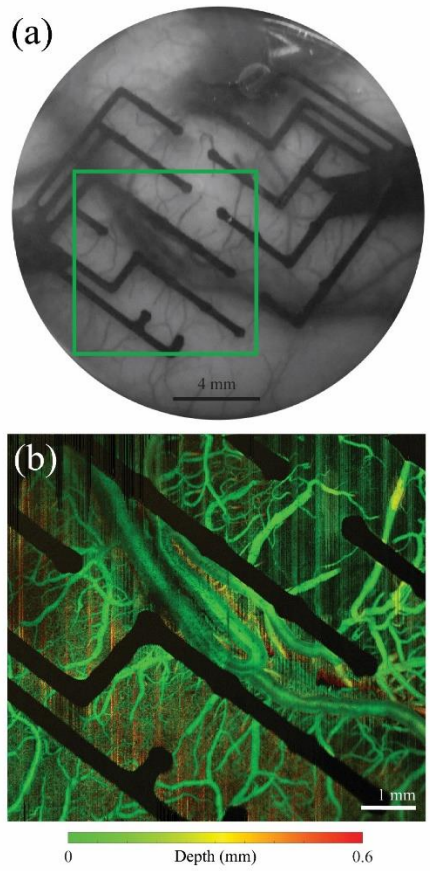

Figure 3.4: In vivo imaging. (a) Greyscale picture of the MMAD on the sensorimotor cortex of an NHP. Box indicates the region imaged in (b). (b) Optical coherence tomography angiography of the cortex as imaged through the array. Reprinted from (Griggs *et al.*, 2021a) *with permission.*

3.3.2.2 ECoG Recordings

We successfully collected bilateral ECoG data from all three subjects under urethane anesthesia (Fig. S1). The power spectral densities of the electrodes calculated over a 30-minute period approximate a $1/f^{\alpha}$ curve, while peaks are evident at 60 Hz and its harmonics, as expected (Fig. 5a). Example heatmaps from bilateral recordings of Monkey D in different frequency bands reveal a heterogenous distribution of power and groupings of electrodes (Fig. 5b). During recording, we observed artifacts when the animal was touched. In addition, across the two MMADs implanted in each subject, we saw two bad channels for Monkey D, four bad channels for Monkey E, and 20 bad channels for Monkey F with abnormally low signal power, which were excluded from analysis. Further testing suggested that the bad channels we observed

from Monkey F recordings matched the failed electrodes we found in bench-side impedance measurements (see section 3.1.1).

3.3.2.3 ECoG Stimulation

We successfully performed electrical stimulation on the left hemisphere of Monkey F while recording bilateral electrophysiology. We calculated the power spectral densities both before and after stimulation and observed a $1/f^{\alpha}$ curve in both cases which is characteristic of neural data (Fig. 5c, left column). The power spectral densities compared between the stimulated and non-stimulated hemispheres were qualitatively similar as well (Fig. 5c). Due to reduced recording time (2 minutes) the traces from before and after stimulation (Fig. 5c) are expected to be less smooth than the baseline recording traces (Fig. 5a). Specifically, we present the power spectral densities after 30000 stimulation pulses (20 minutes) to give us a reliable perspective of stimulation impact on electrodes.

We measured the impedance of the electrodes before and after stimulation with our electrophysiology system's built-in 1 kHz impedance measurement tool. To prevent bad channels from skewing the data, we omitted any impedance greater than 850 kΩ. We found that impedances did change for some electrodes (Fig. 5d; mean: -2.2 kΩ, -1.9%; standard deviation: 18.7 kΩ, 16.3%). However, when the distribution of the mean impedances of the electrodes were compared between before and after stimulation with a paired t-test, no significance was found (p=0.60). Similarly, the stimulated electrode did not exhibit impedance changes statistically different from the other electrodes (p=0.055). The success of electrical stimulation and recording from MMADs shows efficient electrical connection between our MMAD and our recording system and validates our design which eliminates the need for permanent attachment of PCBs to the MMAD. This shows the efficacy of our design and paves the path for chronic implementation of our MMADs.

3.4 Discussion

Artificial duras have been used for decades to provide large-scale optical access to the brains of NHPs (Arieli, Grinvald and Slovin, 2002; Slovin *et al.*, 2002; Chernov and Roe, 2014; Nassi *et al.*, 2015; Azadeh Yazdan-Shahmorad *et al.*, 2016; Seidemann *et al.*, 2016; Zaraza *et al.*, 2020). Over the years there have been advances in large-scale optical imaging and optical stimulation modalities, including the discovery (Boyden *et al.*, 2005) and widespread proliferation of optogenetics (Yizhar *et al.*, 2011). However, there has been little change in artificial dura designs for NHPs. Here, we present a multi-modal artificial dura, being an artificial dura with embedded electrodes. The MMAD is designed with multiple layers of traces and electrodes vertically aligned in a transparent polymer to increase the transparent surface area, making it well fit for large-scale optical modalities. We have previously demonstrated micro-ECoG arrays which supported large-scale optogenetics in NHPs (Azadeh Yazdan-Shahmorad *et al.*, 2016), but the arrays were fragile and not suitable to be molded into an artificial dura. In contrast, our MMAD can be utilized as both an electrode array and an artificial dura because our conductive traces are flexible. Additionally, our previous micro-ECoG arrays were attached to PCBs which were prone to corrosion. In our present design, the absence of permanently attached PCBs makes the MMAD setup corrosion resistant. The wide spacing between the electrode traces would provide easy integration with penetrating electrical or optical probes similar to others (Ruiz *et al.*, 2013). Moreover, combining an artificial dura and an electrode array by printing flexible traces and electrodes directly into the artificial dura curtails experimental complexity by reducing the number of components required for multi-modal experiments.

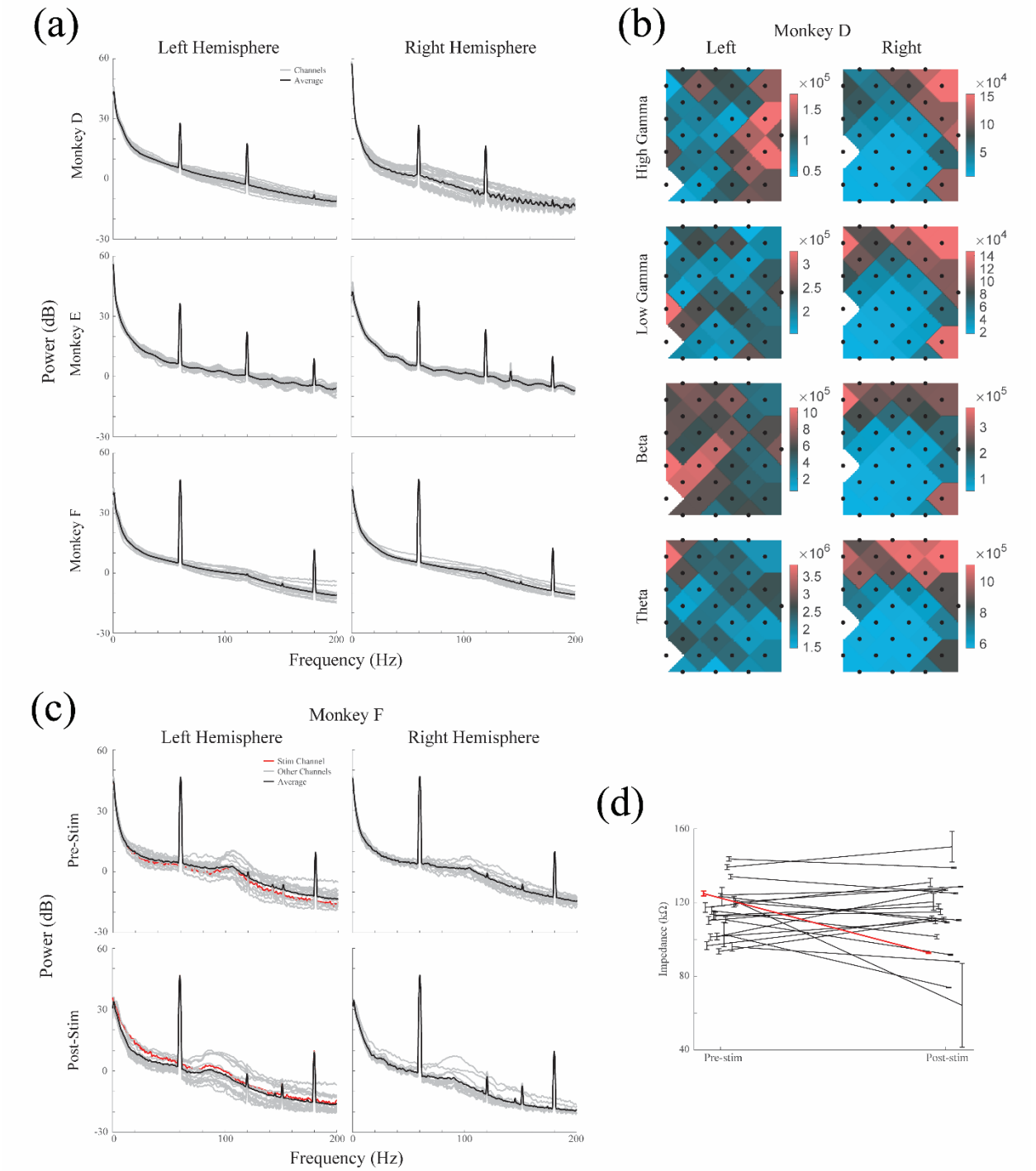

Figure 3.5: In vivo electrocorticography and stimulation. (a) Power spectral densities of left and right hemispheres of three NHPs, recorded with MMADs for 30 min at 30 kHz sampling frequency. Individual electrodes are traced in grey and the mean is traced in black. Power lines cause noise spikes at 60 Hz and its harmonics. High impedance electrodes have been omitted. (b) Electrode array power heatmaps of left and right hemispheres of Monkey D at four frequency bins: theta (4–7 Hz), beta (12–29 Hz), low gamma (30–59 Hz), and high gamma (60–150 Hz). In each array one electrode had high impedance and was omitted. (c) Power spectral densities of left and right hemispheres of Monkey F recorded for two minutes before and after 20 min of stimulation. Individual electrodes are traced in grey, the stimulating electrode is traced in red, and the mean is traced in black. High impedance electrodes have been omitted. (d) Standard error of the mean impedance measurements of electrodes before and after stimulation. The electrode used for stimulation is shown in red. Reprinted from (Griggs *et al.*, 2021a) *with permission.*

Traditional artificial duras have been used in NHPs for a variety of optical imaging and stimulation modalities including intrinsic optical imaging (Arieli, Grinvald and Slovin, 2002; Ruiz *et al.*, 2013; Chernov and Roe, 2014; Zaraza *et al.*, 2020), voltage sensitive dye imaging (Arieli, Grinvald and Slovin, 2002; Slovin *et al.*, 2002), calcium imaging (Seidemann *et al.*, 2016), fluorescence imaging (Nassi *et al.*, 2015; Azadeh Yazdan-Shahmorad *et al.*, 2016), OCTA (Karam Khateeb, Yao, *et al.*, 2019), infrared neural stimulation (Chernov and Roe, 2014), and optogenetics (Ruiz *et al.*, 2013; Nassi *et al.*, 2015; Azadeh Yazdan-Shahmorad *et al.*, 2016).

With our MMAD we aim to accommodate optical modalities such as these in tandem with ECoG recording. After characterizing the MMAD with optical and electrical bench-side tests, we validated the utility of our MMAD via an acute implementation by 1- collecting bilateral ECoG data from the cortex of three NHPs, 2- performing electrical stimulation in one of the subjects, and 3- performing OCTA imaging through the MMAD in one of the subjects. Analysis of the acute data presented in this paper show that the MMAD effectively performs both ECoG recording and stimulation while maintaining optical access for OCTA. Electrophysiological data were not collected during our proof-of-concept imaging session. However, we do not expect to have any issues collecting electrophysiology data while performing OCTA or other large-scale optical modalities such as optogenetics and calcium imaging in NHPs. In particular, our OCTA data show we can image the blood flow through the array and our previous optogenetic data (Yazdan-Shahmorad *et al.*, 2015; Azadeh Yazdan-Shahmorad *et al.*, 2016) show that as long as the light sources are not directly placed on top of an opaque electrode or trace, light penetration would be sufficient to evoke reliable neural responses.

A novel aspect of our design is the technology developed by Ripple Neuro (Salt Lake City, UT) which provides the capability to attach and detach the PCBs from the MMADs through clamp-connectors. This enables us to store the MMADs chronically in cranial chambers, reduce the risk for corrosion of the electronics, and reduce the complexity of chamber design. The electrical stimulation and recording capabilities demonstrated here validate the electrical connection between the electrodes and our recording system through the clamp-connectors.

Concerns of generating photo-induced artifacts naturally arise when optical and electrophysiological modalities are combined. The most obvious approach to avoiding photo-induced artifacts is directing the light away from metal traces. For optogenetic applications, we can also use opsin kinetics to distinguish between light-evoked neural activity and photo-induced artifact similar to our previous work (Ledochowitsch *et al.*, 2015). In that work, we stimulated at frequencies higher than our opsin off-kinetics. If light-evoked signal was detected from electrodes near the stimulated area, we concluded that signal was non-biological. This was only happening if the tip of our fiberoptic was directly located on an electrode and moving the fiber away slightly was solving the problem. We can use this technique to identify photo-induced artifacts in our MMAD as well.

In this paper, we also demonstrate that the addition of a light-blocking layer over electrodes reduces photo-induced artifacts substantially when optical stimulation is directed at the electrode, and practically eliminates artifact when the optical stimulation is directed near, but not at, the electrode. Like the recording traces, the light blocking layer traces are printed with platinum particles because of their strong adhesion properties. As mentioned above, when the fiberoptic was placed directly above the electrode, we observed reduced photo-induced artifact through the light-blocking layer. It is worth noting that the artifact waveform in this case was shaped distinctly different from the artifact waveform produced without the light-blocking layer. In particular, the former has a slow rise and fall, while the later has a sharp onset and quickly falls off. This slow response suggests some capacitive effects between the light-blocking layer and the electrode. To address this issue in future MMAD iterations, we plan to electrically

ground the light-blocking layer or print the light-blocking layer with a highly opaque non-conductive material. We also plan to vary the width of the light-blocking layer traces to optimize the balance between artifact protection and optical access to the brain. Our present MMAD design eliminates photo-induced artifact when the light is not directed at the electrode. For instances when a light source is close to the electrode site we can use the artifact detection process described above to mitigate the artifact. In sum, our data suggest that the MMAD is suitable for simultaneous optical and electrophysiological modalities. We plan to demonstrate such simultaneous data collection in future work.

Given that all MMAD electrodes tested immediately before the first *in vivo* experiment showed normal impedance values, the two bad channels we saw from Monkey D recording were likely caused by poor contact between the MMAD tails and PCB clamp connectors, not intrinsic electrode failure. However, from the *in vivo* experiment in Monkey F and the subsequent bench-side impedance testing, we observed that some of the electrodes from the same print layer on both the used and unused MMAD arrays went bad between 6 and 15 months post production. We are working with Ripple Neuro to understand the major reasons underlying these failures and improve our next batch of arrays being produced. However, even with these limitations, our bench-side and *in vivo* data still suggest that we can reliably use the MMAD in animal experiments for at least 6 months after production.

Additional limitations of our MMAD are the number, size, and pitch of electrodes. These properties arise from a combination of current printing constraints and trade-offs between electrode coverage and optical access. Another related limitation is that cells directly beneath the electrodes are shielded from optical modalities. However, we have previously shown that optogenetic stimulation near an electrode can reliably evoke neural responses which can be recorded by opaque electrodes (Azadeh Yazdan-Shahmorad *et al.*, 2016). In the future, we plan to investigate alternative fabrication methods to provide greater electrode array coverage without compromising optical access and flexibility.

While other groups have developed interfaces for large-scale imaging (Shtoyerman *et al.*, 2000; Chen *et al.*, 2002; Slovin *et al.*, 2002; Chen, Friedman and Roe, 2005; Lu *et al.*, 2010; Ruiz *et al.*, 2013; Li *et al.*, 2017; Ju *et al.*, 2018), large-scale electrocorticography (Bosman *et al.*, 2012; Fukushima, Chao and Fujii, 2015; Komatsu *et al.*, 2017; Chao *et al.*, 2018; Miyakawa *et al.*, 2018; Chiang, Lee, *et al.*, 2020; Chiang, Won, *et al.*, 2020; Kaiju *et al.*, 2021), and large-scale optogenetics (Komatsu *et al.*, 2017; Rajalingham *et al.*, 2020) in NHPs, and still others have proposed a variety of multi-modal systems with other animal models (Kwon *et al.*, 2012; Kuzum *et al.*, 2014; Richner *et al.*, 2014; Ji *et al.*, 2017, 2018; Liu *et al.*, 2018; Stamatakis *et al.*, 2018; Zátonyi *et al.*, 2018; Renz *et al.*, 2020), to our knowledge we remain the only group to have brought all three technologies together chronically for NHPs (Yazdan-Shahmorad *et al.*, 2015; Azadeh Yazdan-Shahmorad *et al.*, 2016). This suggests that a simpler and more robust interface may be broadly advantageous. With this in mind, we designed our MMAD to be adapted for chronic use.

Our previous interface consisted of a chronically implanted chamber but required daily implantation and explantation of the micro-ECoG array, which was a time-consuming process (Azadeh Yazdan-Shahmorad *et al.*, 2016). Additionally, this process introduced unwanted variance in day-to-day electrode positions on the cortex, and daily perturbation of the cortex appeared to accelerate tissue growth on the surface of the brain, obstructing optical access in 4-5 weeks. In order to restore optical access we had to wait for the tissue to mature and separate from the cortex so that the tissue could be resected for continued optical experiments (Azadeh Yazdan-Shahmorad *et al.*, 2016). When we tried chronically implanting micro-ECoG arrays beneath the artificial dura, we observed accelerated tissue growth over the top of the array, which obstructed optical access within a few weeks, thus also forcing us to wait to perform a resection (Yazdan-Shahmorad *et al.*, 2015). Due to these issues with both acute and chronic implementation of the micro-ECoG arrays in conjunction with artificial duras, we designed our MMAD to

prevent tissue growth over the top of the electrode array during chronic implantation by printing the electrode array into the artificial dura itself. Based on our past experience with traditional artificial duras (Azadeh Yazdan-Shahmorad *et al.*, 2016) and similar experiences of others (Arieli, Grinvald and Slovin, 2002; Chen, Friedman and Roe, 2005; Ruiz *et al.*, 2013), we expect that an artificial dura with integrated electrodes, as opposed to a separate electrode array, will reduce tissue growth on top of the brain while maintaining large-scale optical and electrophysiological access to the brain. Furthermore, bringing optical access and electrodes together into a single device would reduce experimental complexity. We previously published designs for a cranial chamber to chronically stabilize the MMAD on the cortex (Griggs, Khateeb, Philips, Chan, Ojemann and Yazdan-Shahmorad, 2019). We expect this stabilization to mitigate variance in day-to-day electrode positioning and reduce perturbations of the cortex which, as previously stated, appeared to accelerate tissue growth on the surface of the brain (Azadeh Yazdan-Shahmorad *et al.*, 2016). The cranial chamber is also designed to house the flexible, PCB-free, corrosion-resistant MMAD cables in a coiled configuration between experiments as we have shown bench-side (Griggs, Khateeb, Philips, Chan, Ojemann and Yazdan-Shahmorad, 2019) which will eliminate our previous corrosion issues with permanently mounted PCBs (Yazdan-Shahmorad *et al.*, 2015).

We outlined a roadmap to chronic implantation of our MMAD in Fig. S2. We have completed bench-side and acute *in vivo* experiments in this work, and we have previously published designs for a chronically implantable chamber (Griggs, Khateeb, Philips, Chan, Ojemann and Yazdan-Shahmorad, 2019). In the future, we plan to implant the chamber, perform a viral vector transfusion with methods similar to those we have previously published (Azadeh Yazdan-Shahmorad *et al.*, 2016; Karam Khateeb, Griggs, *et al.*, 2019), and implant the MMAD, molded into its chronic form (Griggs, Khateeb, Philips, Chan, Ojemann and Yazdan-Shahmorad, 2019), in a single surgery. We expect that viral expression will be sufficiently pronounced roughly 2 months after the surgery, at which point we will be prepared to perform chronic *in vivo* experiments with electrophysiology, electrical stimulation, imaging, and optogenetic modulation.

Our MMAD in combination with our previously presented chronic interfaces (Yazdan-Shahmorad *et al.*, 2015; Azadeh Yazdan-Shahmorad *et al.*, 2016; Griggs, Khateeb, Philips, Chan, Ojemann and Yazdan-Shahmorad, 2019) equip us for a variety of research pursuits. Moving forward, we plan to capitalize on our previous optogenetic (Ledochowitsch *et al.*, 2015; Yazdan-Shahmorad *et al.*, 2015; Azadeh Yazdan-Shahmorad *et al.*, 2016; Azadeh Yazdan-Shahmorad, Silversmith and Sabes, 2018; Yazdan-Shahmorad, Silversmith, *et al.*, 2018; Yazdan-Shahmorad, Tian, *et al.*, 2018; Karam Khateeb, Griggs, *et al.*, 2019; Ojemann *et al.*, 2020; Tremblay *et al.*, 2020) and imaging (Karam Khateeb, Yao, *et al.*, 2019; Stephen L. Macknik *et al.*, 2019) experience as we pioneer the experimental spaces unveiled by the merging of large-scale ECoG and large-scale optical access to the NHP cortex. The synergistic power of these technologies poise us to build on our past work investigating neural plasticity (Yazdan-Shahmorad, Silversmith, *et al.*, 2018; Bloch *et al.*, 2019) as we study large-scale, chronic neural phenomena including neural disease, damage, and recovery. To specifically mention one example research pursuit, we plan to use the MMAD to study the effects of stimulation during recovery from our photothrombotic stroke model (Karam Khateeb, Yao, *et al.*, 2019).

3.5 Conclusion

In this paper, we are integrating electrodes into a traditional artificial dura, expanding its functionality. Our presented MMAD for NHPs supports both large scale optical methods and large-scale electrical recording and stimulation. Specifically, we presented acute *in vivo* data demonstrating the utility of our MMAD for OCTA imaging and electrophysiological recording and stimulation of the large brains of macaques. In addition, our MMADs are compatible for chronic, large-scale electrophysiological experiments complimented by optical techniques, such as imaging and optogenetics.

3.6 Acknowledgments

We would like to thank Toni Han and WaNPRC staff for helping prepare for and run the surgeries; WaNPRC staff for animal care; William Ojemann, Julien Bloch, and Maryam Bahadori-Nejad for helping with interface design; and Minh Nhan Le for helping with the OCTA collection. We would also like to thank Alex Thiessen, Jessi Mischel, and Jose Ortega from Ripple Neuro for their help with the design and manufacturing of the MMADs.

None of the authors have any conflicts of interest to disclose.

This project was supported by the Eunice Kennedy Shriver National Institute of Child Health & Human Development of the National Institutes of Health (K12HD073945, AY), the University of Washington Royalty Research Fund (AY), the Washington National Primate Research Center (WaNPRC, P51 OD010425), the Center for Neurotechnology (CNT, a National Science Foundation Engineering Research Center, EEC-1028725, DG), the National Science Foundation Graduate Research Fellowship (KK), and the Weill Neurohub (JZ).

AY conceptualized the experiments, AY and RK provided supervision and resources; AY, RK, and KK acquired funding; DG, JZ, KK, and AY designed experiments; DG, JZ, KK, TL, and AY performed data collection; JZ, KK, TL, and AY performed data analysis; DG wrote the original draft of the manuscript; DG, JZ, KK, TL, RK, and AY revised and edited the manuscript.

Chapter 4: Optimized large-scale cortical optogenetic interface for non-human primates

This chapter is representative of work which is in-progress and nearing completion. In 2022, I plan to submit a revised version of this chapter to a peer-reviewed journal. Portions of this chapter are reproduced with permission and representative of published work. Where appropriate, please cite as:

> **Griggs DJ**, Chan J, Ojemann W, Phillips S, Khateeb K, Yazdan-Shahmorad A. 'Optimized large-scale optogenetic interface for non-human primates,' *SPIE BIOS Conference,* San Francisco, CA, Feb 2–7, 2019.
>
> **Griggs DJ**, Belloir T, Yazdan-Shahmorad A. 'Large-scale neural interfaces for optogenetic actuators and sensors in non-human primates,' *SPIE BIOS Conference,* Virtual, Mar 5, 2021.
>
> **Griggs DJ**, Bloch J, Fisher S, Ojemann W. K. S., Coubrough K. M., Khateeb K., Chu M., Yazdan-Shahmorad A. 'Demonstration of an optimized large-scale optogenetic cortical interface for non-human primates,' *IEEE Engineering in Medicine and Biology Society Conference,* Glasgow, Scotland, UK, Jul 11-15, 2022. (In Press, © 2022 IEEE)

4.0 Abstract

Stable large-scale optogenetic interfaces for non-human primates have great potential to answer fundamental questions about brain function and develop novel therapies for neurological disorders. Our lab has previously reported an interface that enables manipulation and recording from up to 2 cm^2 of cortical tissue by combining three technologies: 1) convection enhanced viral delivery to achieve high levels of expression across large cortical areas, 2) semi-transparent micro-electrocorticographic arrays to record from areas of viral expression, and 3) artificial dura to both protect and provide optical access to the brain. Although this interface provided a unique platform to study network activity and connectivity, it required day-to-day implantation and explantation of the recording array from the cortical surface. This led to accelerated tissue growth on top of the brain and limited the efficient time window for optical access to about 4 weeks. Here, we report improvements to our interface: We have 1) incorporated the recording array into the artificial dura to reduce manipulation at the brain surface and increase the efficient optical access window to over 3 months, 2) designed corrosion resistance into our interface, and 3) increased the number of simultaneous light stimulation locations from 3 to 16. With this interface we demonstrate optogenetic modulation across tens of mm^2 of the posterior parietal cortex, one of the largest demonstrations of optogenetic neural modulation to our knowledge. We also demonstrate that our large-scale neural deactivation causes NHPs to reach more slowly in a center-out task, which confirms the behavioral efficacy of our system.

4.1 Introduction

Optogenetics is unique among neuromodulation technologies because it allows for cell-type specific manipulation of neural networks with high spatial and temporal precision. These unique advantages empower researchers to explore areas such as fundamental neuroscience (Carter and de Lecea, 2011; Chen *et al.*, 2013; Adhikari *et al.*, 2015; Barnett *et al.*, 2018; Camporeze *et al.*, 2018), learning and memory (Spellman *et al.*, 2015; Barnett *et al.*, 2018; Yang *et al.*, 2018), the relationships between animal behavior and neural circuits in the brain (Gradinaru *et al.*, 2009; Chen *et al.*, 2013; Adhikari *et al.*, 2015; Jiang, Tremblay and Elaine Chapman, 2018; Yang *et al.*, 2018), the changes in neural circuitry over time (Jiang, Tremblay and Elaine Chapman, 2018; Yazdan-Shahmorad, Silversmith, *et al.*, 2018), and therapies for neurological disorders (Chen *et al.*, 2013; Tønnesen, 2013; Ruggiero *et al.*, 2017; Barnett *et al.*, 2018;

Camporeze *et al.*, 2018). Optogenetic research in non-human primates (NHPs) is of particular interest in translational medical research because the neurophysiology of NHPs is evolutionarily similar to that of humans. Therefore development of stable, chronic and large-scale optogenetic interfaces for NHPs is critical for long-term experiments in these animals.

Our lab had previously developed novel techniques for optogenetics in NHPs (Ledochowitsch *et al.*, 2015; Azadeh Yazdan-Shahmorad *et al.*, 2016). Specifically, these techniques were: 1- convection enhanced delivery of viral vectors that enabled high levels of expression across large cortical areas, 2- an artificial dura that provided optical access to the large optogenetic expressing areas, and 3- a semitransparent micro-electrocorticographic (µECoG) array that enabled simultaneous neural recording from the affected networks. Our lab also had designed a stimulation setup that enabled positioning of fiberoptics for acute, cortical, non-penetrating optogenetic stimulation and allowed the location of stimulation to be imaged. Collectively, these techniques allowed for large-scale (~2 cm^2) optogenetic experiments across the sensorimotor cortex (Ledochowitsch *et al.*, 2015; Azadeh Yazdan-Shahmorad *et al.*, 2016). However, our lab's techniques and interface had some limitations (Azadeh Yazdan-Shahmorad *et al.*, 2016). Firstly, the placement of the arrays on top of the brain required daily implantation and explantation of the artificial dura. This repetitive tissue manipulation resulted in accelerated tissue growth on the surface of the brain that eventually blocked optical access after about four weeks of experiments. Secondly, the design of our lab's stimulation setup limited the number of fiberoptic cables that could be placed simultaneously on the surface of the brain to two or three locations. This limited the spatial stimulation which could be applied.

Our lab also paired the µECoG array with the artificial dura to enable chronic implantation of the array while maintaining optical access to the brain (Yazdan-Shahmorad *et al.*, 2015). This produced accelerated tissue growth after about 18 days over the top of the array which blocked optical access. Another challenge with this chronic setup was the corrosion of the µECoG array PCBs that were housed in the chamber. To begin addressing these issues, we acutely tested our novel ECoG array called a multi-modal artificial dura (MMAD) (Griggs *et al.*, 2021a) and in this work we demonstrate the MMAD's chronic capabilities.

Here we propose a novel integration of techniques to address the above challenges: 1- we embedded our MMAD into the artificial dura to prevent tissue from growing over the MMAD and to allow optical imaging and months of optogenetic stimulation, 2- we developed moisture-tolerant MMAD cables, which were connected to recording hardware only during experimentation and could be safely housed within the implant between experimental sessions, and 3- we incorporated a non-invasive LED array into the design to allow optical stimulation across ~1 cm^2 of cortex. Collectively, these improvements produce a more robust interface design, which allows for longer and more complex optogenetic experiments. Additionally, our methods are designed to be simple and replicable.

To prepare for surgical implementation, we used our previously published surgical planning method (Ojemann *et al.*, 2020) and designed chambers custom-fit to the skulls of two NHPs. During surgery, we performed convection-enhanced delivery to disperse optogenetic viral vector throughout the posterior parietal region of the cortex and then we implanted the chamber and MMAD in the NHPs. We confirmed optogenetic expression both with epifluorescence and with electrophysiology recording during optical stimulation, and in one animal we slowed his reach in a center-out reach task by deactivating the posterior parietal cortex (PPC) with our custom, non-invasive LED array.

4.2 Methods

We designed as many parts as practical to be 3D-printed in-house with common fused deposition modeling (FDM) polylactic acid (PLA) printers. With the exception of the chamber, which was custom designed for each monkey and chronically implanted, all parts were modular and exchangeable between

animals. Portions of our methods have been previously published (Griggs, Bloch, *et al.*, 2022) and our designs improved upon our previously published concepts (Griggs, Khateeb, Philips, Chan, Ojemann, Yazdan-Shahmorad, *et al.*, 2019; Griggs, Belloir and Yazdan-Shahmorad, 2021).

4.2.1 MMAD

To address tissue growth concerns, we chose to embed our previously published ECoG electrode array, the MMAD (Griggs *et al.*, 2021a), into the artificial dura. We custom-designed a flexible, biocompatible, and semi-transparent MMAD with interleaving conductive layers (250-300 µm trace width with 800 µm pitch) and insulating layers of a transparent medical grade copolymer (50-60 µm thick; Fig. 1A). The arrays consisted of 32 platinum micro-electrodes (~500 µm diameter) covering a 12 mm x 10.5 mm surface area which could be used for both electrical recording and stimulation. The traces extending to many of the 32 electrodes were layered on top of each other, thus increasing the area of optical access. While our previous work included a "light-blocking layer" which demonstrated a reduction in photo-induced artifacts (Griggs *et al.*, 2021a), for this work we chose to forgo the light-blocking layer. We reasoned that this choice would make it more straightforward to determine the presence of photo-induced artifacts during chronic experiments. The MMAD was ultra-flexible because the conductive material was composed of platinum particles dispersed in a matrix within the polymer and featured no printed circuit boards (PCBs). The MMAD was designed in close collaboration with Ripple Neuro (Salt Lake City, UT, USA), who printed the arrays.

The traditional artificial dura, such as the one we used previously (Azadeh Yazdan-Shahmorad *et al.*, 2016), was a single silicone piece composed of a cylindrical wall fitting in the chamber with a flange extending under the native dura to reduce regrowth of the native dura (Fig. 1B). Here, we embedded the MMAD into the artificial dura by first pouring approximately 1 mL of the artificial dura silicone mixture (10:1 ratio of Shin-Etsu silicone KE1300-T and CAT-1300) onto the central cylinder of the mold base. We then placed the MMAD onto the initial silicone layer (Fig. 1C), followed by a second mold piece using two alignment posts as a guide (Fig. 1D). To prevent the silicone from curing on any electrodes, we placed a protective adhesive on the electrode array. We poured approximately 3-4 mL of the silicone mixture into the mold and then the acrylic cover was fitted onto the mold (Fig. 1E) and clamped with a C-clamp. To ensure the MMAD was fully embedded into the artificial dura without gaps, the outer edges of the MMAD were printed to extend radially beyond the electrodes (Fig. 1A) such that the outer edges were embedded within the cylindrical wall of the artificial dura (Fig. 1C-E). We removed any remaining air bubbles in the optical window with pressure induced by clamping the mold assembly during the curing process. We cured the assembly overnight at room temperature. Disassembly of the mold resulted in an artificial dura (skirt diameter: 31.2 mm; skirt thickness: 0.4 mm; wall outer diameter: 21.0 mm; wall inner diameter: 18.6 mm; height: 11.9 mm) with a fully embedded MMAD (Fig. 1F).

4.2.2 Detachable MMAD cables, chamber, and cap

In our previous work, the chronically implanted ECoG array was permanently wired to PCBs which were housed in the implant between experimental trails (Yazdan-Shahmorad *et al.*, 2015). Because the design did not feature a barrier between the cerebrospinal fluid and the PCBs, the PCBs began to corrode over time due to moisture exposure. In this work we solved the corrosion issue by designing the entire MMAD, including the cables, as a flexible, corrosion resistant single piece. The cables of the MMAD could be easily attached to and detached from the electrophysiological recording and stimulation hardware. Between experiments the cables were flexible enough to be housed for long periods within the chamber. Similar to our lab's previous work (Azadeh Yazdan-Shahmorad *et al.*, 2016), the chamber is a cylinder that provides a sturdy base for experimental equipment and protects the brain when the animal is freely moving between experiments. Our lab's previous method of custom fitting the chamber to the skull of the NHP (A Yazdan-Shahmorad *et al.*, 2016) was inadequate for the larger sizes of our proposed chamber.

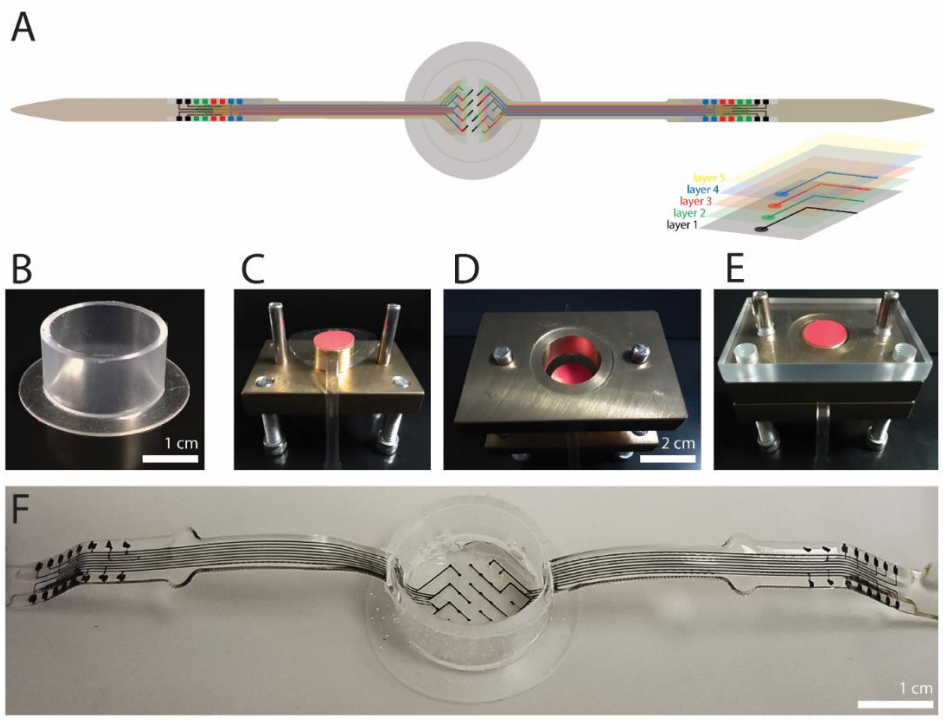

Figure 4.1: MMAD, artificial dura, and molded MMAD. (A) The MMAD was semitransparent and contained individually wired electrodes in the center with 250-300 µm traces embedded within 5 layers of a transparent medical grade copolymer. The traces extended down cables on opposite ends of the centered electrode array. (B) The traditional silicone artificial dura consisted of a cylindrical wall and skirt that extended under the native dura during implantation. (C-E) The mold consisted of the mold base and central cylinder (C), a second mold piece guided into place onto the mold base by two alignment posts (D), and an acrylic cover also guided by the two alignment posts (E). (F) The MMAD consists of the ECoG array embedded within the artificial dura. Reprinted from (Griggs, Khateeb, Philips, Chan, Ojemann, Yazdan-Shahmorad, *et al.*, 2019) *with permission.*

In previous work, we developed a method of extracting the NHP skull curvature from MRI files (Ojemann *et al.*, 2020). In this work, we generated a custom software pipeline (MATLAB, MathWorks, Natick, MA, USA; Solidworks, Waltham, MA, USA) based on past our work (Ojemann *et al.*, 2020) to extract the skull curvature from an MRI file and then use the unique curvature to design a chamber with a unique skull-fitting skirt (Fig. 2A-B). We incorporated concentric tracks within the chamber to store the MMAD cables between experiments (Fig. 2C-D). In addition to the tracks and custom-fit to the skull, the chamber included multiple features: 1- It was made of Ti-6Al-4V (TI-64) which has osteointegration properties, may be 3D printed, and has a high strength to weight ratio, 2- the chamber skirt included 12 holes for skull tap screws (Christ Instruments, Hagerstown, MD, USA), 3- the chamber was hollow (23 mm internal diameter) to provide optical access to the brain, 4- the chamber included an intracranial rim to aid in positioning the chamber on the skull during surgery and to reduce tissue growth around the wall of the MMAD, 5- the chamber was threaded with a high thread pitch (M38 X 1.5) to allow either affixation of experimental equipment or a cap to close the chamber between experiments, and 6- tabs on the outside of the chamber prevented users from screwing equipment too far down the chamber. Fabrication of the chamber (via 3D printing and machining) was performed by Hybex Innovations (Anjou, Quebec, Canada).

We designed a cap (stainless steel 304) to close off the chamber between experiments. We applied polytetrafluoroethylene (PTFE) tape to the threads before each closure to prevent binding of the threads. We used a set screw (HSS11400187HD, #4-40 X 3/16) screwed against the rim of the cap to fasten the cap shut. Machining of the caps was performed by Hybex Innovations.

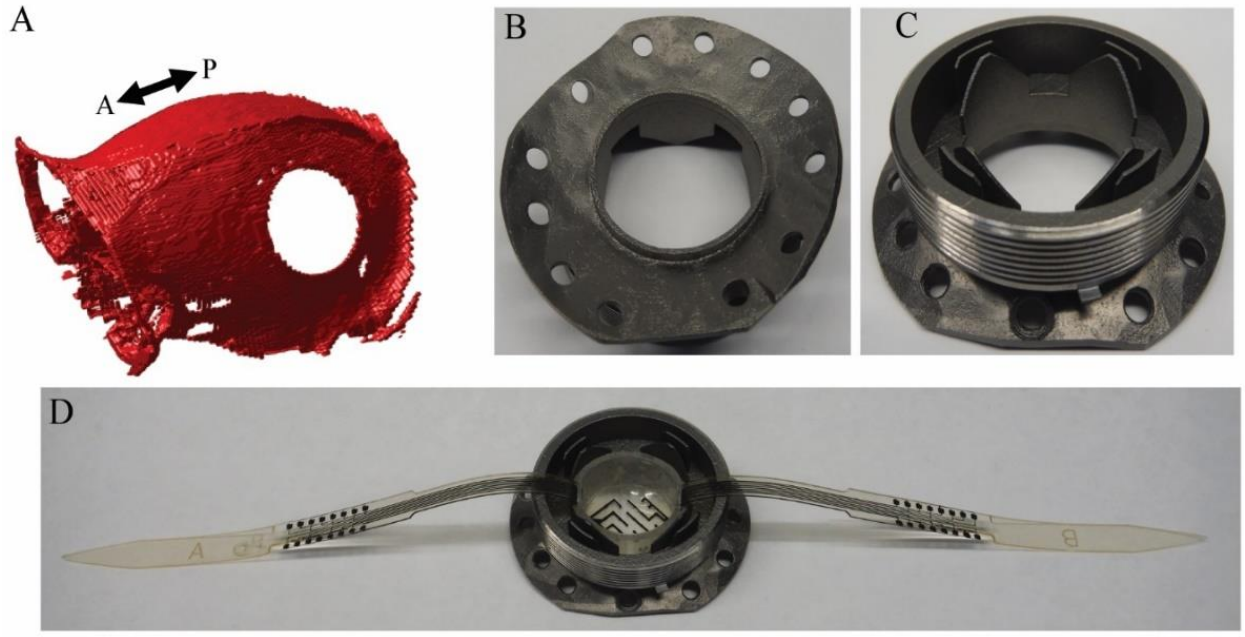

Figure 4.2: Chamber. (A) Model skull extracted from MRI file with proposed craniotomy. (B) Flange of chamber custom-fit to match skull. (C-D) Chamber. The MMAD cables are stored in tracks on the chamber to enable chronic implantation of the MMAD. The screw holes on the flange surface are used to attach the chamber to the skull via skull tap screws. Threading on the outside of the chamber allow the chamber to be closed with a cap or connected to a ring for experimental procedures. Figure adapted from (Griggs, Bloch, *et al.*, 2022)*, which is in press © 2022 IEEE.*

4.2.3 Ring, Tray, and PCB Clamp Connector

The experimental equipment that attached to the chamber is based on our lab's previous work and was modified to exploit the advantages of the MMAD cables. The experimental equipment we propose in this work included a ring, a clamp connector tray, and PCB clamp connectors (Fig. 3A). To prepare the interface for recording and stimulation, we screwed the ring onto the chamber and secured the clamp connector tray onto the ring with 2-4 screws (M2.5 X 6). The ring was machined from stainless steel (304; Hybex Innovations) because of its design simplicity and the clamp connector tray was 3D printed with titanium (TI-64; i.materialise, Leuven, Belgium) due to its design complexity. The ring had 32 screw holes (M2.5) around its rim to offer optimal flexibility in the orientation of attachments. The upper face of the ring included a slight recess just above the threads for additional hardware to be easily aligned with the ring for fastening. The bottom of the clamp connector tray included a lip around the window to fit into the recession of the ring. The base of the tray included a right-angled outer rim for grounding electronics as well as four elevated screw holes (M2.5 or 4-40 thread) designed to allow optical stimulation equipment to be secured to the tray. The tray was compatible with both our lab's previous fiberoptic-based setup and our proposed LED-based optical stimulation setup (section 2.3.4). The arms of the tray were designed to be low weight and provide support for the MMAD cables as they extended from the artificial dura walls upwards and at an angle. The tip of the tray arm was approximately 9.5 cm away from the cranial window. The arms of the tray supported PCB clamp connectors (Fig. 3A) held in place by rubber bands (not shown), which secured the MMAD cables approximately 4.5 cm away from the brain and provided an electrical connection between the cables and commercial neurophysiology equipment (Grapevine Nomad, Ripple Neuro). The PCB clamp connectors were designed and manufactured by Ripple Neuro. Two of these setups may be simultaneously deployed on the same animal, one on each hemisphere, although we have only performed one craniotomy per animal.

4.2.4 Optical Stimulation Setup

To optically stimulate across large cortical areas, we incorporated a 4 x 4 LED array (Fig. 3C) inspired by previous work (Rajalingham *et al.*, 2021). This enhancement increased our optical modulation area from 2-3 points (Yazdan-Shahmorad *et al.*, 2015; A Yazdan-Shahmorad *et al.*, 2016) to ~1 cm^2. To prevent the LED array from moving when in use, we designed a system involving a rod, tube, coverslip, and base (Fig. 3B). We custom designed and 3D printed the rod, tube, and base with FDM PLA in-house. We glued (Better Ultimate Adhesive, slow dry, Cemedine Co. Ltd., Shinagawa City, Tokyo, Japan) the coverslip (Ø 16 mm) to one end of the tube. The base, which we affixed to the clamp connector tray, secured the coverslip against the top side of the MMAD and a set screw (HSS11400187HD, #4-40 X 3/16) secured the rod inside the tube. The rod positioned the LED array over the brain and above the coverslip. Our setup created an air gap between the LEDs and the coverslip, which protected the brain from conductive heating. Four long screws in the base secure the tube in place.

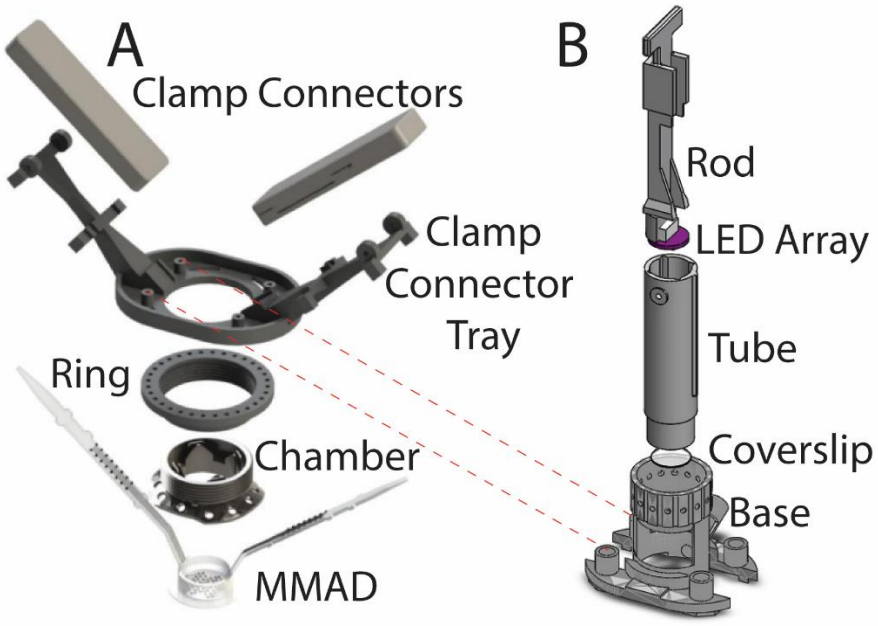

Figure 4.3: Neurophysiology recording setup. (A) The MMAD was inserted into the chamber. A ring was screwed onto the chamber to support the clamp connector tray. The MMAD cables connected to the PCB clamp connectors, which were placed on the arms of the clamp connector tray. (B) The LED array was connected to the end of a rod, which slid through a tube, which was capped by a coverslip. This eliminated the need for the LED array to be sterilized before use and protects the brain from heating due to optical stimulation. The tube was inserted through the base, which was screwed to the tray. The base provided some flexibility in the location and angle of tube insertion and the tube was locked into place with screws (not shown) near the top of the base. Figure adapted from (Griggs, Bloch, *et al.*, 2022)*, which is in press © 2022 IEEE.*

The LED array consisted of a circular custom rigid printed circuit board (PCB; 15.5 mm diameter) printed with standard PCB printing services (OSH Park, Portland, OR, USA). The PCB was wired to drive four individually addressable rows of LEDs (L1C1-RED1 or L1C1-BLU1, Lumileds, Schipol, Netherlands) and included an internal copper plane for heat dissipation. We soldered 16 LEDs in a 4-by-4 grid on one side of the PCB and a connector (501331-0807, Molex Inc., Lisle, IL, USA) on the other side. We drove the LED with a custom external PCB (OSH Park) connected to the LED array by a cable assembly (151330806, Molex Inc.). The external PCB consisted of four voltage controlled current sources, one for each row of LEDs. Each driving circuit consisted of a high output current opamp (TLE2301, Texas Instruments, Dallas, TX, USA) and a high-power resister (15 Ω, 5 W power rating, SMW515RJT, TE Connectivity, Schaffhausen, Switzerland), where the resister value controls the ratio of input voltage to output current. The input

voltage is provided by our neurophysiology system's analog voltage output (Ripple Neuro). The input voltage is prevented from floating (e.g. when the neurophysiology system is turned off) by a pull down resistor (10 kΩ). We drove our PCBs with two in-series batteries (9V Li-ion rechargeable, Keenstone, Industry, CA, USA) to reduce line noise in our electrophysiological recordings. We depict our circuit in Fig. 4.

We also designed our clamp connector tray to be compatible with our previous laser stimulation setup (Yazdan-Shahmorad *et al.*, 2015), and its slightly modified version briefly described here. Our setup was composed of a base (similar to the base for the LED array setup) and stimulation ring, both FDM 3D-printed in-house with black PLA. The base was screwed to the clamp connector tray. The stimulation ring guided telescoping cannulas (HTX-13R, HTX-16T, and HTX-18T, Component Supply Co., Sparta, TN, USA) to different stimulation locations, and optical fibers driven by lasers (520 nm or 638 nm, LDFLS_520_520_638_638, Doric Lenses, Quebec, Canada) were slid through the cannulas.

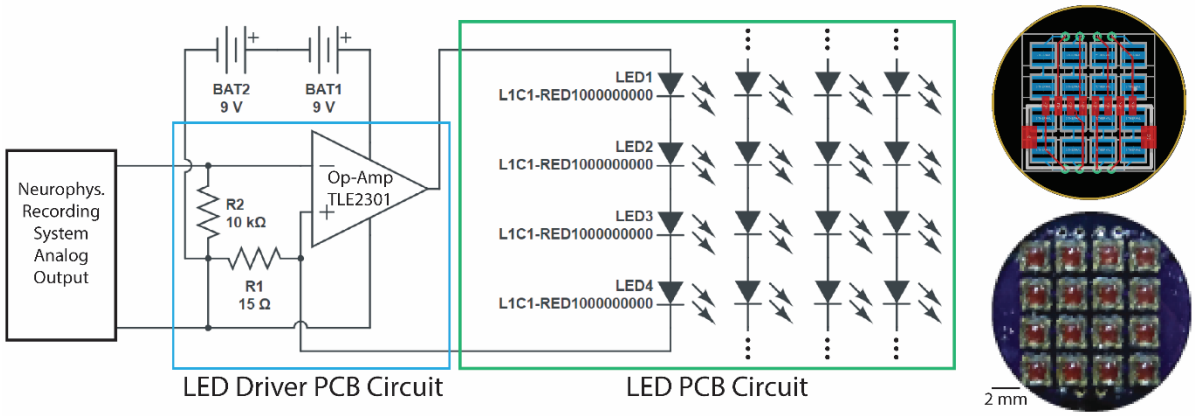

Figure 4.4: LED array and circuitry. The circuitry is powered by batteries and driven by a neurophysiology system. The circuitry consists of two PCBs, being the driver on the bench and the LED array acutely implanted during experiments. The LED PCB schematic and final product are shown on right. Figure adapted from (Griggs, Bloch, *et al.*, 2022)*, which is in press © 2022 IEEE.*

4.2.5 Animals

We utilized two healthy, socially housed male rhesus macaques (*Macaca mulatta*; Monkey H: 9 y, 13 kg; Monkey L: 9 y, 11 kg) for this study. Water was available *ad libitum* and no feeding restriction or scheduling protocols were used. All animal care and experiments were approved by the University of Washington's Office of Animal Welfare, the Internal Animal Care and Use Committee, and the Washington National Primate Research Center.

4.2.6 Surgical procedures

We used surgical procedures on both animals similar to those we previously published (A Yazdan-Shahmorad *et al.*, 2016) and we briefly describe them here. We sedated the animal and shaved his head before anesthetizing and head-fixing him in a stereotactic frame. The respiratory rate, heart rate, and body temperature of the animal were monitored throughout the procedure. We created an incision several cm long to the left of the head's midline and used elevators to peel back the skin, musculature, and muscle fascia. Then we test-fitted a plastic version of the chamber to the skull and marked the center of the craniotomy. We confirmed the location of the center of the craniotomy with stereotactic coordinates. Using a 25-mm diameter trephine, we resected the skull. Then we resected the dura by lifting the dura with a curved needle and trimming with ophthalmic scissors, revealing the posterior parietal cortex. After test-fitting the titanium chamber to the skull, we placed a flat transparent silicone artificial dura on the brain to keep the brain moist.

With the craniotomy complete, we performed convection-enhanced delivery (CED) of the Jaws opsin (rAAV8/hSyn-Jaws-KGC-GFP-ER2, 5.4 x 10^{12} virus molecules/mL, University of North Carolina Vector Core), a red-shifted inhibitory viral vector, which has previously been used to evoke behavioral effects in NHPs (Chuong *et al.*, 2014; Acker *et al.*, 2016). Prior to surgery we had manufactured a 1-mm stepped-tip silica cannula (inner cannula: ID 320 µm, OD 435 µm; outer cannula: ID 450 µm, OD 673 µm; Polymicro Technologies, Phoenix, AZ, USA) for CED similar to our previous work (A Yazdan-Shahmorad *et al.*, 2016; Griggs, Garcia, *et al.*, 2022). We removed the artificial dura from the brain, punched a hole through it, laid the artificial dura back on the brain, and then inserted the cannula tip through the hole in the artificial dura and approximately 2 mm into the cortex and began the infusion protocol similar to our precious work (A Yazdan-Shahmorad *et al.*, 2016). We infused at several locations across the visible cortex. Unlike our previous work where we performed live MRI during infusions (A Yazdan-Shahmorad *et al.*, 2016; Karam Khateeb, Griggs, *et al.*, 2019), we elected to monitor the infusions by eye. Once complete, we placed a new artificial dura on the brain.

Following CED, we placed the chamber on the skull. We used a piezo-drill to drill screw holes and we used skull tap screws (Crist Instruments) to secure the chamber to the skull. We removed the artificial dura and placed the MMAD on the brain and coiled the cables in the slots of the chamber (Fig. 5). Finally, we applied PTFE tape to the threads, closed the cap, secured the set screw, and applied bone wax to the set screw. Having secured and closed the chamber, we closed the wound using standard surgical techniques. Following the surgery, the animal was placed on oral antibiotics for 4-5 weeks.

We had implanted a headpost (Crist Instruments) on each animal prior to this study (Ojemann *et al.*, 2020).

Figure 4.5: Chamber and MMAD implanted prior to cap being placed during surgery. MMAD arms coiled in slots.

4.2.7 Chamber cleaning and hardware assembly

We developed a process of cleaning the chamber at least three times each week, starting one week after the surgery, and assembling hardware on the chamber for experimentation. After head-fixing the animal, we began by trimming scalp hair in the vicinity of the chamber. Then we cleaned the cap, chamber margin, surrounding scalp and outside of the ear with a cleaner (Hibiclens, Mölnlycke Health Care, Norcross, GA,

USA), then with 70% ethanol to remove all cleaner, and then repeated the cleaning at least once more. Once clean, we loosened, but did not remove, the cap's set screw. To loosen the cap, we wiped down our nitrile gloves and large pliers (straight jaw, Channellock Inc., Meadville, PA, USA) with ethanol and used the pliers to apply the necessary torque. Then we removed the cap by hand.

To begin cleaning the chamber, we removed PTFE from the chamber threads with sterile forceps. We dipped sterile cotton-tipped applicators into sterile saline and used them to clean the margin. During this step we occasionally used sterile forceps to aid in the removal of buildup in the margin and sterile scissors to perform additional hair trimming. After cleaning the margin, we used cotton-tipped applicators dipped in saline to clean the threads and the rim of the chamber. To clean the inside of the chamber, we used a sterile syringe and blunt-tipped needle to spray warm saline on and in the MMAD, its cables, and the storage area for the cables. We removed the saline during rinses with a sterile suction tip.

To prepare for electrophysiological recording, we screwed a sterile ring onto the chamber the screwed a sterile clamp connector tray to the ring with sterile screws. Then we draped sterile gauze over the side of the animal's head and ear. Using fresh sterile forceps, we removed the cables from the chamber and draped them down onto the sterile gauze. Then we wiped the cables with sterile saline, dabbed them dried them with gauze, placed them into the clamp connectors, and rubber banded the clamp connectors to the clamp connector tray arms. Note that the clamp connectors were never sterilized. Finally, we removed the sterile gauze.

From here we attached the non-sterile base for either the LED array or for the lasers. We wiped the bottom of the base with povidone iodine because parts of it would touch the sterile screw posts of the clamp connector tray, then we screwed the base to the clamp connector tray. In the case of laser stimulation, we slid the stimulation ring down around the base. We inserted the fiberoptic cable through the cannula and wiped down the tips of each with alcohol, then we inserted the cannula through the simulation ring until the fiberoptic cable came into contact, or nearly into contact, with the MMAD. In the case of LED stimulation, we assembled the LED array, rod, and tube with coverslip, and secured them together with a set screw. Then we wiped down the coverslip and about 3 cm of tube with povidone iodine. We did not clean the tube with alcohol to avoid degrading the glue holding the coverslip to the tube. Then we wiped off the povidone iodine with sterile gauze dipped in sterile saline, and then dried the coverslip and tube with sterile gauze. Once the end of the tube had been cleaned, we lowered the assembly down through the base and into the MMAD, and secured the tube into place with set screws. Black foil was wrapped around the stimulation equipment to prevent the animal from seeing any lighting changes due to stimulation.

When experimentation was complete, we removed the stimulation equipment and draped sterile gauze over the side of the animal's head and ear. We removed the cables from the clamp-connectors, wiped them with povidone iodine followed by sterile saline, and draped them onto the sterile gauze. We removed the clamp connectors from the clamp connector tray and draped sterile gauze over the clamp connector tray arms because they were no longer sterile. Then we used sterile forceps to place the cables into the chamber as shown in Fig. 5. Once the MMAD was in place, we removed the clamp connector tray and ring from the chamber.

To prepare for chamber closing, we repeated the saline rinse several times. We also used saline to rinse the gap between the walls of the MMAD and the inner diameter of the chamber, but this was done with special care to avoid any direct or indirect manipulation of the underlying neural tissue, which can result in accelerated tissue growth. If a chamber infection was known or suspected, we also rinsed several times with saline mixed with a small amount of povidone iodine such that the saline was lightly tinted. We

followed these povidone iodine rinses with additional saline rinses to ensure betadine would not be in the chamber at final closing. We wiped the chamber threads and rim with alcohol.

Then we applied antibiotic to the center of the MMAD. We did not apply antibiotic during initial surgery recovery because the animal was given oral antibiotics. To avoid building antibiotic resistance, we changed antibiotics approximately every 4-5 weeks. Except for the initial surgery recovery, we rotated through polymyxin B sulfate, gentamicin, and amikacin sulfate.

To prevent the cap from binding to the chamber between cleanings, we wrapped a strip of sterile PTFE around the threads (or at least a portion of the threads). Then we screwed a sterile cap on and tightened by hand. We loosened the set screw and checked that the cap was still tight and had not tightened onto the set screw, then we tightened the set screw and applied bone wax to the screw. Finally, we returned the animal to his cage.

4.2.8 Behavioral task

We trained the animals to perform a center-out reach task. The task began with a green initial circle appearing in the center of a screen. When the animal placed his finger into the initial circle, a red target circle would appear in one of four different reach directions (up, down, left, or right). The appearance of the target circle coincided with the onset of stimulation. After a random delay of up to several hundred ms, during which the animal held his finger in the initial circle, a go-tone would play and the animal would touch the target circle and earn a juice reward (5-RLD-D1 D.A.R.I.S., Crist Instruments). The task was developed in and operated by MATLAB with Psychophysics Toolbox version 3 (Brainard, 1997; Pelli, 1997; Kleiner, Brainard and Pelli, 2007), similar to our previous work (Griggs *et al.*, 2020).

We placed a reflective sticker on the middle finger of the animal's right hand and used a tracking system (Motive, OptiTrack, NaturalPoint Inc., Corvallis, OR, USA) to track the movement of the animal's finger, and the data was delivered to MATLAB for live processing. We displayed a cursor, being a small white circle, on the screen when the marker was close to the screen. During the task, the animal was head-fixed and in a dark experimental rig.

4.3 Results

Portions of our results have been previously published (Griggs, Bloch, *et al.*, 2022).

4.3.1 Optical window stability

For Monkey H, we imaged the brain weekly through the MMAD and observed only modest tissue growth over the first 14 weeks after implantation (Fig. 6A). After 14 weeks, we performed an experiment unrelated to this work that facilitated tissue growth, likely due to tissue heating.

For Monkey L, we observed blood between the MMAD and the brain after surgery, obscuring the brain. The optical window remained at least partially obscured for about four weeks after surgery, at which point we observed some tissue growth partially blurring the surface of the brain. The brain stayed this way for about 1.5 weeks before a series of issues, such as tissue growth and blood on the brain, obscured optical access again. 10 weeks after surgery we resected the dura and swapped out the MMAD for a classic artificial dura which resulted in blood heavily obstructing optical access for 2 weeks, after which the optical window cleared and revealing the cortex with little to no tissue growth until the time of writing, which was about 3 weeks.

4.3.2 Opsin epifluorescence

We started monitoring optogenetic expression with epifluorescent imaging two weeks after infusion of Monkey H and stopped six weeks after infusion. Expression was apparent during the first imaging session

and increased in coverage and intensity until the fifth week after infusion, where expression plateaued at tens of mm^2 coverage (Fig. 6B). We performed epifluorescent imaging four and five weeks after infusion of Monkey L and also identified large-scale expression, despite aforementioned tissue growth (section 2.4.1). 13 weeks after infusion, we performed epifluorescent imaging again, this time with little to no tissue growth impeding optical access, and we confirmed tens of mm^2 expression coverage (data not shown). These large areas of coverage are comparable with our previous work (A Yazdan-Shahmorad *et al.*, 2016) and are important proofs of concept for our novel method of optogenetic CED in NHP cortex without live MRI guidance, which contrasts with much of our past work that used live MRI guidance (A Yazdan-Shahmorad *et al.*, 2016).

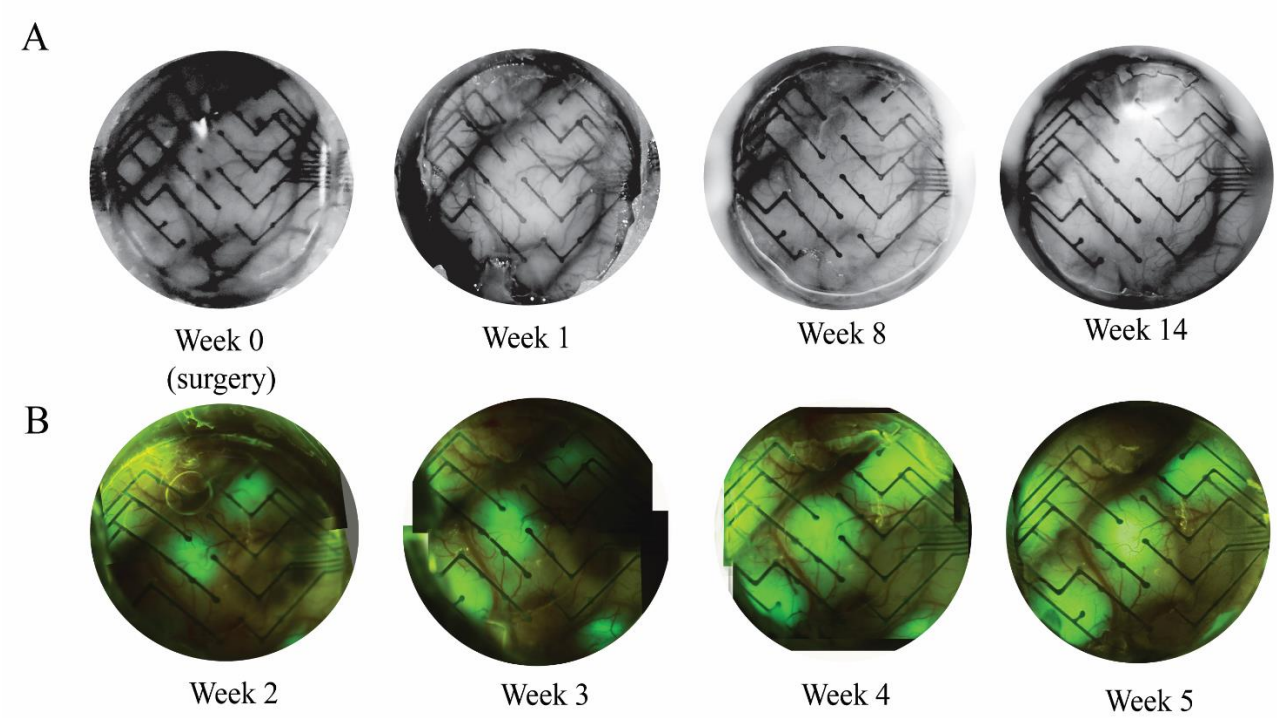

Figure 4.6: Imaging Monkey H. (A) Optical window stability. (B) Epifluorescence imaging of Jaws opsin expression. Weeks 2, 3, and 4 are composed of several images stitched together. Week 5 is composed of a single image. Figure adapted from (Griggs, Bloch, *et al.*, 2022)*, which is in press © 2022 IEEE.*

4.3.3 Optogenetic Modulation

Using our laser setup eight weeks after infusion of Monkey H, we illuminated neural tissue with fiberoptic cable near selected electrodes and evoked spatially specific changes in our ECoG signal confirmed with various illumination parameters (for example, Fig. 7A). Nine weeks after infusion, we tested our LED setup by illuminating the PPC (~1 cm^2) with the entire LED array while varying the illumination parameters (for example, Fig. 7B). To characterize the response, we calculated power spectral densities (PSD) of our ECoG recording from before and during stimulation (Fig. 7C). The comparison between the ratio of the PSD during and before stimulation, with that of similar data collected in saline, indicated successful neuromodulation, including depression in the 8-39 Hz range (Fig. 7D). Further investigation is needed to elucidate the intricacies of our spectral results.

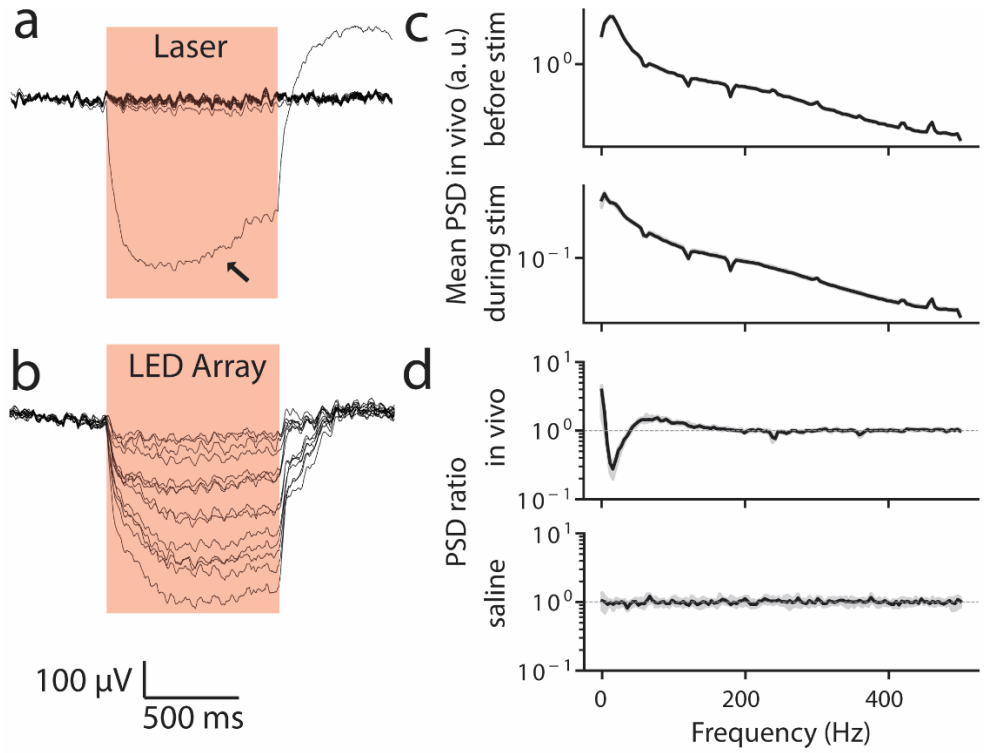

Figure 4.7: Neurophysiology. (a) Time-averaged wideband signals from laser light illumination (30 pulses, 900 ms per pulse at 110 mA, 27 mW optical power) in vivo. The stimulated channel is indicated with an arrow. Stimulation times are shown in red. (b) Time-averaged wideband signals from 30 pulses of the full LED array illumination (30 pulses, 900 ms per pulse at 700 mV, ~2.4 mW/mm^2 optical power) in vivo. (c) Averaged power spectral density (PSD) before (top) and during (bottom) LED array stimulation in vivo. (d) Ratio of the PSD (during stim / before stim) for in vivo (top) and saline data (bottom). Dashed line indicates no change. Data above the dashed line indicated excitation, and below the line indicates inhibition. Shaded error bars are 95% confidence interval of median. Figure adapted from (Griggs, Bloch, *et al.*, 2022)*, which is in press © 2022 IEEE.*

4.3.4 Behavioral effect of stimulation

We trained the subjects to perform a center-out reach task using the hand contralateral to the implant. We stimulated for 900 ms with all LEDs of our LED array (634 nm, ~12 mW/mm^2) during a random subset of the trials, where the beginning of the stimulation aligned with the go-tone. The subjects performed several hundred trails each day for a few days. With Monkey H, we observed stimulation-slowed reaches in two of the four directions. When all directions were pooled together, we found a statistically significant average stimulation-induced delay. With Monkey L, we observed similar stimulation-slowed reaches as well as a correlation between trial success and stimulation, and both findings (no shown) were under further investigation at time of writing.

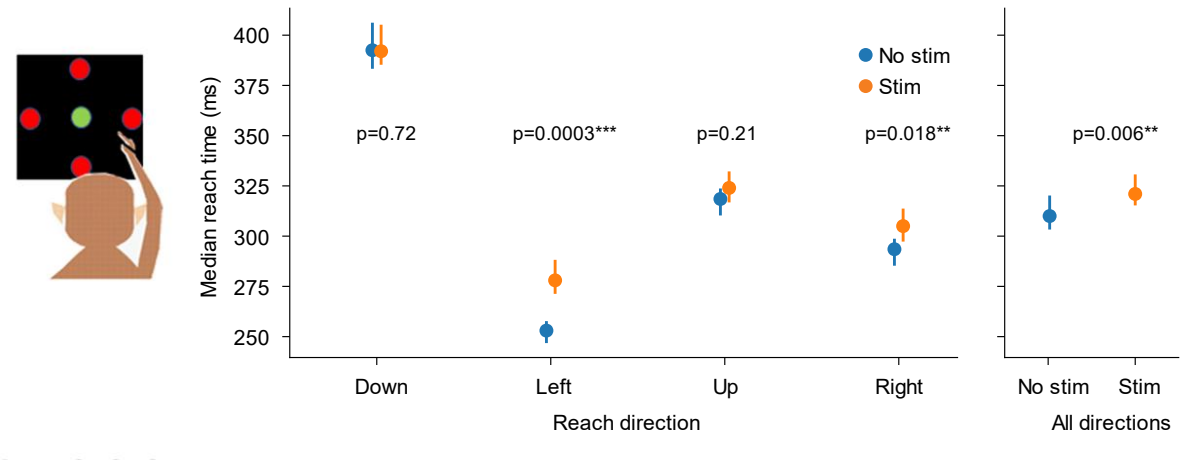

Figure 4.8: Behavioral results. Stimulation increased median reach time in two of four directions in a center-out reach task, and pooled results also showed an increase in reach time. For each direction, N ≈ 10^3. The p-values were calculated with a Man-Whitney U-test. Scale bars are 95% confidence intervals generated with a bootstrapping procedure.

4.4 Discussion

4.4.1 Innovations

One of the major challenges in optogenetics research is optical access, especially at the large scales necessary to study complex network interactions across multiple brain regions *in vivo* in NHPs. One approach to this challenge is resecting both the skull and the opaque native dura and implanting transparent artificial duras. The artificial duras are biocompatible and can provide optical access to the brain for 3-9 months (Arieli, Grinvald and Slovin, 2002; Chen *et al.*, 2002; Azadeh Yazdan-Shahmorad *et al.*, 2016) before tissue growth stifles optical access (Azadeh Yazdan-Shahmorad *et al.*, 2016). This tissue is a neo-membrane and cannot be easily removed during early stages of growth because it is nourished through the brain. The tissue can be surgically removed once the neo-membrane separates from the brain. This growth process forces the researchers to wait for about one to two months before resuming experimentation. Extending the window of efficient optogenetic experimentation is important for reducing the frequency of these delays. In our lab's previous work, an array of micro-electrodes was embedded into Parylene-C, a flexible, biocompatible polymer, and it was implanted under a transparent silicone artificial dura in order to achieve simultaneous electrical recording and optical stimulation (Yazdan-Shahmorad *et al.*, 2015; Azadeh Yazdan-Shahmorad *et al.*, 2016). Our lab was surprised to find that the brain exhibited such a high biocompatibility with Parylene-C that the tissue quickly grew over the top of the Parylene-C during the experiments and allowed for only about 13-18 days of optical access (Yazdan-Shahmorad *et al.*, 2015). Here we had an MMAD fabricated by embedding electrodes into a polymer similar to silicone used in artificial duras. We then incorporated the array into the artificial dura to create a single MMAD. Our demonstrated 3+ months of optical access indicate that the brain's response to this integrated approach is similar to silicone artificial duras and facilitates long-term optogenetic experiments with electrical recording. Also, the chronic MMAD eliminates the need for daily implantations and explanations that accelerated tissue growth and were time consuming for the experimenters (A Yazdan-Shahmorad *et al.*, 2016). We are among the first to embed an ECoG array into an artificial dura (Orsborn *et al.*, 2015; Kleinbart *et al.*, 2018; Chiang *et al.*, 2019; Chiang, Won, *et al.*, 2020), and to our knowledge we are the first to use this embedded approach chronically in NHPs for large-scale imaging in addition to electrophysiology and optogenetics. Of note, optogenetics, ECoG, and optical imaging have been performed simultaneously in rodents (Chen *et al.*, 2020).

Another challenge of neural interfaces is protecting the electronics from moisture and fluids. For example, our lab's previous interface left PCBs within the chamber and subject to chronic moist conditions. Here we addressed this problem by using a corrosion resistant MMAD with flexible cables which can be extended to external neural recording equipment during experimentation and housed within the chamber when not in use.

We designed our interface to be modular and replicable in a number of ways. Our MMAD molding process does not require any special facilities or tools aside from the custom mold pieces. We based our chamber design process on our previously published skull modeling method (Ojemann *et al.*, 2020), and we plan to make our updated process publicly available upon publication of this manuscript. The ring and clamp connector tray facilitate experimental flexibility for electrophysiological recording, imaging, both fiberoptic- and LED-based optical stimulation, and future component designs. Most of the optical stimulation components (bases, stimulation ring, rod, and tube) can be 3D printed in-house with common filament and printers, which facilitates quick and inexpensive revisions for unique experimental needs. Parts can be soldered onto the LED-related PCBs in-house with minimal experience, and the simplistic circuitry was designed to protect against line noise. The behavioral task was based off of our previously published work (Griggs *et al.*, 2020), and our code was written in MATLAB, which is a common software language among researchers. We plan to make the behavioral task code and the design files of our electronic and hardware parts publicly available upon publication of this manuscript. Collectively, our methods make cutting-edge neuroengineering techniques approachable to monkey researchers with diverse expertise. Our lab's previous stimulation setup allowed for the optical stimulation of only two or three point-locations at a time due to the physical interference of fiberoptic wires within the enclosure (Azadeh Yazdan-Shahmorad *et al.*, 2016). In contrast, our 4 x 4 LED array provides broad, non-invasive optical modulation and eliminates concerns regarding fiber fragility. To our knowledge, we have performed one of the largest-scale optogenetic inhibitions (as measured by surface area) in all of neuroscience. Having collected tantalizing ECoG and behavioral data with this LED array, we anticipate development of higher-count and multicolor LED arrays to further complement our large-scale optical interface.

Importantly, our work has demonstrated large-scale optogenetic success by three key measures: epifluorescence imaging, electrophysiology, and behavior. Together, these data validate our chronic setup and indicate that our method is suitable for fostering large-scale optogenetic experimentation in NHPs.

4.4.2 Limitations

The polymer used for the MMAD is appropriate for transmission of visible light and protects the wires from damage during manipulation while also allowing for the long, flexible cables to be easily oriented for both storage and experimental use. These benefits come with three drawbacks: 1- the electrodes are bigger than those our lab has previously used (Ledochowitsch *et al.*, 2015; Azadeh Yazdan-Shahmorad *et al.*, 2016) and therefore provide recordings with lower spatial resolution, 2- the electrodes themselves are not transparent, contrary to our lab's previous demonstration (Ledochowitsch *et al.*, 2015), and 3- the platinum-polymer matrix printing technology imposes an upper limit of 32 electrodes in the MMAD which is fewer than our lab has used previously (Ledochowitsch *et al.*, 2015; Azadeh Yazdan-Shahmorad *et al.*, 2016). We are collaborating with Dr. Maysam Chamanzar from Carnegie Mellon University to develop a µECoG array which addresses these limitations and still allows for optogenetics and imaging. We also plan to incorporate LEDs into the µECoG array (Reddy *et al.*, 2019). To our knowledge, a device of this kind has not yet been chronically demonstrated in NHPs.

Our work does not report histological analysis of optogenetic expression because the animals are still on study. However, the epifluorescence imaging, electrophysiology, and behavior, when taken collectively, strongly suggest robust, large-scale optogenetic expression.

4.4.3 Research opportunities

Our interface opens the door for investigation into a variety of questions which require flexible control of neural activation with high temporal and spatial precision. For example, this interface will better enable the study of functional connectivity between different cortical areas (Yazdan-Shahmorad, Silversmith, *et al.*, 2018; Bloch *et al.*, 2019, 2022). This interface will also allow for the study of neurological disorders such as stroke, which is a particularly prevalent area of research in the cortex (Choi *et al.*, 2018; Frías *et al.*, 2018; Obi, Amano and Takatsuru, 2018; Yazdan-Shahmorad, Silversmith, *et al.*, 2018; K Khateeb *et al.*, 2019; Khateeb *et al.*, 2022; Zhou *et al.*, 2022). Importantly, our proposed interface is compatible with our lab's photothrombotic stroke model (Yao and Yazdan-Shahmorad, 2018; K Khateeb *et al.*, 2019; Griggs, Belloir and Yazdan-Shahmorad, 2021; Khateeb *et al.*, 2022; Zhou *et al.*, 2022).

Notably, our interface has been purposely designed to accommodate both optogenetic and electrical stimulation. This confluence of stimulation modalities allows this interface to be used to compare their differing effects. Research in this area is important because optogenetic stimulation is still largely in a preclinical stage, yet may reveal diagnostic or therapeutic opportunities. In such a scenario, an interface allowing parallel development of both optogenetic and electrical stimulation protocols could speed the translation of the new diagnostic or therapeutic techniques from animals to humans.

We believe that our proposed interface techniques will advance our understanding of neuroplasticity and functional connectivity. We anticipate that energy storage technologies, high channel-count closed-loop systems, and wireless data transfer technologies will be integrated into designs based on our interface to make our work practical for experimentation on freely moving animals. This would further open the door for the advancement of translational optogenetic recovery models for neurodegenerative diseases, stroke, and traumatic brain injury.

4.5 Acknowledgment

We thank WaNPRC staff for their help with animal care and surgeries. We thank Ripple Neuro, and especially Alex Johnson, Jose Ortega, and Jessi Michel, for their help with designing and manufacturing the MMADs.

I would like to thank my advisor Azadeh Yazdan-Shahmorad for her invaluable guidance and support throughout all aspects of this project. I would also like to thank the rest of my lab for their support, especially Julien Bloch, William Ojemann, Tiphaine Belloir, Shawn Fisher, Karam Khateeb, Kali Coubrough, Marcus Chu, Jia Wen Chan, and Stephen Phillips for their help preparing the conference papers on which this manuscript is based (Griggs, Khateeb, Philips, Chan, Ojemann, Yazdan-Shahmorad, *et al.*, 2019; Griggs, Belloir and Yazdan-Shahmorad, 2021; Griggs, Bloch, *et al.*, 2022).

Chapter 5: Improving the efficacy and accessibility of intracranial viral vector delivery in non-human primates

This chapter is representative of work which is complete and published. Reprinted with permission. Please cite the final published version of this work:

> **Griggs DJ***, Garcia AD*, Au WY, Ojemann WKS, Johnson AG, Ting JT, Buffalo EA, Yazdan-Shahmorad A. 'Improving the efficacy and accessibility of intracranial viral vector delivery in non-human primates,' *Pharmaceutics, Special Issue "Brain-Targeted Drug Delivery.* 2022, 14, 1435. https://doi.org/10.3390/ pharmaceutics14071435

5.0 Abstract

Non-human primates (NHPs) are precious resources for cutting edge neuroscientific research, including large-scale viral vector-based experimentation such as optogenetics. We propose to improve surgical outcomes by enhancing surgical preparation practices of convection-enhanced delivery (CED), which is an efficient viral vector infusion technique for large brains such as NHPs'. Here we present both real-time and next-day MRI data of CED in the brains of ten NHPs, and we present a quantitative, inexpensive, and practical bench-side model of the *in vivo* CED data. Our bench-side model is composed of food coloring infused into a transparent agar phantom, and the spread of infusion is optically monitored over time. Our proposed method approximates CED infusions into the cortex, thalamus, medial temporal lobe and caudate nucleus of NHPs, confirmed by MRI data acquired with either gadolinium-based or manganese-based contrast agents co-infused with optogenetic viral vectors. These methods and data serve to guide researchers and surgical team members in key surgical preparations for intracranial viral delivery using CED in NHPs, and thus improve expression targeting and efficacy and, as a result, reduce surgical risks.

5.1 Introduction

The development of novel tools to genetically alter the properties of neurons has been instrumental in expanding the scope of neuroscientific questions. Perhaps one of the most popular of these genetic modification methods is optogenetics, through which cells can be made susceptible to rapid, reversible manipulations via light stimulation. This technique was first demonstrated in 2005 (Boyden *et al.*, 2005) and since then has been robustly developed and widely adopted. In particular, optogenetics has become a powerful tool for rodent neuroscience (Yizhar *et al.*, 2011; Ting and Feng, 2014). The high-throughput nature of experiments with these models means that researchers can pilot, experiment, and make corrections with new subjects rapidly and with minimal resources. Additionally, the rapid gestational time (~1 month for most research species) and large litter size (4-12 pups/litter) of these models extends the genetic modification toolkit of rodent researchers to allow for breeding genetically altered lines and testing transgenic subjects with relative ease. However, transgenic lines are largely unavailable for highly translational non-human primate (NHPs) models. In contrast to rodents, the macaque has a gestational period of ~6 months and gives birth to singular offspring, which eliminates the practical viability of transgenic approaches. This leaves viral vector transfection as the primary method of preparing NHPs for experiments requiring genetic modification. However, this experimental approach still proves to be a challenging, and potentially costly, endeavor. Here, we present novel and updated methods that eliminate several of the main dissuading factors of transduction studies in NHPs.

Convection enhanced delivery (CED) is an infusion technique which has been developed over the past few decades to deliver medicinal agents to the brain (Mehta, Sonabend and Bruce, 2017; René and Parks, 2021). Classic neural infusion techniques rely on diffusion which is based on a concentration gradient and therefore is heavily influenced by molecular weight (Hunt Bobo *et al.*, 1994). Large molecules like viral

vectors are inefficiently spread by diffusion. By contrast, CED capitalizes on a pressure gradient for delivery which is much less influenced by molecular weight and comes with a number of benefits over diffusion: 1- CED can be performed at higher delivery rates (on the order of 1 µL/min or higher) which speeds up delivery (Michal T. Krauze *et al.*, 2005; A Yazdan-Shahmorad *et al.*, 2016; Yazdan-Shahmorad, Tian, *et al.*, 2018), 2- CED can distribute agent over greater volumes (hundreds of mm^3) (A Yazdan-Shahmorad *et al.*, 2016; Yazdan-Shahmorad, Tian, *et al.*, 2018), 3- CED produces a roughly uniform concentration of agent throughout the distribution volume (Hunt Bobo *et al.*, 1994; Lieberman *et al.*, 1995; Lonser *et al.*, 1998, 2002; Michal T. Krauze *et al.*, 2005; Sanftner *et al.*, 2005; Szerlip *et al.*, 2007), and 4- as previously alluded, CED is effective at transporting large molecules, such as viral vectors, throughout regions of the brain (Lonser *et al.*, 1998, 2002; Michal T. Krauze *et al.*, 2005; Sanftner *et al.*, 2005; Szerlip *et al.*, 2007; Kells *et al.*, 2009).

Incentivized by these desirable properties, we have used CED in recent years to deliver optogenetic viral vectors into the brains of non-human primates for neuroscientific experiments (Yazdan-Shahmorad *et al.*, 2015; A Yazdan-Shahmorad *et al.*, 2016; Yazdan-Shahmorad, Tian, *et al.*, 2018; S L Macknik *et al.*, 2019). To compliment the technique, we have utilized a method of real-time infusion validation with magnetic resonance imaging (MRI) technology using a gadolinium-based contrast agent co-infused with the optogenetic viral vector (Karam Khateeb, Griggs, *et al.*, 2019). We previously validated the resulting optogenetic expression with epifluorescence imaging, electrophysiology, and histology (A Yazdan-Shahmorad *et al.*, 2016; Yazdan-Shahmorad, Tian, *et al.*, 2018). However, we recognize that not all institutions have access to an MRI scanner in which live validation of an injection can be visualized. Thus, a separate set of CED experiments without live MRI guidance was performed using novel optogenetic viral vectors co-infused with a manganese-based contrast agent. This allowed us to confirm infusion success the following day with MRI. With these live and next-day *in vivo* MRI data collected across ten animals and three different brain regions, we were uniquely positioned to develop a model to assist in planning CED procedures in the brains of NHPs. This work is important to the field because not all researchers have access to MRI scanners for next-day imaging, and fewer still are equipped to perform NHP viral infusions in an MRI scanner. We propose a CED modeling method which can assist any researcher in NHP neurosurgical CED planning.

Here we have developed a quantitative bench-side CED model which provides the users hands-on CED experience. Our bench-side model builds off of our recent qualitative infusion modeling work (Ojemann *et al.*, 2020), as well as our *in vivo* NHP data (A Yazdan-Shahmorad *et al.*, 2016; Yazdan-Shahmorad, Tian, *et al.*, 2018). Bench-side CED models are usually comprised of dye infused into agar phantom, a clear gel with material properties similar to the brain (Chen *et al.*, 2004; Pomfret, Miranpuri and Sillay, 2013). In this work we propose a similar model, but to our knowledge we are the first to base a bench-side model on *in vivo* MRI data of CED in NHP brains. We provide the MRI data and we present a calibration method for our model using the MRI data to ensure that reproduction of our quantitative method is practical for the field. Infusions into the primate brain are inherently coupled with surgical and experimental risks, however the toolkit presented here mitigates the risk factors of these procedures, such as cost, surgical time, and overall subject count, by providing easily accessible ways to plan CED experiments. We also utilize a radiolabel that can be co-infused with viruses that can be imaged in MRI 24 hours post-operatively, which empowers researchers without immediate access to an MRI scanner to identify issues and make any necessary surgical corrections in a timely fashion.

5.2 Materials and Methods

5.2.1 Subjects

Data from ten macaques were used for this study as described in Table 1. The cortical and thalamic data (total n = 5) come from previously published procedures (Yazdan-Shahmorad *et al.*, 2013; Azadeh Yazdan-Shahmorad *et al.*, 2016; Yazdan-Shahmorad, Silversmith, *et al.*, 2018; Yazdan-Shahmorad, Tian, *et al.*, 2018; Karam Khateeb, Griggs, *et al.*, 2019), and those data have been used in the present study. In contrast, data from the medial temporal lobe (MTL) group is derived from new injection procedures, which are described in detail below. Ages ranged 5 – 11 years, and weights ranged 5.7 – 17.5 kg. Five females and four males were rhesus macaques (Macaca mulatta) and one male was a pig-tail macaque (Macaca nemestrina). MTL Subjects were provided by the tissue distribution program available from the Washington National Primate Center (WaNPRC), and no observable differences were seen in our data as a function of age, sex, species, or weight.

Table 5.1: NHP and surgical data. NHPs are named for their infusion location(s). Medial temporal lobe and caudate nucleus (MTL). Hippocampus (HPC). Entorhinal cortex (EC), Tail of Caudate Nucleus (C). Reprinted from (Griggs, Garcia, *et al.*, 2022) *with permission.*

NHP Name	**C1**	**C2**	**CT**	**T1**	**T2**	**MTL1**	**MTL2**	**MTL3**	**MTL4**	**MTL5**
Infusion Target	Cortex		Cortex, Thalamus	Thalamus		MTL (HPC+C)		MTL (EC)	MTL (HPC+C)	MTL (HPC)
NHP Variety	Rhesus Macaque									Pigtail Macaque
Sex	M	M	M	F	F	F	F	F	M	M
Age (y)	7	8	8	9	11	8	9	8	8	5
Weight (kg)	16.5	17.5	8.7	7.5	6.5	8.2	6.4	5.7	8.88	7.2
Cannula Step Tip Length (mm)	1		1 (Cortex) and 3 (Thalamus)	3						
Left Hemisphere Infusions (µl)	50, 50, 50, 50	50, 50, 50, 50	50 (Cortex)	140, 120	115, 85	15	20	10, 10	15	N/A
Right Hemisphere Infusions (µl)	-	-	246 (Thalamus)	152, 111	-	15	20	10, 10	15	20
Contrast Agent	Gadoteridol					Manganese				
MRI Timing	Live	Live (2 infusions)	Live			Next-day				
Institution	University of California, San Francisco					University of Washington, Seattle				
NHP Alias	Monkey J *	Monkey G *	NHP-H **, ***	NHP-A **	NHP-B **	N/A				

* (Yazdan *et al.*, 2016), ** (Yazdan *et al.*, 2018), *** (Yazdan *et al.*, 2013)

5.2.2 Animal procedures and MRI analysis

Three different neuroanatomical structures were targeted for CED infusions: cortex, thalamus, and the medial temporal lobe together with the caudate nucleus (MTL). Most of the cortical and thalamic infusions were validated with live MRI, while MTL infusions were validated with MRI the day following infusion. Table 1 contains infusion details for each subject.

Subsequent subsections describe various methods and MRI analysis related to cortical, thalamic, and MTL infusions. Because the procedures relating to the cortical and thalamic groups have been previously published, detailed surgical methods are omitted with references to the respective primary studies. However, aspects of the procedures germane to the present study are presented. For the MTL group, details of the surgical methods, euthanasia, and immunohistochemistry are presented in full. For all procedures, vital signs such as heart rate, respiration, and body temperature were monitored throughout.

5.2.2.1 Cortical infusion

We have previously described the surgical methods for cortical CED procedures (Azadeh Yazdan-Shahmorad *et al.*, 2016; Karam Khateeb, Griggs, *et al.*, 2019). Briefly, subjects were anesthetized under isofluorane, a craniotomy was made above sensorimotor cortex in a sterile operating room, and an MR-compatible cannula guide was affixed to the skull with MR-compatible screws and dental acrylic. Afterwards, the subjects were transferred to an MR scanner (Siemens 3T) while remaining under isoflourane anesthesia. We inserted the tip of a stepped-tip cannula about 2 mm below the surface of the brain in the sensorimotor cortex.

Table 5.2: Virus Information. S1 (Primary Sensorimotor Cortex), M1 (Primary Motor Cortex), AT (Anterior Thalamus), MT (Medial Thalamus), PT (Posterior Thalamus), HPC (Hippocampus), C (Tail of Caudate Nucleus), EC (Entorhinal Cortex). vm/mL (virus molecules per milliliter).). Reprinted from (Griggs, Garcia, *et al.*, 2022) *with permission.*

Animal Name	C1	C2	CT		T1	T2		MTL1		MTL2		MTL3		MTL4		MTL5
Hemisphere	Left	Right	Left	Right	Left	Left	Right	Left	Right	Left	Right	Left	Right	Left	Right	Right
Target	S1+M1		S1	MT	AT+PT			HPC	C		HPC	EC		HPC	C	HPC
Vector Serotype	AAV5		AAV2.9	AAV2.2	AAV2.9			AAVRetrograde						PHP.eB	AAV2	PHP.eB
Vector	AAV-CamKIIa-C1V1-EYFP		AAV-CaMKII-ChR2(H134R)-YFP					AAV-CAG-hChR2-H134R-tdTomato	AAV-Syn-Chronos-GFP	AAV-CAG-hChR2-H134R-tdTomato		AAV-CAG-hChR2-H134R-tdTomato		AAV-3xhI56i(core)-minBG-ChR2(CRC)-EYFP-WPRE3-BGHpA		AAV-mDLX5/6-Chrimson R-tdTomato
Titer (vm/mL)	$2.5x10^{12}$		$5.26x10^{12}$	$1.02x10^{13}$	$5.26x10^{12}$			$7.6x10^{12}$	$9x10^{12}$	$7.6x10^{12}$		$9x10^{12}$		$3.25x10^{13}$	$8.7x10^{12}$	$3.55x10^{12}$

A syringe pump (WPI UMP3, MICRO2T SMARTouch SGE250TLL, Sarasota, FL, USA) was used to co-infuse a mixture of AAV-CamKIIa-C1V1-EYFP (Table 2; 2.5x1012 virus molecules/milliliter (vm/ml); UPenn vector core) and a gadolinium-based contrast agent (Table 2; 2 mM Gd-DTPA, ratio of 250:1, Gadoteridol, Prohance, Bracco Diagnostic Inc., Princeton, NJ, USA) into the brain at a starting rate of 1 µL/min, which

was increased every few minutes up to 5 µL/min. After the majority of the volume had been delivered, the rate was reduced in the same stair-step method to end with a rate of 1 µL/min. After infusion, we left the cannula in place for 10 minutes and then removed the cannula. This infusion process was repeated multiple times. During the infusion process, multiple MRI images were taken to track the progress of the infusions. We used fast (2 minute) flash T1 weighted images (flip angle = 30°, repetition time/echo time = 3.05, matrix size = 128 x 128, slice thickness = 1 mm, 64 slices, Siemens 3T MR scanner). After recovery and optogenetic expression, Monkeys C1, C2, and CT were euthanized for immunohistochemical analysis of optogenetic expression (Yazdan-Shahmorad *et al.*, 2013; Azadeh Yazdan-Shahmorad *et al.*, 2016; Yazdan-Shahmorad, Silversmith, *et al.*, 2018).

5.2.2.2 Thalamus infusion

We previously described the surgical details of the thalamic CED infusions (Yazdan-Shahmorad, Tian, *et al.*, 2018), which are similar to the cortical infusion procedures described above. Briefly, the subjects were anesthetized with isoflurane and craniotomies were made (15 mm diameter). We im-planted cannula guides and secured them with plastic screws and dental acrylic. We al-lowed the subjects to recover for two weeks before performing CED. After recovery, the subjects were anesthetized, placed in a stereotax and transported to an MR-scanner. We used the cannula guides to manually insert a 3-mm stepped-tip cannula (ClearPoint Neuro Inc. (formerly MRI Interventions), Solana Beach, CA, USA) to the targeted regions of the thalamus. We used a syringe pump (WPI UMP3, MICRO2T SMARTouch, SGE250TLL, Sarasota, FL, USA) to co-infuse multiple serotypes of AAV-CamKII-ChR2 (Table 2; Upenn vector core) with gadolinium-based contrast agent (Table 2; 2 mM Gadoteridol, Prohance, Bracco Diagnostic Inc., Princeton, NJ, USA) at rates between 0.5 µl/min and 3 µl/min while simultaneously performing fast (2 minute) flash T1 MR-scans (flip angle = 30°, repetition time/echo time = 3.05, matrix size = 128 x 128, slice thickness = 1 mm, 64 slices, Siemens 3T MR scanner). After all infusions were complete, the subjects were transported back to the surgical suite where the cannula guides were explanted and the incision closed. After recovery and optogenetic expression, Monkeys CT, T1, and T2 were euthanized for immunohistochemical analysis of optogenetic expression (Yazdan-Shahmorad *et al.*, 2013; Yazdan-Shahmorad, Tian, *et al.*, 2018).

5.2.2.3. MTL infusion

To pilot the efficacy of expression in the medial temporal lobe (MTL), five viral vectors were infused into the brains of five subjects. Subjects MTL1-3 were infused with two retro-grade viruses (gifted from Edward Boyden & Karel Svoboda; Addgene viral preps #59170-AAVrg & #29017-AAVrg, respectively) (Mao *et al.*, 2011; Klapoetke *et al.*, 2014). Subjects MTL4&5 were infused with three GABA-selective viruses (Allen Institute for Brain Science & University of Washington, Seattle, WA.). See Table 2 for specific information about vectors and target regions for all animals.

The surgical details of the MTL infusions are described in detail here. Animals were sedated with ketamine. A surgical plane was induced with propofol and maintained with 0.8-1.2% isofluorane, the subjects were then stereotaxed. Analgesia was administered prior to (meloxicam) and during the procedure (fentanyl CRI transitioned to sustained re-lease buprenorphine). Sagittal incisions were made to expose the skull, and burr holes were drilled above our intended target. A 3-mm stepped-tip cannula (ClearPoint Neuro Inc. (formerly MRI Interventions), Solana Beach, CA, USA) was stereotactically lowered with a micro-manipulator arm through the burr hole to the targeted region of the MTL (hippocampus or entorhinal cortex), or the tail of the caudate nucleus. We used a syringe pump (WPI UMP3, MICRO2T SMARTouch, SGE250TLL, Sarasota, FL USA) to co-infuse optogenetic viral vector with manganese-based contrast agent (Mn2+, Millipore Sigma, Bulington, MA.) at rates between 1 µl/min and 5 µl/min. The final concentration of Mn2+ mixed with virus was 6.5mM and was specifically chosen as it is well under the limit for neuronal toxicity and interference with viral efficacy as identified by (Fredericks *et al.*, 2020a). After all infusions were complete, the cannula was removed and the incision closed. In one case (MTL5), this procedure was

performed using the Brainsight veterinary surgical robot (Rogue Research Inc., Montreal, QC, Canada) instead of micromanipulator arms. A final analgesic was administered in the form of a local anesthetic block (bupivacaine). The day following infusion the subjects were again anesthetized and placed in an MR compatible stereotax, and 3-D MPRAGE sequences were taken in a 3T MRI Scanner to localize the manganese signal (Scanner: Phillips GE, Boston, MA., slice thickness: 0.35 × 0.35 × 0.5mm anisotropic & 0.5 isotropic voxels, repetition time/echo time = 2, Flip angle: 9 degrees). After eight weeks, animals were euthanized via intraperitoneal pentobarbitol injection and transcardially perfused with 4% paraformaldehyde-phosphate buffer solution.

Harvested tissue was stored in sucrose and then sliced into 50-µm sections using a freezing microtome. Resulting slices were treated in a sodium borohydride bath (Millipore Sigma, Burlington, MA.) to reduce background fluorescence for 24 hours. Afterward, slices were incubated for 72 hours at 4°C in primary antibodies targeting the respective fluorescent tag of the infused virus (for case MTL-4: rabbit-Anti-GFP 1:1000, Abcam #ab290). This was followed by two-hour incubation in fluorescent secondary antibodies (for case MTL-4: donkey anti-rabbit 568 1:200, Invitrogen Molecular Probes #A10042) and DAPI stain (1:5000, ThermoFisher Scientific #D21490) before mounting and visualization.

5.2.2.4. MRI volume extraction

The following infusion volume extraction procedure was performed on the MRI scans. For cortical and thalamic trials, the MRIs were taken throughout the infusion peri-od. For MTL infusions, the MRIs were taken the day after infusion. We imported each MRI scan into MRI viewing software (Mango, Research Imaging Institute, UTHSCSA, San Antonio, TX, USA) and identified the location of the infusion – due to the contrast agent, this area had a higher contrast than the surrounding tissue. A spherical region of interest (ROI) was created and adjusted as necessary to encompass the infused volume. We shrink-wrapped the ROI in 3D with a threshold value below the intensity of the infusion location but above the intensity of the surrounding tissue. The threshold for the ROI was adjusted until it only contained the infusion volume and the final ROI was saved in the NIFTI file format. Next, we reloaded each ROI as its own image and generated an interpolated surface of the infusion volume. Finally, we measured the volume of the bolus using this interpolated surface in the MRI viewing software. In the case of live imaging during infusions, we mapped infusion trajectories by applying this protocol to successive MRI scans within an infusion trial.

5.2.3. Bench-side modeling

We developed a bench-side CED infusion technique using agar and custom-built cannulas. We also developed an image processing technique and statistical methods to analyze the agar data.

5.2.3.1. Cannula production for agar infusions

We manufactured 1-mm and 3-mm stepped-tip cannulas (Supplemental Figure 1) with polyimide coated fused silica capillary tubing (Polymicro technologies, Phoenix, AZ, USA) for cortical and deep infusions respectively. These cannulas were created by sliding the smaller tubing into the larger tubing until the smaller tubing extended out of the larger tubing by 1 mm or 3 mm. This placement was then secured with cyanoacrylate (Super Glue Corporation, Liquid super glue, Ontario, CA, USA). For both cannulas, the inner tubing had an inner diameter of 320 µm and an outer diameter of 435 µm (part #1068150204) and the outer tubing had an inner diameter of 450 µm and an outer diameter of 673 µm (part #1068150625). The cannulas were the same as, or similar to, the cannulas used for our NHP CED experiments above.

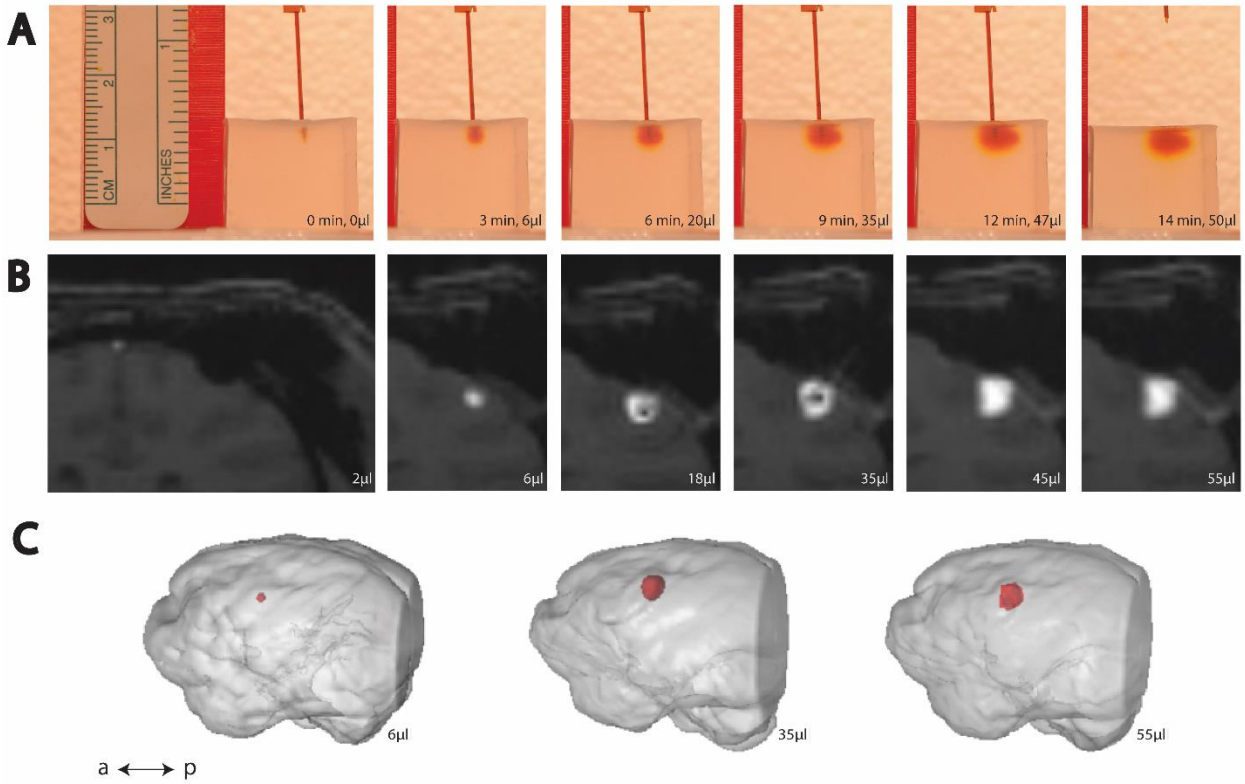

Figure 5.1: Time-lapse (left to right) of cortical CED. (A) Example trial of CED in agar phantom. (B) Example MRI visualization of CED in an NHP. (C) Post hoc reconstruction of NHP brain (grey) and infusion volume (red). Reprinted from (Griggs, Garcia, *et al.*, 2022) *with permission.*

5.2.3.2. Agar phantom infusion

We prepared a solution of 1x phosphate buffered saline (PBS) and 0.6% powder mixture, where the powder mixture was comprised of agar powder (Benchmark Scientific, A1700, Sayreville, NJ, USA) and locust bean gum powder (Modernist Pantry LLC, Eliot, ME, USA) in a 4:1 ratio by mass respectively. We heated and mixed the solution in a microwave to dissolve the powder and poured it into molds to set. Setting occurred in a refrigerator for at least two hours. The molds were 3D printed with polylactic acid (PLA) filament and were designed to produce agar blocks with a 2 × 2 cm base and either 2 or 4 cm high. The agar phantoms were used shortly after setting or were refrigerated for up to one day for future use.

To prepare for CED infusion, we mounted a pump (WPI UMP3, MICRO2T SMAR-Touch, Sarasota, FL, USA) to a stereotactic arm (KOPF, 1460, Tujunga, CA, USA) attached to a stereotactic frame (KOPF, 1430, Tujunga, CA, USA). We filled the pump's 250 mL syringe (WPI, SGE250TLL, Sarasota, FL, USA) with deionized (DI) water and attached it to the pump. The cannula was attached to the syringe with a catheter connector (B. Braun Medical Inc., part #332283, Bethlehem, PA, USA). All of the DI water was ejected from the syringe to fill the cannula with DI water. Undiluted yellow food coloring (McCormick yellow food coloring, Hunt Valley, MD, USA) was then drawn through the cannula and into the syringe. We positioned the agar phantom under the cannula so that it was centered. The agar phantom was oriented such that the side of the block which was not in contact with the mold during the molding process (i.e., the top side, which was the smoothest side of the phantom) was facing up and would be the side to receive the cannula insertion. The cannula was then lowered until the tip touched the surface of the agar phantom. We lowered the cannula manually with the stereotactic arm to a pre-specified depth, 2 mm deep for cortical

infusions and 2 cm deep for thalamic and MTL infusions. We checked that the surface of the agar sealed around the cannula above the stepped-tip before proceeding with the infusion.

To image the infusion process, we positioned a digital single-lens reflex (DSLR) cam-era (Nikon D5300, Minato City, Tokyo, Japan) with a 35-mm lens (Nikon, AF-S NIKKOR 1:1.8G) and adjusted camera settings to clearly image the agar phantom edges, needle, and bolus. The ISO was set at 400, the shutter speed at 1/125, and the aperture at f/6.3. We used interval time shooting. We arranged a white backdrop to help with image processing and placed a ruler near the agar phantom and in-plane with the cannula for scale. We prepared a script in MATLAB (MathWorks Inc., Natick, MA, USA) to run the pump autonomously and in accordance with the infusion rates used in corresponding surgical in-fusions (Table 3). We started the script and the camera's time interval shooting simultaneously. Representative cortical and thalamic infusion models are compared with MRI data as shown in Figures 1 and 2, respectively. Refinements to infusion techniques during preliminary trials included optimizing lighting conditions, and camera angle and placement with respect to the agar phantom.

Table 5.3: Gel infusion rates. Medial temporal lobe (MTL). Reprinted from (Griggs, Garcia, *et al.*, 2022) *with permission.*

Cortical Infusion Rates (µl/min)	**Duration (min)**	**Thalamic Infusion Rates (µl/min)**	**Duration (min)**	**MTL Infusion Rates (µl/min)**	**Duration (min)**
1	1	1	1	1	1
2	1	2	1	2	1
3	1	3	80	3	3
4	1	2	1	2	1
5	6	1	1	1	1
4	1				
3	1				
2	1				
1	1				
Total infused: 50 µl	**Total time: 14 min**	**Total infused: 246 µl**	**Total time: 84 min**	**Total infused: 15 µl**	**Total time: 7 min**

5.2.3.3. Agar phantom image processing

We estimated volumes of distribution from photographs of the agar phantom infusion. A single color component was selected from the color images. (Further description of the color component selection process is found below in section 2.3.4.) Then, we applied a threshold value to the remaining matrix to produce a mask, being a matrix of binary values. (Specific methods for selecting this threshold value are found below in section 2.3.5.) We manually selected the cluster of binary values representative of the infusion bolus and erased the other clusters from the mask. In some cases, this was enough to isolate the bolus, but in other cases the mask appeared to depict the cannula together with the bolus. In these cases, the cannula was erased by masking all pixels above a manually selected point in the image such that the mask outlined the bolus alone. Representative images of the agar phantom image processing are shown in Figure 3. Finally, we converted the mask of the bolus to a volume by assuming an ellipsoidal form, where the ellipsoid was radially symmetric about the axis of the cannula. Similar to (Oh *et al.*, 2007; Prezelski *et al.*, 2021)(Oh *et al.*, 2007; Prezelski *et al.*, 2021), we took the height (*h*) and width (*w*) of the bolus and calculated the volume (*v*) of the associated ellipsoid with the equation

$$v = \left(\frac{\pi}{6}\right) * h * w^2$$

The volume estimation was converted to metric units based on the ruler in the original image.

We performed all agar image processing with MATLAB.

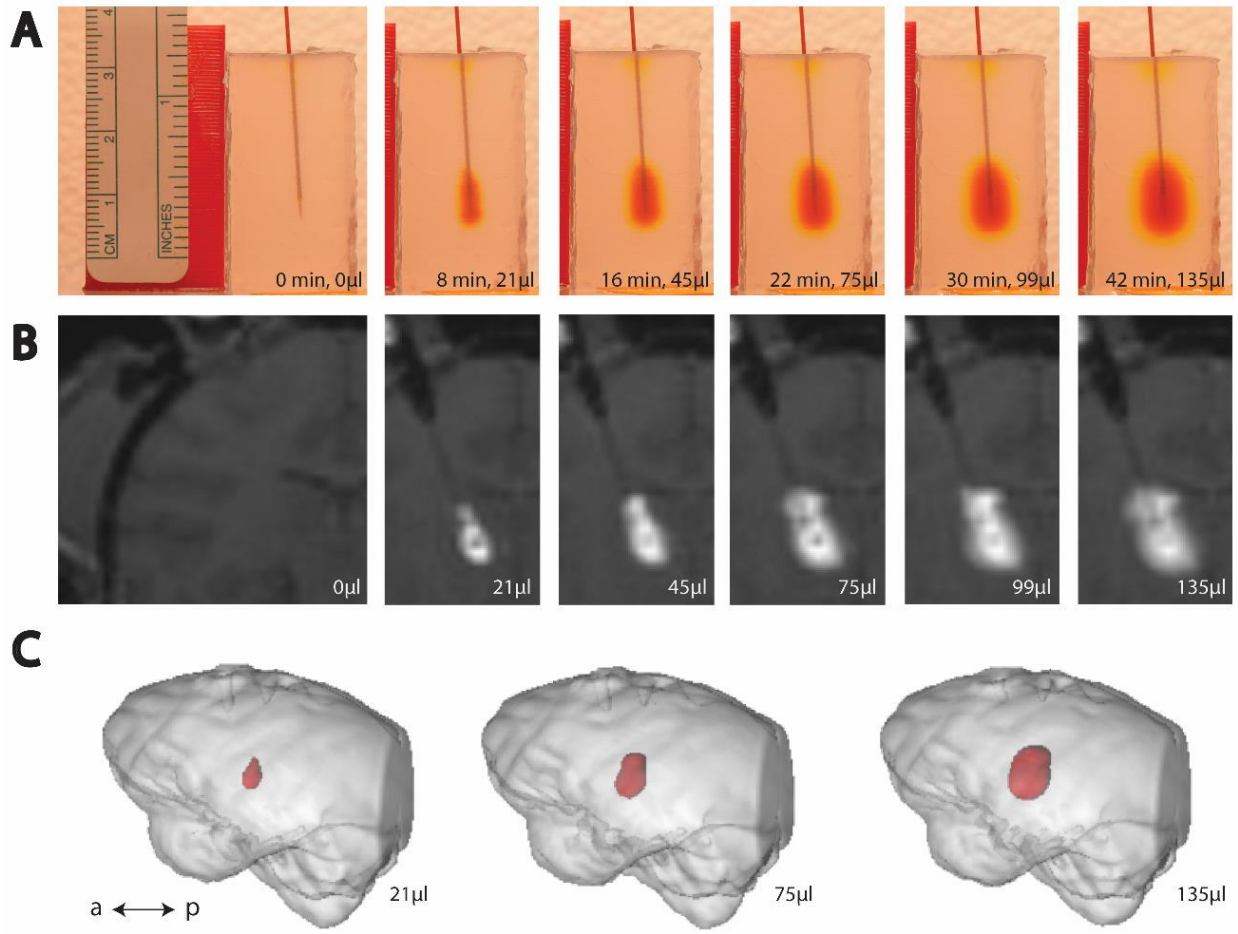

Figure 5.2: Time-lapse (left to right) of thalamic CED. (A) Example trial of CED in agar phantom. (B) Example MRI visualization of CED in an NHP. (C) Post hoc reconstruction of NHP brain (grey) and infusion volume (red). Reprinted from (Griggs, Garcia, *et al.*, 2022) *with permission.*

5.2.3.3. Agar phantom image processing

We estimated volumes of distribution from photographs of the agar phantom infusion. A single color component was selected from the color images. (Further description of the color component selection process is found below in section 2.3.4.) Then, we applied a threshold value to the remaining matrix to produce a mask, being a matrix of binary values. (Specific methods for selecting this threshold value are found below in section 2.3.5.) We manually selected the cluster of binary values representative of the infusion bolus and erased the other clusters from the mask. In some cases, this was enough to isolate the bolus, but in other cases the mask appeared to depict the cannula together with the bolus. In these cases, the cannula was erased by masking all pixels above a manually selected point in the image such that the mask outlined the bolus alone. Representative images of the agar phantom image processing are shown in Figure 3. Finally, we converted the mask of the bolus to a volume by assuming an ellipsoidal form, where the ellipsoid was radially symmetric about the axis of the cannula. Similar to (Oh *et al.*, 2007; Prezelski *et*

al., 2021), we took the height (*h*) and width (*w*) of the bolus and calculated the volume (*v*) of the associated ellipsoid with the equation

$$v = \left(\frac{\pi}{6}\right) * h * w^2$$

The volume estimation was converted to metric units based on the ruler in the original image.

We performed all agar image processing with MATLAB.

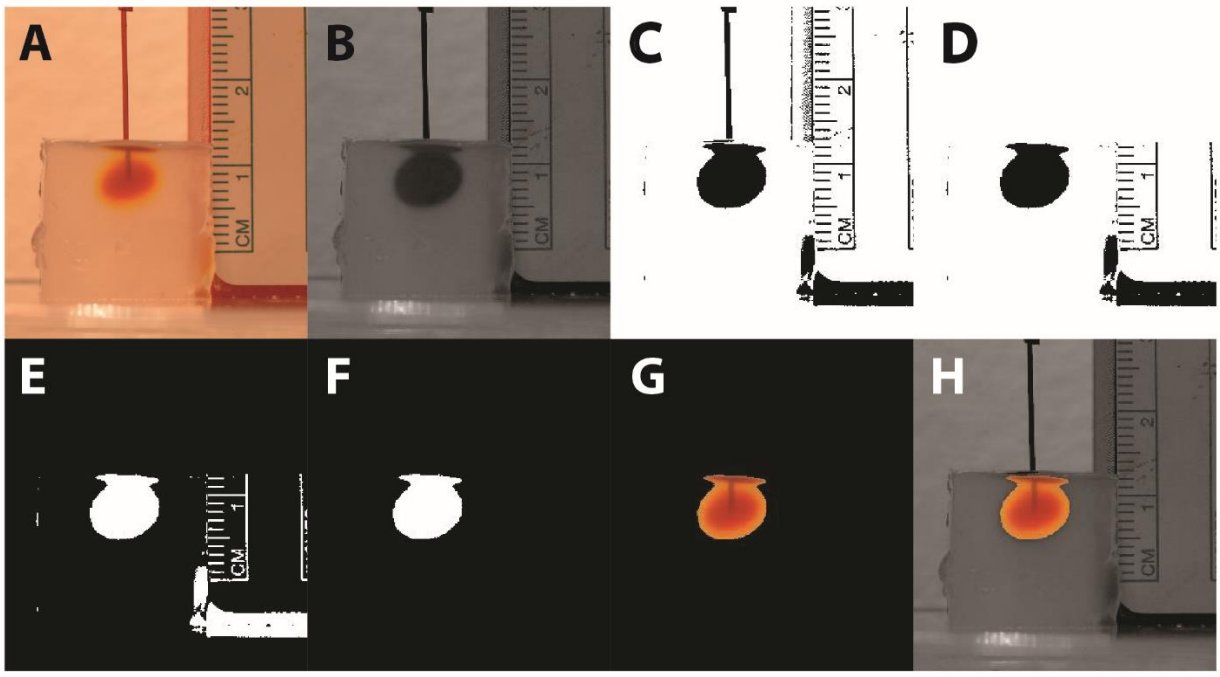

Figure 5.3: Image processing algorithm. (A) Original color image. (B) Single color component image. (C) Thresholded image. (D) Cannula erasure. (E) Binary inversion. (F) Deletion of all non-bolus pixels. This is the final image used for volume calculation. (G) Color image of bolus overlaid on final image for user reference. (H) Color image of bolus overlaid on the single color component image for user reference. Reprinted from (Griggs, Garcia, *et al.*, 2022) *with permission.*

5.2.3.4. Color component selection

Our color component selection is the process by which a 24-bit RGB color image is converted to an image with one 8-bit value per pixel. We tested the three different color components to determine which aligned the agar data most closely with the MRI data. All data of the same infusion type were processed with one selected color component. While image processing software often have functions built-in which will reduce images to a single value per pixel (e.g., the "rgb2gray" function in MATLAB), we found our color component selection process to be more effective.

5.2.3.5. Threshold value selection

After the color component selection, we used a threshold value to distinguish which pixels had strong enough values to be included as part of the bolus. To select the threshold value, we identified a region of the image where heavy coloration faded to no coloration, then we selected a pixel from this region and use its value as the initial threshold. We per-formed the entire image processing procedure with this threshold value and plotted the agar data together with the MRI data to observe the quality of alignment. Based on the results, we selected a new threshold and repeated as necessary in an iterative fashion until

the MRI data and the agar data were in alignment. Once aligned qualitatively, we compared the NHP volume data quantitatively with the agar volume data by using linear regression to determine the slope of each agar and NHP trial, as described in more detail in the next section (2.3.6). All data of the same infusion type were processed with one select-ed threshold value.

5.2.3.6. Statistical methods

To compare the agar and NHP data for the cortical and thalamic trials, we required a quantitative method which would take into account correlations between data points within a given trial, and also compare the different groups of trials. Additionally, we re-quired a method which would not assume a fixed slope between the volume infused by the syringe and the measured bolus volume. To this end, we used a linear mixed effects model with random slopes to fit each infusion trial, both in agar and in NHP data. All best-fit lines were restricted to passing through the origin (i.e., zero input volume and zero output volume). From this model, we calculated the interaction effect which is an ap-proximation of the difference in average slope between the agar and NHP data. All linear mixed effect model calculations were performed with MATLAB's built-in "fitlme" function.

All other statistical calculations were performed in MATLAB except the average and percent error values of Table 4, which were performed in Excel (Microsoft Corp., Redmond, WA, USA).

Table 5.4: Cortical and thalamic data. Reprinted from (Griggs, Garcia, *et al.*, 2022) *with permission.*

Cortical Infusion Slopes			
NHP	**MRI Slopes (µl/µl)**	**Trial**	**Gel Slopes (µl/µl)**
C1	2.86	1	3.03
C1	3.90	2	2.69
C1	3.07	3	2.72
C1	4.61	4	4.74
C2	2.67	5	4.11
C2	3.05	6	4.67
CT	3.07	7	4.23
		8	3.10
		9	4.81
		10	3.82
Thalamic Infusion Slopes			
NHP	**MRI Slopes (µl/µl)**	**Trial**	**Gel Slopes (µl/µl)**
T1	3.48	1	2.63
T2	3.59	2	3.71
T2	3.30	3	4.02
CT	6.38	4	2.66
		5	3.17

5.3. Results

Some agar infusion trials were unsuccessful, and these failed trials were omitted from statistical analyses and reattempted. Failed trials may have been produced by rea-sons such as dye leaking out through the catheter adapter or damaged agar phantoms.

5.3.1. Cortical and thalamic infusions

We iteratively selected color components and threshold values to align the agar data with our previously published cortical (A Yazdan-Shahmorad *et al.*, 2016) and thalamic (Yazdan-Shahmorad, Tian, *et al.*, 2018) NHP data (Figures 4 and 5, respectively). The green component and threshold value of 110 (43% of green component intensity range) were best for the thalamic infusions, and the blue component and threshold value of 67 (26% of blue component intensity range) were best for the cortical infusions.

When comparing the cortical agar data to the thalamic agar data, we observed that the agar and NHP best-fit slopes were similar (Figures 4 and 5). The cortical NHP data had slopes ranging from 2.9 – 4.6 µl/µl, and the cortical agar data had a range of 2.7 – 4.8 µl/µl. Meanwhile, the thalamic NHP data had a range of 3.5 – 6.4 µl/µl and the thalamic agar data had a range of 2.6 – 4.4 µl/µl (Table 4). There is significant variation in the slopes of the best-fit lines of the agar infusion data, however, this variation reflects the variation in the NHP data (Figures 4B, 5B).

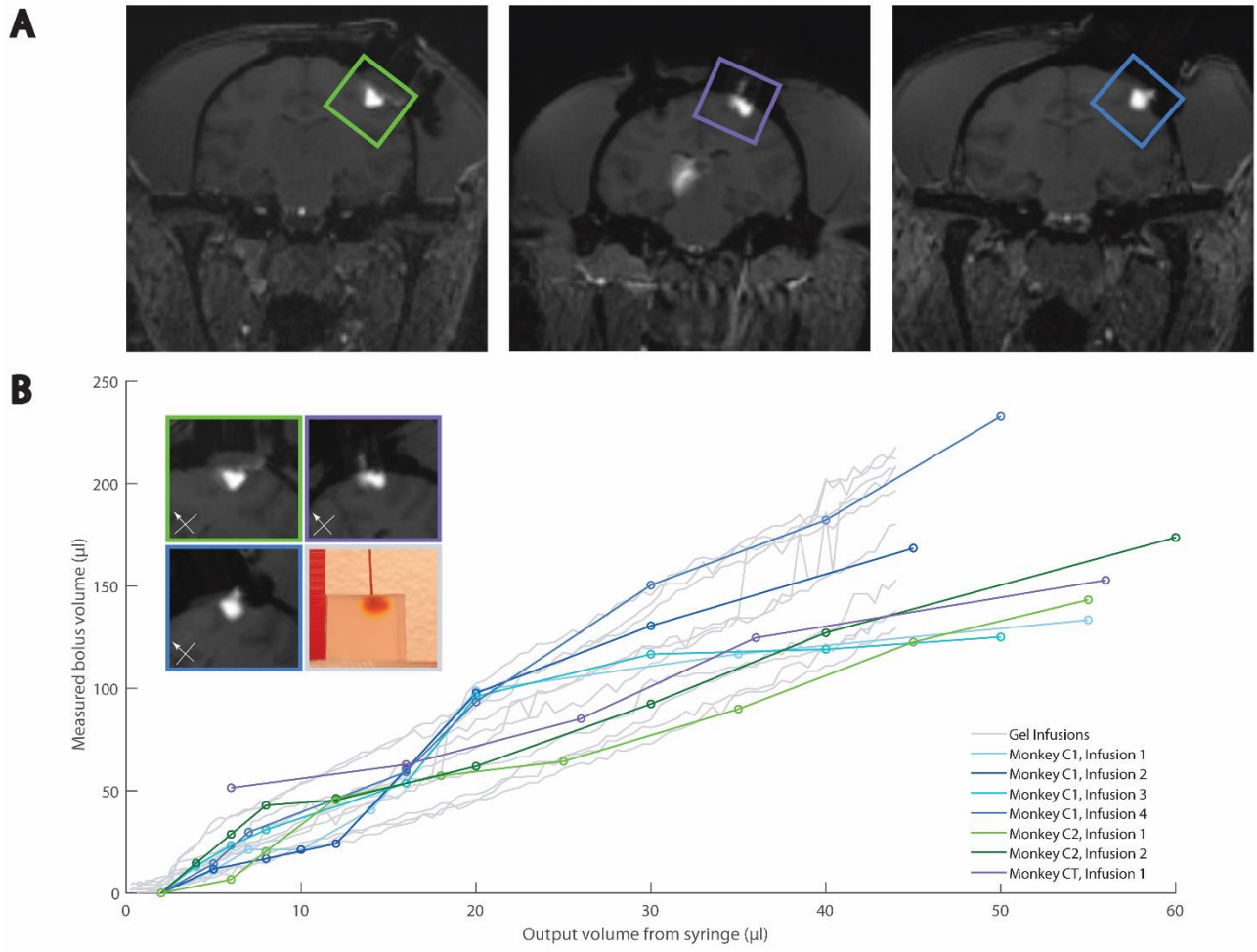

Figure 5.4: Comparison of agar and MRI cortical CED. (A) Example MRIs of cortical infusions. (B) Quantitative and example qualitative (inset) comparisons of agar and NHP data. Box colors in inset relate to images in (A) and traces in (B). MRI data has been previously published (A Yazdan-Shahmorad *et al.*, 2016). *Reprinted from* (Griggs, Garcia, *et al.*, 2022) *with permission.*

We observed that reduction of flow rate at the end of the cortical agar trials led to greater increase in bolus volume with respect to infused volume, i.e., the plots steepen near the end of the infusion protocol (Supplemental Figure 2). This is not characteristic of NHP cortical data, so we omitted the agar cortical

data from 44 µl to 50 µl from statistical analysis and Figure 4 because it was not characteristic of NHP cortical data. Further description may be found in the discussion (section 4.4).

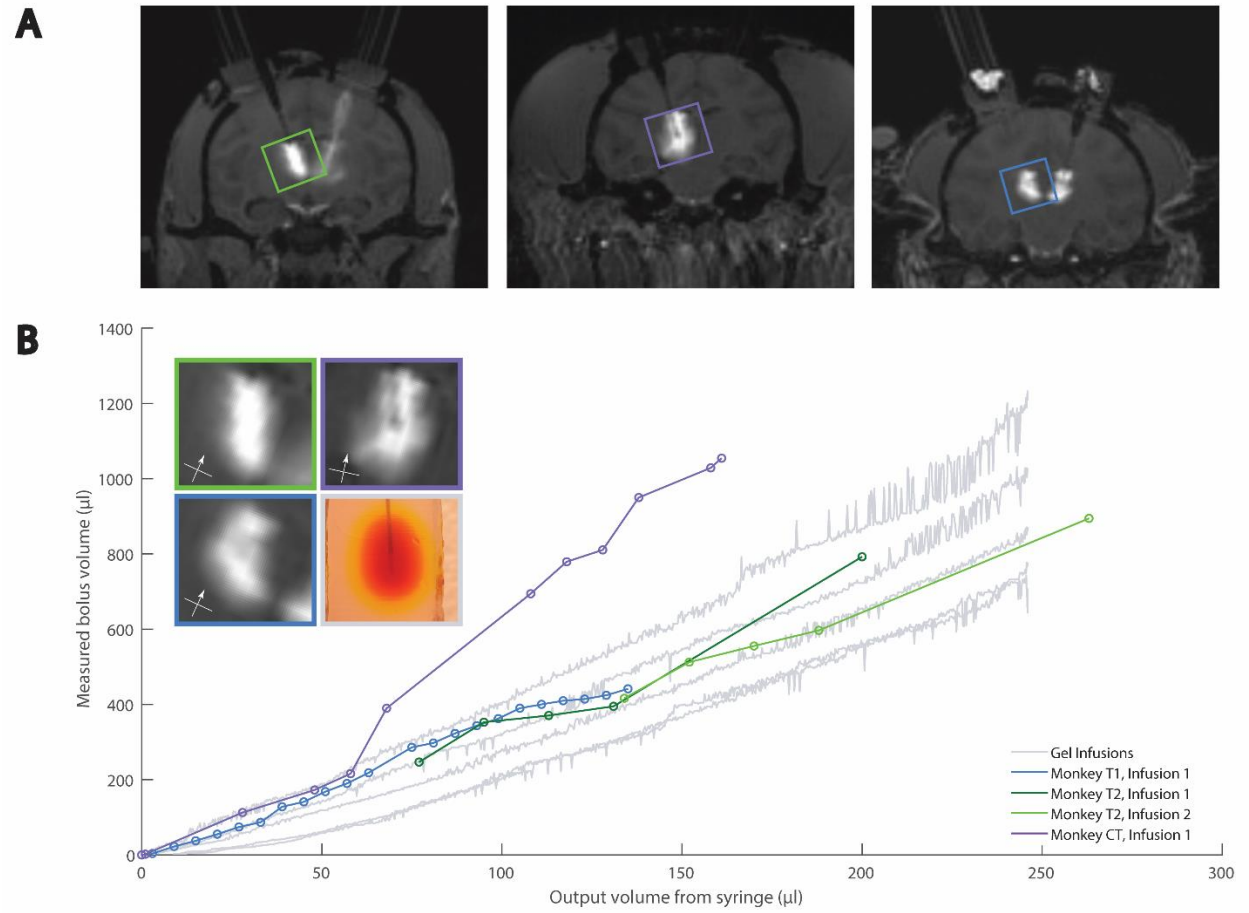

Figure 5.5: Comparison of agar and MRI thalamic CED. (A) Example MRIs of cortical infusions. (B) Quantitative and example qualitative (inset) comparisons of agar and NHP data. Box colors in inset relate to images in (A) and traces in (B). MRI data has been previously published (Yazdan-Shahmorad, Tian, *et al.*, 2018). *Reprinted from* (Griggs, Garcia, *et al.*, 2022) *with permission.*

For the cortical and thalamic trials, we used a linear mixed effects model with random slopes to fit each infusion trial, both in agar and in NHPs. This model produces an interaction effect of 1.1 and -0.5 for cortical and thalamic infusions respectively. These values are close to zero in comparison with the aforementioned ranges of the slopes, and these values have magnitudes less than the slope ranges, indicating that the agar and NHP data differ only mildly and that our agar phantom is a good representation of the NHP data for cortical and thalamic infusions.

5.3.2. MTL infusions

Our MTL NHP data were highly variable, and upon analysis of the MRI scans, we observed that four of the nine infusions displayed a bolus in the MTL as expected (Figure 6A). We only modeled these four successful MTL NHP infusions and omitted the remaining five infusions, which are discussed below (section 3.2.1).

Because the thalamic and MTL NHP infusions used similar cannulas and differed chiefly in the infused volume, we initially compared thalamic agar bolus volumes with MTL NHP bolus volumes (Figure 6B). Counter to our expectations, the MTL NHP data did not align with either the thalamic NHP or agar data.

We recognized that while the cortical and thalamic MRI scans were collected during CED infusion, the MTL MRI scans were collected the next day. Therefore, we reasoned that a CED-generated bolus may diffuse overnight and thus be displayed as a larger bolus in the NHP when MRI is performed the day after infusion. With this in mind, we proposed that diffusion of food coloring in agar after a standard CED protocol would approximate our MTL data. We collected data following the end of 15-µl infusions into agar and observed that the agar data closely modeled the NHP data after approximately 29 minutes of diffusion following the completion of the infusion (Figure 7). We calculated the mean of the NHP infusion volumes and the mean of agar infusion volumes selected from approximately 29 minutes after infusion completion (Table 5), and report a 3.5% percent error between the two data sets. Given the biological context of our model, this error is small enough to safely conclude that 29 minutes of diffusion in our agar phantom, following CED, approximates next-day MRI results of NHP MTL infusions.

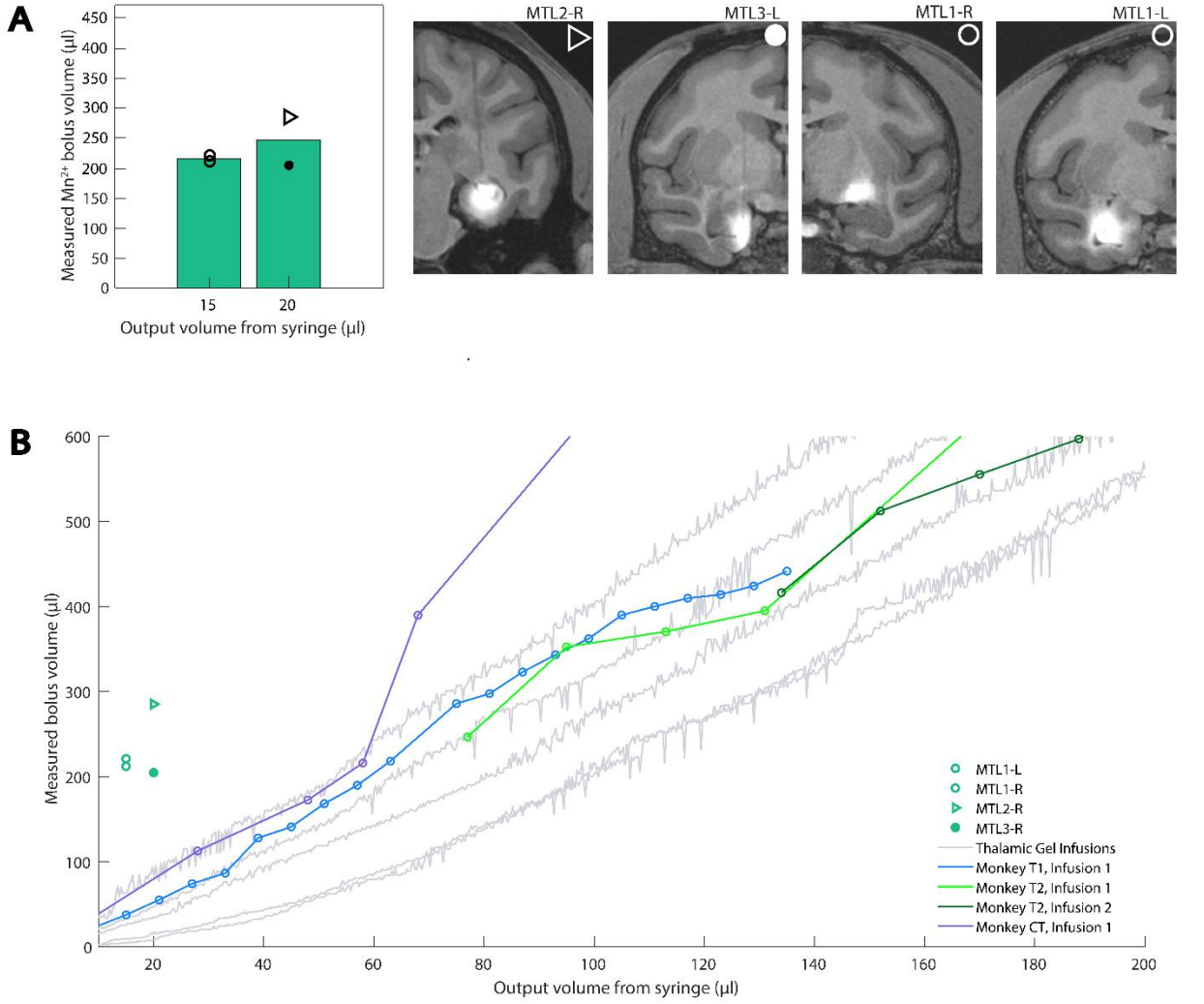

Figure 5.6: MTL MRI data compared with both agar and MRI thalamic data. (A) Deep CED infusions were made into the hippocampus, entorhinal cortex, and the tail of the caudate nucleus. Bar plots show the mean value of measured Mn2+ bolus seen in next-day, post-operative MRIs, with individual data points overlaid. Corresponding MRI slices in the coronal plane are shown for infusions into deep brain areas which are visually similar to cortical and thalamic data. Shape labels correspond to each subject contributing to the data. (B) MTL MRI data compared with both agar and MRI thalamic data. Thalamic MRI data has been previously published (Yazdan-Shahmorad, Tian, *et al.*, 2018). *Reprinted from* (Griggs, Garcia, *et al.*, 2022) *with permission.*

The green component and threshold value of 100 (39% of green component intensity range) were best to model the MTL infusions. We used a t-test to compare the two NHP data points for 15-µl infusions and two data points for 20-µl infusions, and because the two populations were not statistically significant ($p = 0.56$), we pooled the four NHP data points for comparison with agar data. Significant noise was observed in the MTL agar data, more so than in cortical and thalamic agar infusions. The additional noise was possibly due to smaller infusion volumes. We addressed the noise by fitting a line with linear regression to each agar infusion trial and removing data points greater than 1.1 times the corresponding value on the best-fit line.

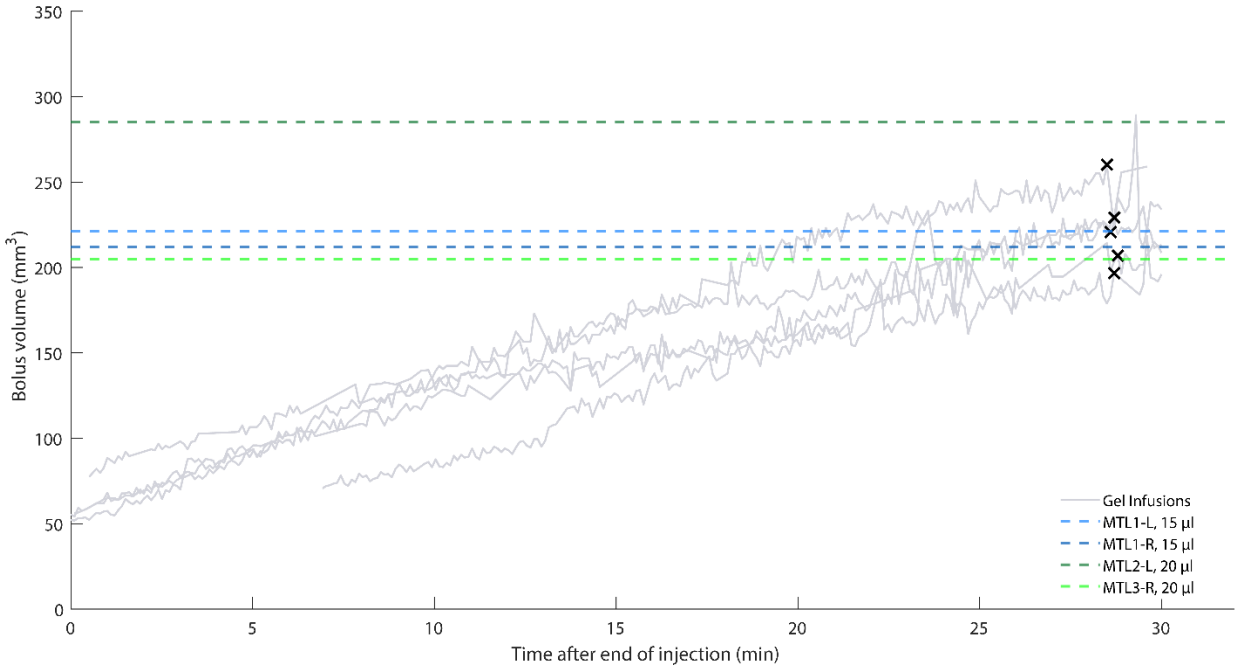

Figure 5.7: MTL MRI data compared with MTL agar data after CED completion. Some trials lack data early in the diffusion process due to the bolus being difficult to identify. Black X's indicate the final point used for statistical analysis from each agar trial. The final chosen points may be shifted slightly to avoid noise spikes. All agar infusions were 15 µl. Reprinted from (Griggs, Garcia, *et al.*, 2022) *with permission.*

Table 5.5: MTL data. Reprinted from (Griggs, Garcia, *et al.*, 2022) *with permission.*

NHP, Hemisphere	Infusion Volume (µl)	Measured Volume (µl)
MTL1, left	15	221.1
MTL1, right	15	212.2
MTL2, left	20	285.3
MTL3, right	20	204.7
Average:		**230.8**
Gel Trial	**Infusion Volume (µl)**	**Measured Volume (µl)**
1	15	196.7
2	15	229.2
3	15	260.2
4	15	220.7
5	15	207.0
Average:		**222.8**
% Error:		**3.5**

5.3.2.1. MTL data omitted from agar modeling

Five of the nine NHP MTL infusions were excluded from the analysis since the next day MRI did not confirm infusion into the MTL regions (Figure 6, Supplemental Figure 3). These failed infusions mostly likely occurred due to the complex shapes of the hippocampus and neighboring structures, which contrasts with the structures of the cortex and thalamus. In three of the five unsuccessful MTL cases, the boluses were very small, which suggested either puncturing into the hippocampal fissure, or infusing deep in the dentate gyrus, depending on the injection depth (Supplemental Figure 3). Penetration of the fissure resulted in contrast agent and virus partially escaping our injection target, indicative of unsuccessful CED. By contrast, deep dentate gyrus infusions were limited to a small portion of the hippocampus, limiting the amount of diffusion observed when compared to our gel model. In the remaining unsuccessful case, the bolus was very large and extended well outside of the volume of the hippocampus, indicating that contrast agent refluxed along the track of the cannula (Supplemental Figure 3). We have excluded these five unsuccessful MTL CED data points from our models, but these negative results are presented to highlight the value of *in vivo* verification of deep injection surgeries.

5.3.3. Histological analysis

For cortical and thalamic infusions, spread of the MR contrast agent modeled the volume of expression of the optogenetic viral vector, as previously analyzed and reported (A Yazdan-Shahmorad *et al.*, 2016; Yazdan-Shahmorad, Tian, *et al.*, 2018). We used different constructs, including retrograde viruses, for our MTL infusions. Because of the variability of the resulting expression, further experiments using a single virus known to express well in these regions is necessary to confirm whether next-day, Mn^{2+} MRI signal mirrors expression. Nevertheless, the Mn^{2+} MRI confirmed our targeting in vivo. Additionally, preliminary evidence from the successful local infection in case MTL4-L suggests a close match between Mn^{2+} signal and immunofluorescence (Figure 8).

5.4. Discussion

Targeted neural manipulations, such as those achieved via optogenetics, are revolutionary techniques for investigating circuit-level communication in the brain and have the potential to influence novel neurotherapeutic technologies in humans. NHPs are the keystone model for validating these techniques because of their similarity to humans, but they are a scarce resource that does not allow for experiments with many unknowns. As such, the risks associated with the viral infusions necessary for most genetic manipulations have led to a lack of uniformity in experimental design and much trepidation in engaging this type of research (Tremblay *et al.*, 2020). In this work, we developed a simple and efficient pipeline to ameliorate a number of these concerns. Our method improves upon past models (Chen *et al.*, 2004; Michal T. Krauze *et al.*, 2005; Pomfret, Miranpuri and Sillay, 2013) by quantitatively matching agar data with *in vivo* infusions of viral particles co-infused with MRI contrast agents, which serve as a proxy of the effective infusion volume. Further, we observe that certain contrast agents can signal the location of infusions up to 24 hours post-infusion, which is a greater time delay for bolus localization than previously demonstrated (Fredericks *et al.*, 2020b). Taken together, the methods presented here serve as an accessible and inexpensive protocol to plan the optimized spread of infusions bench-side and validate the spread and accuracy *in vivo*, significantly reducing the number of unknowns that hinder confidence during circuit-manipulation experiments. Our presented methods contribute to a body of work supporting large-scale optogenetics in NHPs (Yazdan-Shahmorad *et al.*, 2013, 2015; Ledochowitsch *et al.*, 2015; Azadeh Yazdan-Shahmorad *et al.*, 2016; Komatsu *et al.*, 2017; A Yazdan-Shahmorad, Silversmith and Sabes, 2018; Yazdan-Shahmorad, Silversmith, *et al.*, 2018; Yazdan-Shahmorad, Tian, *et al.*, 2018; Stephen L. Macknik *et al.*, 2019; Griggs, Khateeb, Philips, Chan, Ojemann, Yazdan-Shahmorad, *et al.*, 2019; Karam Khateeb, Griggs, *et al.*, 2019; Ojemann *et al.*, 2020; Rajalingham *et al.*, 2021; Griggs *et al.*, 2021a; Griggs, Belloir and Yazdan-Shahmorad, 2021; Belloir *et al.*, 2022; Bloch *et al.*, 2022; Griggs, Bloch, *et al.*, 2022).

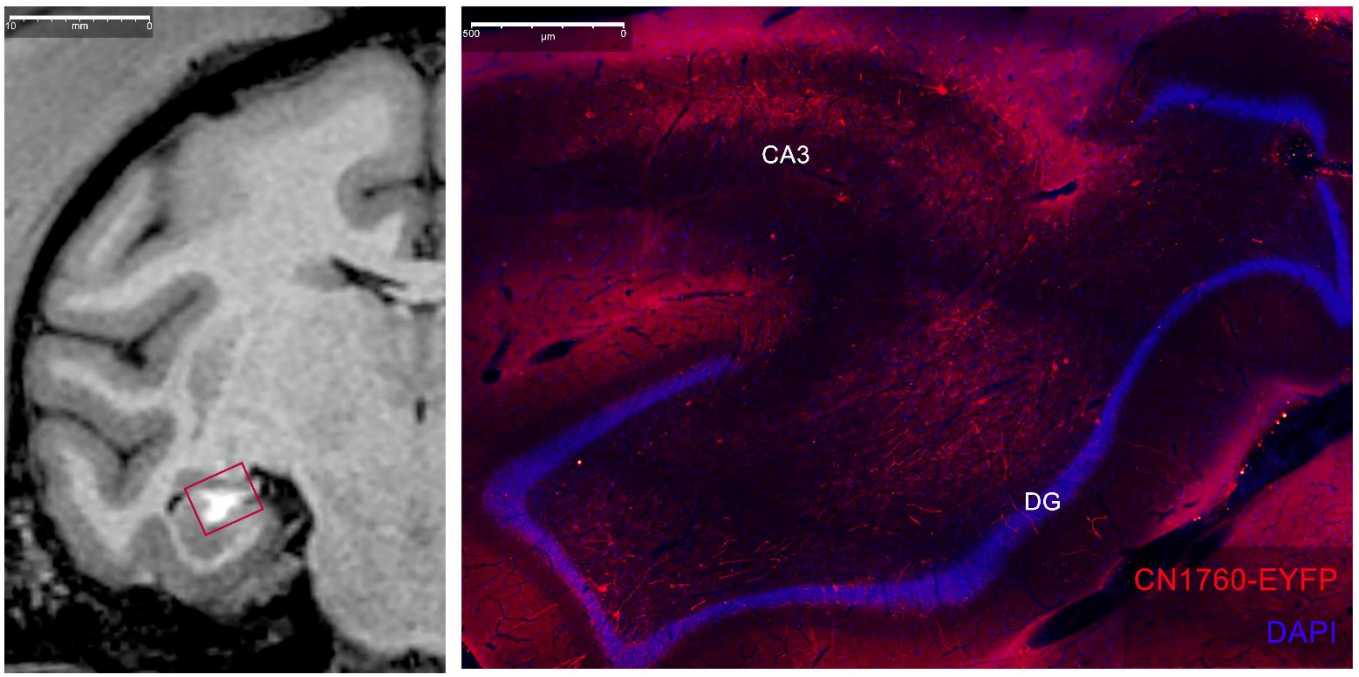

Figure 5.8: Comparison of Mn2+ MRI signal (left) and local expression of virus (right) after a hippocampal injection in case MTL4-L. Right-imaged region highlighted with red square in MRI (left). Our virus used a GABA-specific enhancer to selectively target interneurons, as evidenced by a lack of red pyramidal cell body labeling in CA3 and granule cell body labeling in the dentate gyrus (DG). We tagged infected interneurons and associated fibers with red-shifted fluorophores (anti-EYFP, ThermoFisher, Waltham, MA., USA) and cell bodies were non-selectively labeled using a DAPI stain (ThermoFisher, Waltham, MA., USA). (Viral construct CN1760: trAAV-3xhI56i(core)-minBG-ChR2(CRC)-EYFP-WPRE3-BGHpA (Paul Allen Institute, Seattle, WA., USA).). Reprinted from (Griggs, Garcia, *et al.*, 2022) *with permission.*

Agar has been previously established as a model of intraparenchymal neural tissue and is now commonly used as a medium for simulating infusion procedures (Chen *et al.*, 2004; Michal T. Krauze *et al.*, 2005; Pomfret, Miranpuri and Sillay, 2013). Our work builds on prior studies by presenting a data-driven method developed from *in-vivo* results. To our knowledge, the model proposed here is the first to provide a quantitative method of fitting agar infusion data with NHP CED data collected with live MRI. Because of this, our model serves as a more accurate guide for selecting infusion parameters for future *in vivo* infusions targeting a wide array of brain areas when compared to other simulations.

Our work lends itself well to case-by-case methodological refinements: for example, researchers may consider alternative cannulas, infusion protocols, etc. to cater to their goals. Additionally, our method is designed to facilitate replication by other labs with its simplicity in both materials and methods. We also recognize that labs replicating our work are unlikely to implement agar infusion imaging setups identical to our own. With this in mind, we designed our image processing technique to be easily adaptable to different imaging setups. We provide NHP MRI bolus volume data (see Supplementary Materials) to which other labs may align their own agar infusion data, using our presented method. We have also made our custom code freely available (see Data Availability Statement), and the code is written in MATLAB which is widely used by researchers and is straightforward to adapt for applications akin to ours.

5.4.1. Diversity of Modeled Structures

To maximize flexibility in accurately predicting spread of CED infusions in a variety of brain areas, we used *in-vivo* data from cortical, thalamic, and MTL infusions of viruses co-infused with MRI contrast agent. Our

cortical and thalamic procedures, which represented shallow and deep infusions into large brain structures, utilized live MRI taken during surgery. In addition to qualitative agreement between these infusion types, the ranges of MRI data best-fit slopes were similar (2.9 – 4.6 µl/µl for cortical and 3.5 – 6.4 µl/µl for thalamic) which suggested that the agar models for cortical and thalamic infusions may be similar as well. This proved to be the case: Despite differences in cannula design, depth of insertion, and infusion protocol, the models for both cortical and thalamic CED were generated with our same presented method and aligned well to the *in vivo* data (agar model best-fit slopes were 2.7 – 4.8 µl/µl for cortical and 2.6 – 4.4 µl/µl for thalamic). The cortical and thalamic models did differ in the parameters used during image processing (cortical: blue component, threshold = 67; thalamic: green component, threshold = 110), but this demonstrates that our method is robust to variations in agar infusion processes. Our successful MTL cases differed from the previous two conditions and represented infusions into more limited and more difficult to access deep structures. Additionally, they differed in their post-operative MRIs in that scans were taken ~20 hours after infusion. We found that our initial hypothesis of these data aligning to the thalamic cases was invalidated. However, after accounting for diffusion expected from the delay in imaging, our model successfully aligned to all three conditions.

5.4.2. Insights from MTL Infusions

Because of its unfurled shape in primates compared to rodents (Strange *et al.*, 2014), standard injections into the NHP hippocampus are laborious and often require either multiple craniotomies and penetrations (Zola *et al.*, 2000) or penetrating through the long-axis of the structure and periodically injecting while retracting (Hampton *et al.*, 2004) to try and maximize coverage. To inject into this structure more efficiently, we leveraged the unique ability of CED to deliver a large bolus with a single infusion in our MTL CED group, which to our knowledge is the first set of CED infusions delivered to this area in NHPs. Because of the exploratory nature of these experiments, we experienced challenges that made delivery into this structure and subsequent imaging of our contrast agents more difficult. Infusion MTL2-L was a case of mass reflux due to an error made during the infusion delivery. MTL3-R and MTL4-R represent issues in targeting. Because much of the hippocampus is separated from the rest of the brain by ventricular spaces except laterally, targets made too shallow or too deep will leak into those spaces and either dissipate away or reflux upwards. For similar reasons, posterior-medial injections—for example targeting the intermediate dentate gyrus—produced more isolated boluses (cases MTL4-L, MTL5-R). Our successful cases were qualitatively similar to our cortical and thalamic data because they were delivered to larger, more anterior regions in the genu of the hippocampus, or to large neighboring regions such as the entorhinal cortex or tail of the caudate nucleus. For areas such as MTL where targeting needs to be very precise, we strongly recommend the use of MRI validation of injection either during infusion or the next day.

5.4.3. MRI scan parameters for successful contrast label visualization

Our novel MTL infusions were also the first to utilize co-infused manganese to localize viral infusions in MRI scans acquired ~20 hours post-operatively. Despite the differences in employed contrast agent, scan acquisition timing, and even the scanner used between this group and our cortical and thalamic infusions, we observed a few similar parameters for successful contrast imaging in all MRI scans for all groups. Specifically, all scans were T1-weighted scans with a repetition time/echo time ratio around 2 to 3 and flip angles from 9 to 30 degrees. Analysis of other studies employing similar manganese-enhanced MRI protocols either to image viral injections delivered at shorter delays (Fredericks *et al.*, 2020a) and at much longer delays for *in-vivo* tract tracing (Simmons *et al.*, 2008) also closely mirrored the majority of parameters used in these experiments, suggesting a range of optimized parameters for imaging T1-weighted MRI contrast agents.

5.4.4. Diffusion versus convection using agar

It is important to note that while agar is a good model of CED, agar's rate of diffusion differs from the rate of diffusion in the brain. This factor became apparent when we observed that reduction of flow rate at the end of the cortical agar trials led to greater increase in bolus volume with respect to infused volume, i.e., the plots steepen near the end of the infusion protocol (Supplemental Figure 2). This is consistent with our observation that diffusion will continue to cause the bolus to grow in agar after the end of our infusion trials. With this in mind, we concluded that diffusion and convection both contribute to bolus size in agar to varying degrees during CED. However, we propose the relative contributions of diffusion and convection were skewed when the flow rate was reduced at the end of the protocol, thus allowing diffusion to contribute more heavily to the bolus size in agar. To prevent the best-fit lines of the cortical agar data from being skewed due to this effect, we omitted the data from 44 µl to 50 µl from statistical analysis and Figure 4. This effect was not observed in the thalamic agar infusions likely due to the lower maximum rate of infusion (3 µl for the thalamic agar protocol, as contrasted with 5 µl for the cortical agar protocol) in conjunction with the short duration of infusion at the lower rates and small amount of volume infused during the flow rate reduction at the end of the protocol. This effect was not observed *in vivo* cortical or thalamic injections collected with live MRI. We observed diffusion in our *in vivo* MTL data, but the data were collected with our next-day imaging technique, thus allowing sufficient time for diffusion. We show that MTL next-day imaging data can be modeled with our agar phantom when we allow 29 minutes of diffusion following the end of the infusion protocol. This highlights that the speed of diffusion in agar differs from that of the brain. Also, this is in agreement with our observation that cortical and thalamic NHP data collected with live MRI did not exhibit high levels of diffusion at the end of the protocols, in contrast with cortical agar data.

5.4.5. Technical Considerations

We encountered some issues during agar infusions. The most common issues faced when refining infusion techniques were damaging the agar during its extraction from the mold, such that no smooth surface was available for imaging, and reflux of the dye during the infusion. While agar preparation became more efficient with practice, we suggest that custom, flexible silicone molds be considered in lieu of our 3D printed molds to more easily produce undamaged agar phantoms. Reflux issues can arise in agar, neural tissue, and other media and are less easily mitigated because the cause of reflux is not always obvious. In some cases, reflux may be related to the quality of the seal between the media and cannula, which is difficult to assess visually even in transparent media such as agar. Additionally, we hypothesize in some cases that the cannula gets clogged with the media during insertion. To address this potential issue, we suggest a low flow rate during insertion to avoid clogging.

As previously mentioned, the agar data are aligned to *in vivo* MRI data with an iterative process of parameter selection. The iterative alignment process allows researchers to fine-tune their image processing parameters to overcome potential differences in lighting, camera placement, etc. While our agar image processing techniques are effective, we acknowledge that software refinements may be attained. Our process is currently semi-automated yet we expect it could be more fully automated in future work. Improvement opportunities may also exist in the refinement of our volume estimation formula, and the characterization of the bolus shape.

5.4.6. Ethical Considerations

Despite the limitations presented, our methods will allow for the development of more efficient and effective CED procedures. We can inexpensively plan the expected spread of our infusions with our data-driven model and validate our surgical targeting rapidly without the need to perform infusions in an MRI scanner. Critically, our method is not only quantitative and data-based, but also designed to aid surgical

planning with its visual, hands-on nature. Our bench-side modeling technique serves to increase the likelihood of success in NHP CED experiments, thus refining animal research processes and reducing the number of animals required for experimentation, both of which are key ethical considerations in animal research and included in the 3Rs (Russell and Burch, 1959). Our model was capable of simulating both cortical and deep infusions (limitations discussed above). Because of this, our method provides a generalized surgical preparation technique to all researchers regardless of region of interest, and particularly to research groups which do not have the facilities or resources required to perform live MRI during CED infusions. Our novel next-day MRI data additionally serve to showcase a post hoc infusion confirmation method that improves upon previous work (Fredericks *et al.*, 2020b) to highlight verification of infusion placement ~20-hours post-operatively. This method supplements our proposed modeling technique and is a welcomed alternative to live-MRI, which requires specialized equipment and facilities often unavailable to researchers. In sum, we propose our method as an additional way of applying the principles of replacement, reduction, and refinement (3Rs) to injections in NHPs (Prescott and Poirier, 2021). We recommend NHP CED infusions be modeled in advance of surgery with our proposed method to reduce the number of animals, replace an excess of pilot procedures with artificial simulations, and refine the overall technique to reduce harm. We also suggest the results be confirmed after surgery with MRI if live-MRI is not feasible during infusion. Finally, our work is designed to be highly flexible. While our methods are specifically prepared for NHP experiments involving optogenetic actuators, we expect that our method would also be generally effective for modeling CED of optogenetic sensors, pharmaceutical compounds, and other therapeutic agents in large brains.

5.5 Supplementary Materials

We provide three supplementary figures and a CSV file of the MRI data points.

5.6 Funding

This work was supported by the National Science Foundation Graduate Research Fellowship Program (#1762114, A.D.G.), the National Institutes for Health (NS107609, A.D.G. and E.A.B.; OD010425, all authors; R01 NS119395, D.J.G. and A.Y.; R01 NS116464-01, A.Y.-S.), University of Washington Mary Gates Research Scholarship (W.Y.A., W.K.S.O.), and the Center for Neurotechnology (CNT, a National Science Foundation Engineering Research Center, EEC-1028725, A.G.J., D.J.G).

5.7 Acknowledgments

We would like to thank all of the staff from University of Washington, Seattle, and University of California, San Francisco who provided animal care and surgical support. We thank Sabes lab for use of their previously published data. We thank Spencer Hansen, Serge Aleshin-Guendel, and Tianyu Zhang for their help with statistical analyses. We thank the Viral Technology team at the Allen Institute for Brain science, Ximena Opitz Araya, Shane Gibson, and Greg Horwitz for assistance with virus production. Finally, we thank Toni Haun, Karam Khateeb, and Megan L. Jutras for their technical help.

Author Contributions: Conceptualization, E.A.B. and A.Y.; Methodology, D.J.G., A.D.G., W.Y.A., W.K.S.O., A.G.J., E.A.B., and A.Y.; Software, D.J.G., A.D.G., W.Y.A., and W.K.S.O.; Validation, D.J.G. and A.D.G.; Formal Analysis, D.J.G., W.Y.A., and W.K.S.O., A.Y.; Investigation, D.J.G., A.D.G., W.Y.A., W.K.S.O., A.G.J., E.A.B., and A.Y.-S.; Resources, E.A.B., A.Y., and J.T.T.; Data Curation, D.J.G., A.D.G., W.Y.A., W.K.S.O., A.Y. and A.G.J.; Writing – Original Draft Preparation, D.J.G., A.D.G., W.Y.A., and W.K.S.O.; Writing – Review & Editing, D.J.G., A.D.G., W.Y.A., W.K.S.O., A.G.J., E.A.B., and A.Y.; Visualization, D.J.G., A.D.G., W.Y.A., E.A.B., and A.Y.; Supervision, E.A.B. and A.Y.; Project Administration, E.A.B. and A.Y.; Funding Acquisition, E.A.B. and A.Y.

5.8 Institutional Review Board Statement

All animal care and experiments performed at the University of Washington were approved by the University of Washington's Office of Animal Welfare, the Institutional Animal Care and Use Committee, and the Washington National Primate Research Center (WaNPRC). All animal care and experiments performed at the University of California, San Francisco were performed under the approval of the University of California, San Francisco Institutional Animal Care and Use Committee and were compliant with the Guide for the Care and Use of Laboratory Animals.

5.9 Informed Consent Statement

Not applicable.

5.10 Data Availability Statement

MRI files, agar data, and histological data will be made available upon reasonable request. MATLAB code has been made publicly available:
https://bitbucket.org/yazdanlab/ced_protocol_and_analysis/src/master/

5.11 Conflicts of Interest

The authors declare no conflict of interest.

Chapter 6: Autonomous cage-side system for remote training of non-human primates

This chapter is representative of work which is complete and published. Reprinted with permission. Please cite the final published version of this work:

> **Griggs DJ**, Bloch J, Chavan S, Coubrough KM, Conley W, Morrisroe K, and Yazdan-Shahmorad A. 'Autonomous cage-side system for remote training of non-human primates,' *Journal of Neuroscience Methods*, 348(October 2020), p. 108969. doi: 10.1016/j.jneumeth.2020.108969.

6.0 Abstract

Background: Training non-human primates (NHPs) for translational medical experimentation is an essential yet time consuming process. To increase training efficiency, some training systems have been designed for NHPs to use at their home cages. Several autonomous cage-side tablet-based systems have been proposed, but none of these systems allow for remote monitoring and task modification while also being wireless, low-cost, light weight, and portable.

New method: Here we present ACTS: an Autonomous Cage-side Training System which meets all these criteria. ACTS consists of 1) a touchscreen tablet and a speaker attached to the subject's home cage, 2) an inexpensive reward system made from a slightly modified fish feeder, and 3), a laptop operating the system wirelessly and remotely via a router.

Results: We were able to test the system and wirelessly train two macaques in their home cages. Remote access enabled us to control ACTS from up to 90 m, through up to 3 walls, and through a floor of a building. The device is compatible with different reward pellet sizes and could run about two hours with a ~4 mm pellet size. The animals were able to generalize the task when transferred to a traditional experimental rig. Comparison with existing methods: The low cost and modest skill required to build and implement ACTS lowers the barrier for NHP researchers and caregivers to deploy autonomous, remotely controlled tablet-based cage-side systems.

Conclusion: ACTS can be used for low-cost, wireless cage-side training of NHPs being prepared for translational medical experimentation.

6.1 Introduction

Computer-based systems have been used for decades to train non-human primates (NHPs) and perform experiments (Perdue, Beran and Washburn, 2018). To increase NHP learning speed and reduce the effort and attention required of researchers, some computer-based systems have been designed for NHPs to use at their home cages. Home cage training systems reduce the burden on researchers who would be required to transport subjects to an experimental rig for each training session and closely monitor the subject throughout the session. Cage-side systems not only allow researchers to monitor subjects remotely, but also have the added benefit of allowing researchers to begin training subjects on tasks even before the subjects are trained to be transported to experimental rigs. This is desirable because it has been observed that training NHPs before introduction to research facilities can improve initial performance at the facility (Tulip *et al.*, 2017). Additionally, training in the home cage can reduce stress levels for some subjects (Bonini, 2019).

Here we propose a touchscreen-based training system that is autonomous, wireless, low-cost, light weight, portable, sturdy, designed for remote subject monitoring and task modification, and configurable to different cage varieties. The system is easily integrated with other lab hardware and is implementable

and modifiable by researchers with modest levels of background in hardware and software. We call our system the Autonomous Cage-Side Training System (ACTS). Our user-friendly system is designed to train NHPs in their home cages to perform motor tasks detected by a touchscreen.

Several published touchscreen-based systems meet some but not all of the characteristics fulfilled by ACTS. Touchscreen-based systems have been reported as wireless (Calapai *et al.*, 2017; Butler and Kennerley, 2019), low-cost (Butler and Kennerley, 2019), light weight (Calapai *et al.*, 2017; Butler and Kennerley, 2019), and portable (Truppa *et al.*, 2010; Calapai *et al.*, 2017; Berger *et al.*, 2018; Perdue, Beran and Washburn, 2018; Butler and Kennerley, 2019), but to our knowledge no published system has met each of these requirements while also allowing for remote subject monitoring and task modification.

Our proposed ACTS can be broadly used for NHP training, experimentation, and enrichment. We demonstrate an application of ACTS by training rhesus macaques to perform a touchscreen-based visually-guided motor task.

6.2 Materials and Methods

We designed ACTS to present animal subjects such as NHPs with tasks and corresponding rewards. ACTS operates by sending MATLAB screen data from a laptop to a tablet, which then sends touch information back to the laptop. Based on the inputs provided from the tablet, the laptop wirelessly controls a feeder and speaker via a Wi-Fi transmitter/receiver. A summary schematic is depicted in Figure 1. The cage-side components of ACTS consist of 1) an aluminum structure supporting a tablet and a speaker to present tasks for the subject, 2) a feeder and tubing to provide rewards to the subject, and 3) an electronics box to house the electronic interfaces between the components. The complete cage-side system, which is approximately 5 kg, is attached to the cage. A laptop running MATLAB (2019a; MathWorks, Natick, MA) controls the cage-side components remotely via a wireless router.

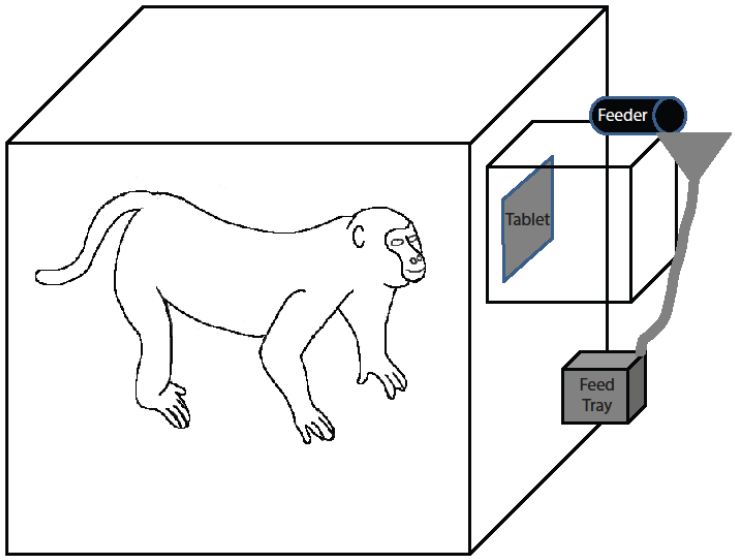

Figure 6.1: System overview. ACTS consists of a structure on which is mounted a tablet, a feeder, and a funnel and tubing to dispense the food rewards into a cage-mounted feed tray. Other electrical components (not shown) necessary to run ACTS are also mounted on the structure. Reprinted from (Griggs *et al.*, 2020) *with permission.*

6.2.1 Subjects

The system was used by two healthy adult male rhesus macaques (Macaca mulatta, weight range 14.5-15.5 kg, age range 6-7 years). The subjects were socially housed. Water was made available *ad libitum* and

no special food restriction or scheduling measures were taken. All animal care and experiments, including the use of ACTS, is approved by the University of Washington's Office of Animal Welfare, the Internal Animal Care and Use Committee, and the Washington National Primate Research Center.

6.2.2 Structure and tablet

We designed the aluminum structure holding the cage-side components (Figure 2A) to be adaptable to different cage designs. For our research purposes we prepared the auxiliary components to fit Seattle-type cages (Figure 2B-D; Lab Products, Seaford, DE). The aluminum structure supporting the cage-side components is a sturdy cuboid constructed with aluminum T-slot bars (80/20 Inc., Columbia City, IN) and measures approximately 25 x 36 x 25 cm (Figure 2C, D). These dimensions allow the aluminum structure to be securely attached to the caging with angled brackets and padlocks such that electrical components and moving parts are held out of reach of our subjects (Figure 2B, D). We designed the aluminum structure to be easily attached to the cage with the angled brackets and padlocks by a single researcher in 1-2 minutes. To allow the subject to touch the screen of the tablet while reducing the chance of the subject tampering with the buttons and plugs on the edges of the tablet, the edges of the aluminum structure and tablet were covered with sturdy, opaque scrap plastic (Figure 2A). We wedged the top and bottom edges of the tablet into the slots in the T-slot bars (Figure 2C, D). This prevents the tablet from being removed from the aluminum structure without a screwdriver, yet extra length of the aluminum bars still allows researchers to slide the tablet left and right ~2 cm along the slots in the aluminum structure to allow easier access to the tablet home button during ACTS setup (Figure 2B). In theory, the subjects can also slide the tablet, so the addition of a set screw was considered to keep the tablet in place. In practice, however, the slots alone provide enough friction that we do not observe the subjects sliding the tablet during use.

6.2.3 Reward System

The reward system consists of a fish feeder with a rotating hopper (HDE, Allentown, PA) and a piping system to guide rewards into the subject's feed tray. To hold the piping system, we constructed a box with acrylic plastic and attached it to the top back corner of the aluminum structure with bolts and wingnuts out of reach of the subjects. The feeder is secured in this box with velcro and propped on scrap acrylic to provide a convenient angle for gravity to aid in reward delivery (Figure 2D). To release rewards, the motor of the feeder rotates the hopper a full turn which briefly positions an opening in the hopper such that food rewards exit the hopper due to gravity. This opening can be manually adjusted in size to accommodate different sizes of food rewards and to vary the average number of food rewards dispensed for each successful trial. The hopper holds up to roughly 120 ml of food rewards. We used glue to connect a funnel and polyvinyl chloride (PVC) tubing together and subsequently used a bolt and wingnut (not shown), a plastic cable tie, and a cable lanyard and padlock to fit the funnel and tubing to the aluminum structure such that rewards are deposited into the cage feed tray (Figure 2C).

6.2.4 Physical arrangement of electrical components

To drive the feeder and the speaker (Adafruit.com, Product ID: 1314; New York, NY), we use a Wi-Fi transmitter/receiver (ESP-01S, ESP8266; STEMedu, Beijing, China) powered by a power supply converter (USB to ESP-01 Adapter, CH240G; STEMedu, Beijing, China). These electronics are housed in an opaque plastic box (Figure 2C). The footprints of the electrical components are small, but the box selected to house the components was relatively large to allow easier maintenance access and to allow room for excess wire length to be bundled. The power switch for the speaker is mounted to the outside of the opaque plastic box for convenient manual access (Figure 2D). The opaque plastic box is mounted in the acrylic box with the feeder and speaker. The speaker is connected to the front of the acrylic box with

plastic cable ties. Holes were drilled into the front of the acrylic box to improve acoustic propagation from the speaker (Figure 2A).

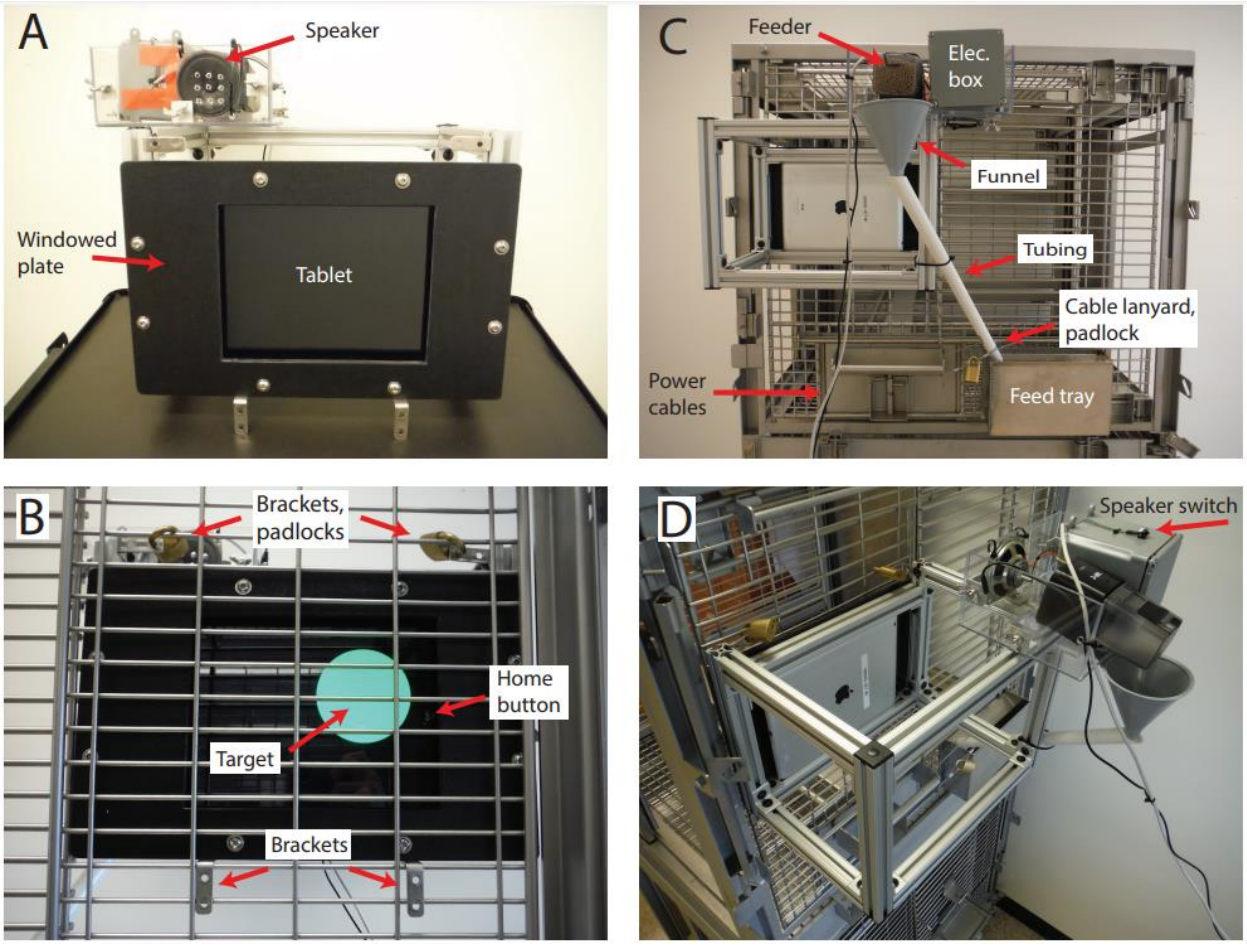

Figure 6.2: Mechanical setup. (A) The structure as viewed from the front. A protective windowed plate was installed to prevent the NHPs from easily pulling on the tablet. Note that the tablet home button is obscured from view. A box was mounted on the back of the structure to contain the feeder, speaker, and electronics. Holes were drilled through the side of the box to improve the acoustics of the speaker. (B) The structure as viewed from within the cage. The two angled brackets above the windowed plate allow the structure to be secured to the bars of the cage with padlocks and the two angled brackets below the windowed plate allow the structure to rest on the bars of the cage. An example target is displayed on the screen. The tablet home button is visible simply to show that researchers may slide the tablet to reveal the button during ACTS setup and then slide the tablet back into place to once again obscure the view of the button. (C) The structure as viewed from the back, mounted on the front of the cage. A funnel and tubing were attached to guide rewards from the feeder to the feed tray. A cable lanyard and padlock serve to restrain movement of the tubing. Power cables for the feeder and other electrical components are routed down the back of the structure. A plastic electrical box provides protection for the electronics which interface between the router, feeder, and speaker. (D) The structure as viewed from an isometric angle. A small speaker switch is secured to the top of the electronics box. Reprinted from (Griggs *et al.*, 2020) *with permission.*

6.2.5 Wireless system and tablet

We operate the cage-side components with a laptop (MacBook Air, Early 2015, 1.6 GHz Intel Core i5, 8 GB 1600 MHz DDR3, Intel HD Graphics 6000 1536 MB, OS X Yosemite version 10.10.5; Apple Inc., Cupertino, CA) which communicates wirelessly with a Wi-Fi router (WRT54GL, Wireless-G 2.4 GHz, 54 Mbps; Linksys, Irvine, CA) on a private network. The router communicates wirelessly with the tablet (iPad, MD510LL/A, version 10.3.3 (14G60); Apple Inc., Cupertino, CA) and with the Wi-Fi transmitter/receiver. A schematic of the system is shown in Figure 3A.

6.2.6 Cage-side electronics

The cage-side electronics include the feeder, speaker (Figure 3A, B), Wi-Fi transmitter/receiver, and power supply converter (Figure 3A, C) required to run ACTS. The Wi-Fi transmitter/receiver is powered from the wall via the power supply converter (Figure 3C). After downloading the Wi-Fi transmitter/receiver driver (Mihalko, 2016) to the laptop, we used the Arduino IDE (Arduino AG, Somerville, MA) to program the Wi-Fi transmitter/receiver to receive commands from the router and then drive the feeder and the speaker via general purpose input/output (IO) pins (Figure 3B, C). Wires were soldered to pins of the button which activated the feeder in order to allow the Wi-Fi transmitter/receiver to drive the feeder directly (Figure 3D). A switch is used to turn the speaker on and off (Figure 3B). Due to a limitation of the Wi-Fi transmitter/receiver, the speaker is required to be turned off during the initial ~20 seconds of power-up when the Wi-Fi transmitter/receiver establishes a wireless connection with the router. The feeder is powered from the wall separately from the power supply converter.

6.2.7 Screen-sharing and data storage

We designed ACTS to run with screen-sharing software (Yam Display, Yamdisplay.com; Yamstu Inc. Seoul, South Korea) which allows the tablet to be treated as an additional screen of the laptop. For best results, we disable the feature allowing the user to zoom in and out with a pinch action, which is called pinch-zoom. We also employ the tablet's "Guided Access" feature to disable the subjects from exiting the screen-sharing app without a passcode. The screen-sharing software did not support audio, thus necessitating a separate speaker. To reduce the likelihood of connectivity issues, the priority levels of the MATLAB and screen-sharing applications are increased in the laptop's operating system. All data generated by the subjects is recorded on the laptop's internal hard drive. Data is saved at the end of each trial to protect against data loss in the case of unexpected laptop failure and to give researchers immediate access to the data.

6.2.8 Tasks

We created three tasks to be displayed on the tablet using MATLAB and the open source Psychophysics Toolbox extensions, version 3 (Brainard, 1997; Pelli, 1997; Kleiner, Brainard and Pelli, 2007). The first is a touch task, which simply requires the subject to touch a start target in order to generate a reward. The second is a delayed reach task requiring the subject to touch the start target and wait for a go tone before touching an end target. The third is a two-forced choice task which requires the subjects to touch the start target, wait for the go tone which plays one of two sounds, and then touch one of two identical end targets as instructed by the go tone. Due to the limited capabilities of the screen-sharing software, this system is not designed for multi-touch use.

6.2.9 System security

The main security risk of ACTS is unauthorized control of the tablet's cameras. To address this risk, two key cautionary measures have been taken. Firstly, ACTS is designed to be run entirely on a private network which would hinder nefarious activity. Secondly, the user-facing camera of the tablet is physically obscured by the windowed plate and the rear-facing camera is physically obscured with a piece of tape.

6.3 Results

We tested different aspects of ACTS to ensure its utility for NHP training, experimentation, and enrichment. We also recorded the cost of components to highlight the low financial barrier of ACTS implementation.

6.3.1 NHP training and data collection

We trained two adult male rhesus macaques, Monkey H and Monkey L, on the touch task using ACTS. Subjects were housed independently while using ACTS. The router and laptop were located in a different

room two walls away from the subjects, which amounted to approximately 6 meters distance. Because aspects of our lab's research ultimately must be performed in a traditional experimental rig, the subjects were introduced to the same touch task in our experimental rig after learning the task on ACTS. When transitioned to the rig, the subjects readily began attempting the task.

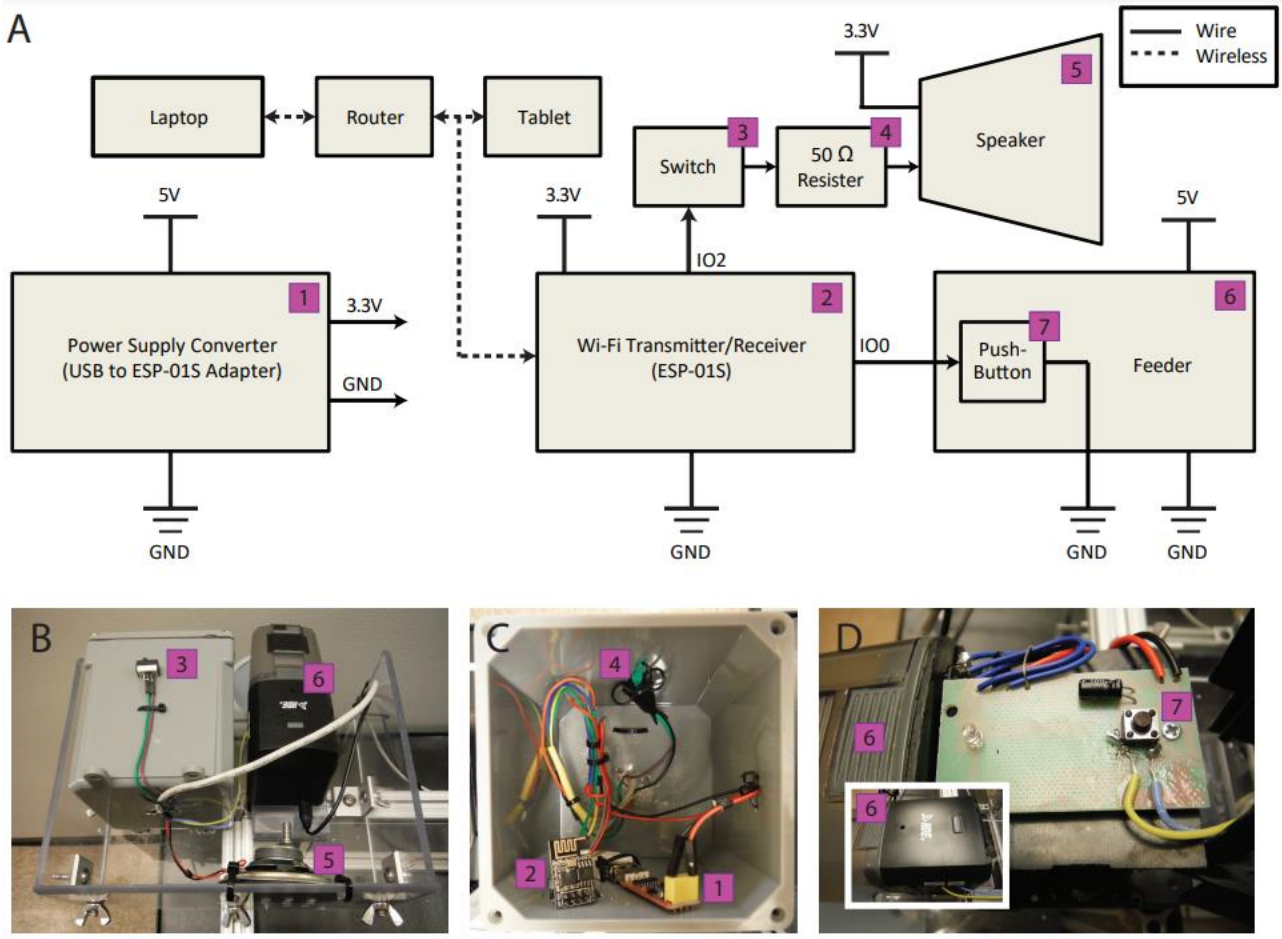

Figure 6.3: Electrical schematic. (A) The entire ACTS system is driven by custom MATLAB code running on a laptop. The laptop communicates via Wi-Fi through a router to both the tablet and the Wi-Fi transmitter/receiver (ESP-01S). The Wi-Fi transmitter/receiver is powered by a power supply converter (USB to ESP-01S Adapter) which is plugged into a standard wall power outlet via a USB cable and wall adapter. The IO2 port of the Wi-Fi transmitter/receiver is wired to the speaker via a switch and a 50 Ω resister. The switch is necessary to disconnect the Wi-Fi transmitter/receiver from the speaker during startup and the resister is necessary to improve impedance matching. The speaker is powered by the power supply converter. The IO0 port of the Wi-Fi transmitter/receiver is wired directly to the pushbutton of the feeder. The feeder is plugged into a standard wall power outlet via a USB cable and wall adapter. (B) A box mounted on the back of the structure contains the feeder, speaker, and electrical box, on which is affixed the speaker switch. (C) The power supply convertor, Wi-Fi transmitter/receiver, and resister are all stationed inside the electrical box with plastic cable ties. Wires were given enough length to allow the electronics to be manipulated by hand outside of the electrical box as needed. (D) The feeder shown with its casing both removed and intact (inset picture). Wires were soldered to pins of the pushbutton to allow for wireless operation: The yellow wire delivers the signal from the Wi-Fi transmitter/receiver and the blue wire is tied to ground. The jackets of the wires were glued to the electrical board of the feeder to reduce risk of mechanical stress on the solder points. The wires were routed out of holes drilled in the casing of the feeder to allow integration with the other electronics. Reprinted from (Griggs *et al.*, 2020) *with permission.*

ACTS saved data from individual trials for analysis (Figure 4A). We performed analysis across multiple sessions to monitor success rates (Figure 4B) and to analyze relationships between other variables.

Parameters were changed session to session, and sometimes within sessions, and the results presented are a simplified summary.

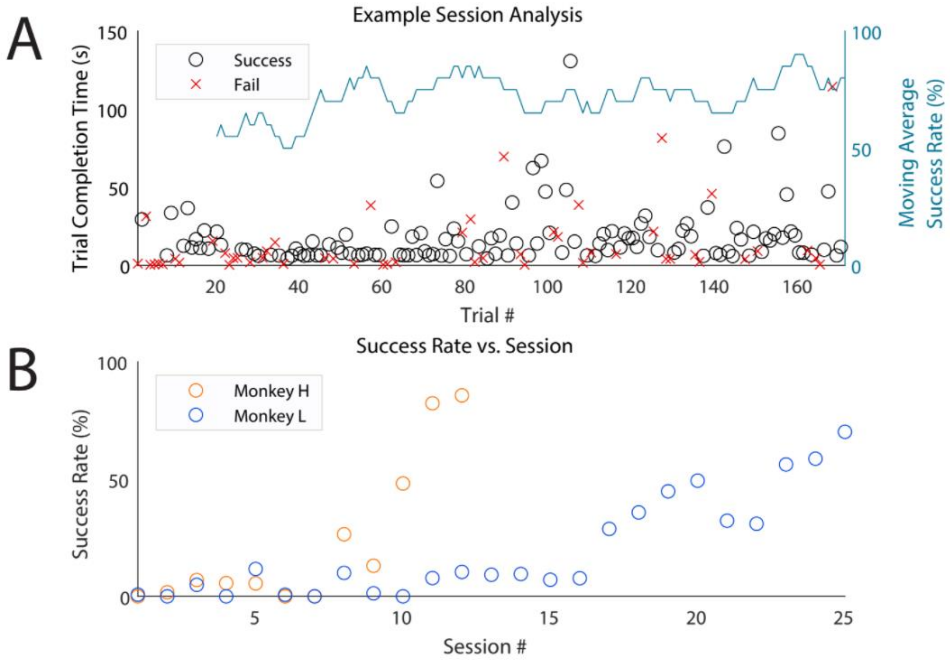

Figure 6.4: NHP usage results. (A) Results from an example touch task session are displayed. Time taken to complete each successful and failed trial are shown, as well as a 20 trial moving average success rate. (B) Two monkeys were trained with ACTS to perform the touch task and their success rate for each session is plotted chronologically. Sessions with ten trials or fewer were excluded from the plot. Reprinted from (Griggs *et al.*, 2020) *with permission.*

6.3.2 Food rewards

Before introducing ACTS to the subjects, a variety of food rewards were tested with the feeder, funnel, and tubing. We found that, in general, round, hard, low-friction food rewards were most compatible with the system. We also found that food rewards which get sticky with prolonged exposure to warm and humid environments should be avoided to prevent the system from jamming. Additionally, small food rewards naturally increased the number of trials that could be run before the hopper of the feeder required refilling. We selected Wilton Jumbo Nonpareils as the initial food rewards for both subjects because they had characteristics desirable for use with the system and they were relatively inexpensive. We observed that Monkey L responded to these rewards but Monkey H was relatively uninterested, so we switched to 45 mg chocolate flavored nutritional rat pellets (commonly used by rat laboratories) or a combination of the two rewards for Monkey H. This appeared to increase motivation while being compatible with the system. Both pellet types were roughly spherical and measured approximately 4 mm in diameter. Some of the feed trays had drainage holes big enough that the rewards would fall through the bottom of the tray, so we swapped these trays out for a tray with smaller drainage holes as needed.

The adjustable opening of the hopper was positioned to allow an approximate average of 5 pellets to be dispensed for each rotation of the feeder. This configuration could allow for an estimated 400 successful trials without refilling the hopper, although we usually ran shorter sessions. Trial completion times and success rates were variable, but an estimate of 10-20 seconds on average per trial at a 100% success rate suggested that a full hopper could provide about 2 hours of training.

6.3.3 Wireless distance

ACTS relied on a private Wi-Fi network broadcast by a Wi-Fi router to communicate wirelessly between the laptop, the tablet, and the electronics that control the feeder and speaker. While effective wireless distance may vary for different groups based on facility layouts and other factors, we tested our system to provide example data. In a hallway without obstructions we demonstrated that cage-side components could operate up to approximately 90 meters away from the router. We also demonstrated that up to three walls can separate the cage-side components and the router, totaling approximately 6 meters, and we demonstrated that cage-side components and the router can be separated by a floor of a building.

6.3.4 Cost

Throughout this work, efforts were taken to limit the cost of ACTS which is detailed in Table 1. In many cases we used equipment and programs already available in our lab and which are likely available in other labs. When we did not have readily available components we used low-cost selections.

Table 6.1: Cost of parts, supplies, and programs used in ACTS in USD. Costs of parts that were available in our laboratory are estimated and indicated with a ''. Downloaded programs that were free at the time of download are indicated with a '**'. The MATLAB license was purchased through a university-wide arrangement with MathWorks and may not be representative of the price advertised to groups affiliated with other institutions. Reprinted from* (Griggs *et al.*, 2020) *with permission.*

Item	Cost
Laptop	$ 500 *
Structural components	$ 166
MATLAB license	$ 135 *
Tablet	$ 100 *
Wi-Fi router	$ 53 *
Feeder	$ 22
Wiring	$ 10 *
ESP-01S and USB adapter	$ 8
Lab tape	$ 6 *
Cable ties	$ 5 *
Electrical switch	$ 4 *
Solder	$ 4 *
Super glue	$ 3 *
Funnel	$ 2 *
Speaker	$ 2
Tubing	$ 2 *
Electrical box	$ 1 *
Arduino IDE	$ 0 **
CH240 G driver (for ESP-01 to USB Adapter)	$ 0 **
Psychophysics Toolbox 3	$ 0 **
Yam Display	$ 0 **
Estimated total	**$ 1023**

6.4 Discussion

Here we present ACTS: an autonomous, wirelessly monitorable and configurable, light weight, sturdy, low-cost training and reward system adaptable to different cage varieties. ACTS is easily integrated with other lab hardware and designed for researchers with modest levels of background in hardware and software to implement and modify for the purpose of NHP training, experimentation, and enrichment. In addition, as ACTS is a video-based system, it may garner more engagement as a source of enrichment than foraging devices (Bennett *et al.*, 2016). ACTS has been used by two adult rhesus macaques. It is wireless which allows researchers to remotely monitor the performance of the subject and modify the parameters (e.g., target size) of the task presented to the subject throughout a session, or even change tasks entirely. Consequentially, our system offers greater flexibility than the comparable, tablet-based Mymou system (Butler and Kennerley, 2019). Although session durations are variable and maximum session times largely depend on success rate, reward size, and quantity of rewards dispensed per success, we estimate that ACTS can offer 2 hours of continuous use in its current configuration. Importantly, ACTS can be used by any species which can interact with a touch screen, and the rewards used can be small enough to be appropriate even for rat-sized animals.

ACTS is designed to allow subjects to "work from home", allowing the animals to learn a new task in the least stressful environment. Standard enrichment practices of the Washington National Primate Research Center had already familiarized the subjects with tablet-based enrichment and with target training to a handheld target. The subjects readily transitioned to learning a touch task in context with the full cage-side system (Figure 2C). The remote task monitoring and configuration capabilities offered by ACTS allowed for rapid skills acquisition, however, cage-side performance is insufficient for our final goals. Because we require our subjects to ultimately perform tasks in an experimental rig, the cage-side tasks are designed to be easily generalized to the rig. With this need in mind, our design allows tasks to be introduced in a familiar environment before they are presented in the less familiar experimental rig.

While our subjects were housed independently during use of ACTS, ACTS could feasibly be modified to support data collection in social housing situations by tagging animals with RFIDs or other related technologies (Andrews and Rosenblum, 1994; Fagot and Paleressompoulle, 2009; Fagot and Bonté, 2010; Gazes *et al.*, 2013; Tulip *et al.*, 2017), or by video identification (Calapai *et al.*, 2017; Butler and Kennerley, 2019). Relatedly, duplicate ACTS systems could be used in the same animal room to train multiple animals at the same time, and the tones produced by the speakers could be altered for uniqueness if needed. In addition to training and experimentation, ACTS is also designed to be used for enrichment, much like other computer-based systems for NHPs (Washburn and Rumbaugh, 1992; Perdue, Beran and Washburn, 2018).

Except for two USB power cables, both of which could easily be replaced with portable power supplies if desired, ACTS is completely wireless. The wireless communications run on Wi-Fi and have been shown to be efficacious through walls, through a floor of a building, and over considerable unobstructed distances. Moreover, because ACTS can be run on a private network as we have shown, the cage-side components and the controlling laptop could theoretically be separated geographically and still be effective with a strong and secure network connection. We tested Bluetooth wireless technology during development but later switched to Wi-Fi to increase effective wireless distance.

Because the system is operated by a laptop, no data is saved to the tablet itself. Instead, data is saved to the laptop after the completion of each trial. This protects against data loss due to unexpected tablet failure which is an advantage over the Mymou system (Butler and Kennerley, 2019). Furthermore, minor coding changes can also allow the data to be saved to a backup external hard drive or a remote server, although we did not test these options.

ACTS is relatively inexpensive. The cost of ACTS, excluding the MATLAB license and laptop, is roughly that of a single laboratory standard commercial feeder. This is a reasonable comparison because both these items are plausibly readily available in laboratory settings and can be utilized for additional projects beyond those targeted by ACTS. To the authors' knowledge, the only other touchscreen-based system to have been published with details regarding cost of implementation is the recently published Android tablet-based Mymou system (Butler and Kennerley, 2019) which was comparable in cost to ACTS although the Mymou system publication did not include the cost of its reward-delivery systems. Here we present our reward-delivery method, a fish feeder with minor modifications, which is considerably less expensive than standard laboratory feeder systems and simpler to implement than an open source feeder (Oh, Hofer and Fitch, 2017).

There are alternatives to the more expensive components of ACTS. For example, free programming languages such as Python could be employed in ACTS. Additionally, the Apple-oriented collection of laptop (MacBook Air), tablet (iPad), and screen-sharing software (Yam Display) could be replaced by products from other brands. This could allow for utilization of equipment that is already available in some laboratory settings without heavily modifying our presented aluminum structure, cage-side components, and MATLAB software. Another possible cost-saving modification to ACTS would be to program and download an app directly to the tablet as this could reduce or eliminate the need for a wireless connection during use. However, since such a system could not be remotely controlled, this modification could limit the researchers' ability to remotely monitor the performance of the subject and change tasks or task parameters throughout sessions, which is one of the strengths of our system and differentiates our system from the Mymou system (Butler and Kennerley, 2019).

ACTS is designed to be relatively easy to build and implement by other research groups. To provide qualitative evidence, ACTS was built with tools and skills native to our laboratory except for cutting the aluminum and plastic parts of the structure and modifying a feed tray to have smaller drainage holes. The light weight and manageable size of the aluminum structure and cage-side components made the system easily portable, yet the design is sturdy enough to endure use by NHPs. Furthermore, the design is easily adaptable to different varieties of cages.

ACTS is also designed to be easily modified for differing needs of NHP researchers and caregivers. For example, while touchscreen-based activities similar to ACTS are commonly used for NHP work (Weed *et al.*, 1999; Fagot and Paleressompoulle, 2009; Fagot and Bonté, 2010; Mandell and Sackett, 2010; Truppa *et al.*, 2010; Gazes *et al.*, 2013; Calapai *et al.*, 2017; Berger *et al.*, 2018; Butler and Kennerley, 2019), other equipment such as joysticks (Richardson *et al.*, 1990; Washburn and Rumbaugh, 1992; Andrews and Rosenblum, 1994; Perdue, Beran and Washburn, 2018), buttons (Tulip *et al.*, 2017), lights, and other electronic or mechanical parts could be integrated into the system. Furthermore, ACTS could be used in conjunction with systems designed to monitor bodily movements of NHPs (Libey and Fetz, 2017; Bonini, 2019). To these ends, the firmware of the Wi-Fi transmitter/receiver (ESP-01S) is easily configurable with Arduino IDE software which is free, widely used in research settings, and has a wealth of online support which is often tailored for users with limited backgrounds in hardware and software. This allows for ACTS to be easily modified to operate other lab equipment such as liquid-based reward systems, lights, robotics, etc. Our chosen Wi-Fi transmitter/receiver only supports two general purpose IO 3.3V transistor-transistor logic (TTL) pins, but other ESP8266-based hardware is available for purchase with more general purpose IO pins. These pins can allow more lab equipment to be integrated with the system. Notably, the increases in cost and size of these ESP8266-based alternatives are generally trivial.

ACTS is designed to complement the growing field of tetherless neurophysiology systems and other tetherless biomedical systems. While tethered neurophysiology research with NHPs is still common and

is presently used in our lab (A Yazdan-Shahmorad *et al.*, 2016; Yazdan-Shahmorad, Silversmith, *et al.*, 2018; Griggs, Khateeb, Philips, Chan, Ojemann, Yazdan-Shahmorad, *et al.*, 2019), some groups have begun developing and using tetherless systems (Jackson *et al.*, 2006; Jackson, Mavoori and Fetz, 2006, 2007; Miranda *et al.*, 2010; Zanos *et al.*, 2011; Borton *et al.*, 2013; Yin *et al.*, 2014; Schwarz *et al.*, 2014; Fernandez-Leon *et al.*, 2015; Su *et al.*, 2016; Libey and Fetz, 2017; Shahidi *et al.*, 2019; Berger, Agha and Gail, 2020; Milton, Shahidi and Dragoi, 2020). The modifiability of ACTS makes it a prime candidate to augment tetherless experiments with tablet-based tasks. Experiments such as these will support research of restraint-free behaviors and corresponding physiology.

Tasks were kept as consistent as possible between the cage-side and experimental rig systems by deriving the MATLAB code for ACTS from the MATLAB code for the experimental rig. Once the subjects learned a task with ACTS, they transitioned readily to working on that task in our experimental rig. Because the animals were able to generalize behaviors so effectively, we plan to train them and any future subjects on additional tasks cage-side using ACTS with the goal of transitioning the behaviors to the experimental rig.

6.4.1 Limitations

We capitalized on freely available software where applicable, and we kept our custom written software simple and easy to modify. These advantages bring about some limitations. Because ACTS relies on screen-sharing software, competition for the cursor can arise if the subject touches the tablet and the researcher attempts to operate the laptop simultaneously. In practice, this means that it is ideal for the researcher to pause the MATLAB program and modify tasks after the subject has completed a successful trial and is busy collecting rewards. Future software development efforts could potentially allow for the subject and researcher to operate ACTS simultaneously. Also, we determined that automatic parameter adjustment features were not necessary because our system can be remotely controlled. However, our MATLAB-based system is easy to modify and the functionality could be added in the future as others have done (Berger *et al.*, 2018; Butler and Kennerley, 2019).

The style of feeder used presents another potential limitation which is its lack of consistency in reward quantity. We chose to sacrifice reward quantity precision in order to select a low-cost feeder. Additionally, we were not concerned with a variance in reward quantity due to literature which suggests variations in rewards can increase motivation (Ferster and Skinner, 1957). An additional limitation of the feeder is the lag in reward delivery. Because the feeder uses a rotation-style hopper, it takes a few seconds for the rewards to be released from the feeder into the funnel, tubing, and ultimately the feed tray. However, the feeder is audible when activated and we have also paired the rotation of the feeder with a reward tone from the speaker which plays immediately after a successful trial. This setup worked well for our application, and we expect it would work well for many others.

Another limitation related to food rewards is that those which work well with ACTS require chewing and are deposited in a tray rather than directly into the mouth of the subject. Both the actions of retrieving and consuming the rewards take time and may slow the rate of trial completion. This characteristic may be ideal for enrichment activities and can be employed in experimental and training scenarios such as ours, especially because the autonomous nature of ACTS reduces the burden on researchers and encourages animals to learn in their home environment and at their own pace. However, we recognize that rewards deposited directly into the mouth of the subject may still be ideal in some scenarios and our system can be modified to operate juice reward systems accordingly.

We estimate that our low-cost feeder, with the configuration used for our subjects, supplies roughly 2 hours of continuous use. If longer sessions are desired, the feeder hopper can be modified accordingly. Furthermore, other similar feeders with larger hoppers can be used instead.

6.4.2 Open practices

The code written in MATLAB to run on the laptop and the code written in the Arduino IDE to run on the Wi-Fi transmitter/receiver, as well as the data generated by ACTS, are available in the Bitbucket repository https://djgriggs@bitbucket.org/yazdanlab/acts.git.

6.5 CRediT authorship contribution statement

Devon J. Griggs: Data curation, Investigation, Methodology, Project administration, Software, Visualization, Writing - original draft, Writing - review & editing. Julien Bloch: Data curation, Investigation, Methodology, Software, Writing - review & editing. Shivalika Chavan: Investigation, Methodology, Software, Writing - review & editing. Kali M. Coubrough: Investigation, Methodology, Software, Writing - review & editing. William Conley: Investigation, Methodology, Visualization, Writing - review & editing. Kelly Morrisroe: Resources, Supervision, Writing - review & editing. Azadeh Yazdan-Shahmorad: Conceptualization, Funding acquisition, Project administration, Supervision, Visualization, Writing - original draft, Writing - review & editing.

6.6 Declaration of Competing Interest

None.

6.7 Acknowledgements

The authors would like to thank Toni Haun and the Washington National Primate Center staff for technical help.

This project was supported by the Eunice Kennedy Shriver National Institute of Child Health & Human Development of the National Institutes of Health (K12HD073945, AY), the Washington National Primate Research Center (WaNPCR, P51 OD010425), the and Center for Neurotechnology (CNT, a National Science Foundation Engineering Research Center, EEC-1028725, DJG and JB). This project was also supported by the Mary Gates Endowment for Students (KB and SC), the University of Washington Institute for Neuroengineering (SC), and the University of Washington's Big Data for Genomics & Neuroscience Training Grant (JB).

Chapter 7: Conclusion and future directions

I have presented a collection of methods making optogenetic non-human primate (NHP) studies more accessible to researchers. Chapter 2 presented surgical planning techniques and Chapter 3 presented a novel, optical access-oriented electrode array, both of which culminate in a large-scale optogenetic interface presented in Chapter 4. Chapter 5 presented methods for data-guided planning of convection enhanced-delivery (CED) in NHPs, which promises to support future large-scale optogenetic interfaces based off of my presented work. Finally, Chapter 6 presented methods for training NHPs to perform behavioral tasks from the convenience of their home-cage, which is broadly applicable to neuroscience study in NHPs.

While these contributions to the scientific field are notable, more study and development are needed to perpetuate the accessibility, and ultimately the productivity, of NHP research. Concerning surgical planning presented in Chapter 2 (Ojemann *et al.*, 2020), further automation of the brain and skull modeling methods, although not required for success, would surely be welcomed. For example, recent years have seen great strides in the realms of data processing, such as machine learning techniques, which have the potential to further increase accessibility and speed of anatomy modeling and other surgical preparation steps.

The MMAD presented in Chapter 3 (Griggs *et al.*, 2021b) set the stage for tantalizing neuroscience pursuits. I have already used my presented multi-modal artificial dura (MMAD) to assist in the development of a lesioning toolbox for NHPs (Khateeb *et al.*, 2022), which prepares us for studying stroke and brain injuries, and developing novel neuroprotective techniques. My work also bolsters the field for exciting development of additional optogenetically-oriented electrocorticography (ECoG) arrays for NHPs. For example, more research is needed to optimize electrode sizes, spacing, and electrical characteristics of the MMAD as well as other ECoG arrays.

The large-scale, chronic optogenetic interface for NHPs presented in Chapter 4 (which is based on (Griggs, Khateeb, Philips, Chan, Ojemann, Yazdan-Shahmorad, *et al.*, 2019; Griggs, Belloir and Yazdan-Shahmorad, 2021; Griggs, Bloch, *et al.*, 2022)) pushes the limits of multimodal experimentation and my early work on large-scale optical access has been recognized by the field (De La Crompe, Coulon and Diester, 2020). While the culmination of this work is not yet complete, the neural and behavioral effects presented suggest that my interface may be used to study critical areas of neuroscience such as functional connectivity (Yazdan-Shahmorad, Silversmith, *et al.*, 2018; Bloch *et al.*, 2019, 2022), stroke models (K Khateeb *et al.*, 2019; Khateeb *et al.*, 2022; Zhou *et al.*, 2022), and other neurological diseases and disorders. My work invites integration of other optical stimulation and imaging techniques, as well as further development of the MMAD and other ECoG arrays, as briefly discussed above. Finally, my work may be applicable to other large-animal models and thus expand the diversity of animal models used in research.

Chapter 5 (Griggs, Garcia, *et al.*, 2022) extended the surgical planning techniques presented in Chapter 2 (Ojemann *et al.*, 2020) by providing a novel, data-guided, quantitative approach to CED planning. CED is a powerful technique of quickly delivering optogenetic viral vectors to large volumes of neural tissue, and my work serves to increase the likelihood of success in such surgical operations. With this being said, further research and development of anatomical brain models, cannula designs, and infusion protocols would build on the power of my methods and make large-scale delivery of optogenetic agents, as well as other agents, more accessible for large brains.

Finally, Chapter 7 provides a low-cost method of training NHPs to perform behavioral tasks with a touch-screen (Griggs *et al.*, 2020). My system contributed to the training of the animals used for behavioral data

collection in Chapter 4, and my work has been recognized by the field (Womelsdorf *et al.*, 2021). The system is flexible and thus could be improved in a number of ways, such as incorporating additional tasks or equipping the system with a low-cost juice reward system. Further research is needed to identify the optimal methods of training NHPs to perform tasks, and future iterations of the system may be needed to facilitate such methods.

The tremendous weight of neurological damage, diseases, and disorders throughout the world calls for efficient study of neuroscience and neuropathology, with the hope that effective therapies will be developed. My work serves as a step towards making optogenetics in NHPs, which is a critical area for translational research, more accessible to researchers.

References

Acker, L. *et al.* (2016) 'FEF inactivation with improved optogenetic methods', *Proc Natl Acad Sci U S A*. 2016/11/04, 113(46), pp. E7297–E7306. doi: 10.1073/pnas.1610784113.

Adhikari, A. *et al.* (2015) 'Basomedial amygdala mediates top-down control of anxiety and fear', *Nature*, 527(7577), pp. 179–185. doi: 10.1038/nature15698.

An, L., Qin, J. and Wang, R. K. (2010) 'Ultrahigh sensitive optical microangiography for in vivo imaging of microcirculations within human skin tissue beds', *Opt Express*. 2010/07/01, 18(8), pp. 8220–8228. doi: 10.1364/OE.18.008220.

Andrews, M. W. and Rosenblum, L. A. (1994) 'Diurnal Pattern of Joystick Use by Bonnet Macaques for Food Reward: Effects of Time-Limited Access', *Learning and Motivation*, (25), pp. 95–104.

Arieli, A., Grinvald, A. and Slovin, H. (2002) 'Dural substitute for long-term imaging of cortical activity in behaving monkeys and its clinical implications', *Journal of Neuroscience Methods*, 114(2), pp. 119–133. doi: 10.1016/S0165-0270(01)00507-6.

Barnett, S. C. *et al.* (2018) 'Optogenetic stimulation: Understanding memory and treating deficits', *Hippocampus*, 28(7), pp. 457–470. doi: 10.1002/hipo.22960.

Belloir, T. *et al.* (2022) 'iScience Large-scale multimodal surface neural interfaces for non-human primates', *ISCIENCE*.

Bennett, A. J. *et al.* (2016) 'Moving evidence into practice: cost analysis and assessment of macaques' sustained behavioral engagement with videogames and foraging devices.', *American journal of primatology*. United States, 78(12), pp. 1250–1264. doi: 10.1002/ajp.22579.

Berger, M. *et al.* (2018) 'Standardized automated training of rhesus monkeys for neuroscience research in their housing environment', *Journal of Neurophysiology*, 119(3), pp. 796–807. doi: 10.1152/jn.00614.2017.

Berger, M., Agha, N. S. and Gail, A. (2020) 'Wireless recording from unrestrained monkeys reveals motor goal encoding beyond immediate reach in frontoparietal cortex', *bioRxiv*. Cold Spring Harbor Laboratory. doi: 10.1101/305334.

Bliss-Moreau, E., Costa, V. D. and Baxter, M. G. (2022) 'A pragmatic reevaluation of the efficacy of nonhuman primate optogenetics for psychiatry', *Oxford Open Neuroscience*, 1(May), pp. 1–7. doi: 10.1093/oons/kvac006.

Bloch, J. *et al.* (2022) 'iScience ll Network structure mediates functional reorganization induced by optogenetic stimulation of non-human primate sensorimotor cortex', *ISCIENCE*. The Author(s), 25(5), p. 104285. doi: 10.1016/j.isci.2022.104285.

Bloch, J. A. *et al.* (2019) 'Cortical Stimulation Induces Network-Wide Coherence Change in Non-Human Primate Somatosensory Cortex∗', *Proceedings of the Annual International Conference of the IEEE Engineering in Medicine and Biology Society, EMBS*. IEEE, pp. 6446–6449. doi: 10.1109/EMBC.2019.8856633.

Blonde, J. D. *et al.* (2018) 'Customizable cap implants for neurophysiological experimentation', *J Neurosci Methods*. 2018/04/26, 304, pp. 103–117. doi: 10.1016/j.jneumeth.2018.04.016.

Bonini, L. (2019) 'Refinement techniques in non-human primate neuroscientific research.', *Annali dell'Istituto superiore di sanita*. Italy, 55(4), pp. 408–412. doi: 10.4415/ANN_19_04_18.

Borton, D. A. *et al.* (2013) 'An implantable wireless neural interface for recording cortical circuit dynamics in moving primates', *Journal of Neural Engineering*. {IOP} Publishing, 10(2), p. 26010. doi: 10.1088/1741-2560/10/2/026010.

Bosman, C. A. *et al.* (2012) 'Article Attentional Stimulus Selection through Selective Synchronization between Monkey Visual Areas', *Neuron*. Elsevier Inc., 75(5), pp. 875–888. doi: 10.1016/j.neuron.2012.06.037.

Boyden, E. S. *et al.* (2005) 'Millisecond-timescale, genetically targeted optical control of neural activity', *Nat Neurosci*, 8(9), pp. 1263–1268. doi: 10.1038/nn1525.

Brainard, D. H. (1997) 'The Psychophysics Toolbox', *Spatial Vision*, 10(4), pp. 433–436.

Butler, J. L. and Kennerley, S. W. (2019) 'Mymou: A low-cost, wireless touchscreen system for automated training of nonhuman primates', *Behavior Research Methods*. Behavior Research Methods, 51(6), pp. 2559–2572. doi: 10.3758/s13428-018-1109-5.

Calapai, A. *et al.* (2017) 'A cage-based training, cognitive testing and enrichment system optimized for rhesus macaques in neuroscience research', *Behavior Research Methods*. Behavior Research Methods, 49(1), pp. 35–45. doi: 10.3758/s13428-016-0707-3.

Camporeze, B. *et al.* (2018) 'Optogenetics: the new molecular approach to control functions of neural cells in epilepsy, depression and tumors of the central nervous system.', *American journal of cancer research*, 8(10), pp. 1900–1918. Available at: http://www.ncbi.nlm.nih.gov/pubmed/30416844%0Ahttp://www.pubmedcentral.nih.gov/articlerender.fcgi?artid=PMC6220144.

Camus, S. *et al.* (2015) 'Why bother using non-human primate models of cognitive disorders in translational research?', *Neurobiology of Learning and Memory*. Elsevier Inc., 124, pp. 123–129. doi: 10.1016/j.nlm.2015.06.012.

Carrera, E. and Tononi, G. (2014) 'Diaschisis: Past, present, future', *Brain*, 137(9), pp. 2408–2422. doi: 10.1093/brain/awu101.

Carter, M. E. and de Lecea, L. (2011) 'Optogenetic investigation of neural circuits in vivo', *Trends in Molecular Medicine*. Elsevier Ltd, 17(4), pp. 197–206. doi: 10.1016/j.molmed.2010.12.005.

Chail, A. *et al.* (2018) 'Transcranial magnetic stimulation: A review of its evolution and current applications YR - 2018/7/1', *Industrial Psychiatry Journal*, (2 UL-https://www.industrialpsychiatry.org/article.asp?issn=0972-6748;year=2018;volume=27;issue=2;spage=172;epage=180;aulast=Chail;t=5), pp. 172 OP-180 VO–27. doi: 10.4103/ipj.ipj_88_18.

Chao, Z. C. *et al.* (2018) 'Large-Scale Cortical Networks for Hierarchical Prediction and Prediction Error in the Primate Brain', *Neuron*. Elsevier Inc., 100(5), pp. 1252-1266.e3. doi: 10.1016/j.neuron.2018.10.004.

Chen, B. T. *et al.* (2013) 'Rescuing cocaine-induced prefrontal cortex hypoactivity prevents compulsive cocaine seeking', *Nature*. Nature Publishing Group, 496(7445), pp. 359–362. doi: 10.1038/nature12024.

Chen, L. M. *et al.* (2002) 'A chamber and artificial dura method for long-term optical imaging in the

monkey', *Journal of Neuroscience Methods*, 113(1), pp. 41–49. doi: 10.1016/S0165-0270(01)00475-7.

Chen, L. M., Friedman, R. M. and Roe, A. W. (2005) 'Optical imaging of SI topography in anesthetized and awake squirrel monkeys', *Journal of Neuroscience*, 25(33), pp. 7648–7659. doi: 10.1523/JNEUROSCI.1990-05.2005.

Chen, R. C.-H. *et al.* (2020) 'A system identification analysis of optogenetically evoked electrocorticography and cerebral blood flow responses', *Journal of Neural Engineering*. Available at: http://iopscience.iop.org/10.1088/1741-2552/ab89fc.

Chen, Z. J. *et al.* (2004) 'A realistic brain tissue phantom for intraparenchymal infusion studies', *J Neurosurg*. 2004/08/18, 101(2), pp. 314–322. doi: 10.3171/jns.2004.101.2.0314.

Cheng, H. *et al.* (2018) 'Prolonged operative duration is associated with complications: a systematic review and meta-analysis', *J Surg Res*. 2018/06/26, 229, pp. 134–144. doi: 10.1016/j.jss.2018.03.022.

Chernov, M. and Roe, A. W. (2014) 'Infrared neural stimulation: a new stimulation tool for central nervous system applications', *Neurophotonics*, 1(1), p. 011011. doi: 10.1117/1.nph.1.1.011011.

Chiang, C.-H., Lee, J., *et al.* (2020) 'A modular high-density $\upmu${ECoG} system on macaque {vlPFC} for auditory cognitive decoding', *Journal of Neural Engineering*. {IOP} Publishing, 17(4), p. 46008. doi: 10.1088/1741-2552/ab9986.

Chiang, C.-H., Won, S. M., *et al.* (2020) 'Development of a neural interface for high-definition, long-term recording in rodents and nonhuman primates', *Science Translational Medicine*, 12(538), p. eaay4682. doi: 10.1126/scitranslmed.aay4682.

Chiang, C.-H. H. *et al.* (2019) 'A modular high-density 294-channel µECoG system on macaque vlPFC for auditory cognitive decoding', *bioRxiv*, p. 768127. doi: 10.1101/768127.

Choi, I. A. *et al.* (2018) 'Effect of inhibition of DNA methylation combined with task-specific training on chronic stroke recovery', *International Journal of Molecular Sciences*, 19(7). doi: 10.3390/ijms19072019.

Chuong, A. S. *et al.* (2014) 'Noninvasive optical inhibition with a red-shifted microbial rhodopsin', *Nature Neuroscience*. Nature Publishing Group, 17(8), pp. 1123–1129. doi: 10.1038/nn.3752.

Deegan, A. J. *et al.* (2018) 'Optical coherence tomography angiography monitors human cutaneous wound healing over time', *Quantitative Imaging in Medicine and Surgery*, 8(2), pp. 135–150. doi: 10.21037/qims.2018.02.07.

Dong, D. *et al.* (2018) 'Dysfunction of Large-Scale Brain Networks in Schizophrenia: A Meta-analysis of Resting-State Functional Connectivity', *Schizophrenia Bulletin*, 44(1), pp. 168–181. doi: 10.1093/schbul/sbx034.

Fagot, J. and Bonté, E. (2010) 'Automated testing of cognitive performance in monkeys: Use of a battery of computerized test systems by a troop of semi-free-ranging baboons (Papio papio)', *Behavior Research Methods*, 42(2), pp. 507–516. doi: 10.3758/BRM.42.2.507.

Fagot, J. and Paleressompoulle, D. (2009) 'Automatic testing of cognitive performance in baboons maintained in social groups', *Behavior Research Methods*, 41(2), pp. 396–404. doi: 10.3758/BRM.41.2.396.

Fernandez-Leon, J. A. *et al.* (2015) 'A wireless transmission neural interface system for unconstrained non-human primates', *Journal of Neural Engineering*. {IOP} Publishing, 12(5), p. 56005. doi:

10.1088/1741-2560/12/5/056005.

Ferster, C. B. and Skinner, B. F. (1957) *Schedules of reinforcement*. Appleton-Century-Crofts.

Fredericks, J. M. *et al.* (2020a) 'Methods for mechanical delivery of viral vectors into rhesus monkey brain', *Journal of Neuroscience Methods*. Elsevier, 339(April), p. 108730. doi: 10.1016/j.jneumeth.2020.108730.

Fredericks, J. M. *et al.* (2020b) 'Methods for mechanical delivery of viral vectors into rhesus monkey brain', *Journal of Neuroscience Methods*. Elsevier, 339(February), p. 108730. doi: 10.1016/j.jneumeth.2020.108730.

Frías, I. *et al.* (2018) 'Interhemispheric connectivity of primary sensory cortex is associated with motor impairment after stroke', *Scientific Reports*, 8(1), pp. 1–10. doi: 10.1038/s41598-018-29751-6.

Fukushima, M., Chao, Z. C. and Fujii, N. (2015) 'Studying brain functions with mesoscopic measurements: Advances in electrocorticography for non-human primates', *Current Opinion in Neurobiology*. Elsevier Ltd, 32, pp. 124–131. doi: 10.1016/j.conb.2015.03.015.

Galvan, A. *et al.* (2017) 'Nonhuman primate optogenetics: Recent advances and future directions', *Journal of Neuroscience*. 2017/11/10, 37(45), pp. 10894–10903. doi: 10.1523/JNEUROSCI.1839-17.2017.

Galvan, A., Caiola, M. J. and Albaugh, D. L. (2018) 'Advances in optogenetic and chemogenetic methods to study brain circuits in non-human primates', *J Neural Transm (Vienna)*. 2017/02/27. Springer Vienna, 125(3), pp. 547–563. doi: 10.1007/s00702-017-1697-8.

Gazes, R. P. *et al.* (2013) 'Automated cognitive testing of monkeys in social groups yields results comparable to individual laboratory-based testing', *Animal Cognition*, 16(3), pp. 445–458. doi: 10.1007/s10071-012-0585-8.

Gradinaru, V. *et al.* (2009) 'Optical deconstruction of parkinsonian neural circuitry', *Science*, 324(5925), pp. 354–359. doi: 10.1126/science.1167093.

Griggs, D. J., Khateeb, K., Philips, S., Chan, J. W., Ojemann, W., Yazdan-Shahmorad, A., *et al.* (2019) 'Optimized large-scale optogenetic interface for non-human primates', *SPIE BiOS*, 1086605(February), p. 3. doi: 10.1117/12.2511317.

Griggs, D. J., Khateeb, K., Philips, S., Chan, J. W., Ojemann, W. and Yazdan-Shahmorad, A. (2019) 'Optimized large-scale optogenetic interface for non-human primates', p. 3. doi: 10.1117/12.2511317.

Griggs, D. J. *et al.* (2020) 'Autonomous cage-side system for remote training of non-human primates', *Journal of Neuroscience Methods*. Elsevier B.V., 348(October 2020), p. 108969. doi: 10.1016/j.jneumeth.2020.108969.

Griggs, D. J. *et al.* (2021a) 'Multi-modal artificial dura for simultaneous large-scale optical access and large-scale electrophysiology in non-human primate cortex', *Journal of Neural Engineering, Special Issue 'Neuroelectronic Interfaces'*, 18(5), p. 2021.02.03.429596. doi: 10.1101/2021.02.03.429596.

Griggs, D. J. *et al.* (2021b) 'Multi-modal artificial dura for simultaneous large-scale optical access and large-scale electrophysiology in non-human primate cortex', *bioRxiv*, p. 2021.02.03.429596. doi: 10.1101/2021.02.03.429596.

Griggs, D. J., Bloch, J., *et al.* (2022) 'Demonstration of an Optimized Large-scale Optogenetic Cortical Interface for Non-human Primates', *Ieee*, 119395, pp. 1–4.

Griggs, D. J., Garcia, A. D., *et al.* (2022) 'Improving the efficacy and accessibility of intracranial viral vector delivery in non-human primates', *Pharmaceutics*, p. 2022.06.06.494543. doi: 10.1101/2022.06.06.494543.

Griggs, D. J., Belloir, T. and Yazdan-Shahmorad, A. (2021) 'Large-scale neural interfaces for optogenetic actuators and sensors in non-human primates', *SPIE BiOS*, 1166305(March), p. 17. doi: 10.1117/12.2579431.

Hampton, R. R. *et al.* (2004) 'Method for making selective lesions of the hippocampus in Macaque monkeys using NMDA and a longitudinal surgical approach', *Hippocampus*, 14(1), pp. 9–18. doi: 10.1002/hipo.10150.

Han, X. (2012) 'Optogenetics in the nonhuman primate', *Prog Brain Res*. 2012/02/22, 196, pp. 215–233. doi: 10.1016/B978-0-444-59426-6.00011-2.

Harding, J. D. (2017) 'Nonhuman primates and translational research: Progress, opportunities, and challenges', *ILAR Journal*, 58(2), pp. 141–150. doi: 10.1093/ilar/ilx033.

Huijgen, J. and Samson, S. (2015) 'The hippocampus: A central node in a large-scale brain network for memory', *Revue Neurologique*. Elsevier Masson SAS, 171(3), pp. 204–216. doi: 10.1016/j.neurol.2015.01.557.

Hunt Bobo, R. *et al.* (1994) 'Convection-enhanced delivery of macromolecules in the brain', *Proceedings of the National Academy of Sciences of the United States of America*, 91(6), pp. 2076–2080. doi: 10.1073/pnas.91.6.2076.

Jackson, A. *et al.* (2006) 'The neurochip BCI: towards a neural prosthesis for upper limb function', *IEEE Transactions on Neural Systems and Rehabilitation Engineering*, 14(2), pp. 187–190. doi: 10.1109/TNSRE.2006.875547.

Jackson, A., Mavoori, J. and Fetz, E. E. (2006) 'Long-term motor cortex plasticity induced by an electronic neural implant', *Nature*, 444(7115), pp. 56–60. doi: 10.1038/nature05226.

Jackson, A., Mavoori, J. and Fetz, E. E. (2007) 'Correlations Between the Same Motor Cortex Cells and Arm Muscles During a Trained Task, Free Behavior, and Natural Sleep in the Macaque Monkey', *Journal of Neurophysiology*, 97(1), pp. 360–374. doi: 10.1152/jn.00710.2006.

Jeong, W., Chung, C. K. and Kim, J. S. (2015) 'Episodic memory in aspects of large-scale brain networks', *Frontiers in Human Neuroscience*, 9(AUGUST), pp. 1–15. doi: 10.3389/fnhum.2015.00454.

Ji, B. *et al.* (2017) 'Flexible Optoelectric Neural Interface Integrated Wire-Bonding μ LEDs and Microelectrocorticography for Optogenetics', *IEEE Transactions on Electron Devices*. IEEE, 64(5), pp. 2008–2015. doi: 10.1109/TED.2016.2645860.

Ji, B. *et al.* (2018) 'Flexible polyimide-based hybrid opto-electric neural interface with 16 channels of micro-LEDs and electrodes', *Microsystems and Nanoengineering*. Springer US, 4(1). doi: 10.1038/s41378-018-0027-0.

Jiang, W., Tremblay, F. and Elaine Chapman, C. (2018) 'Context-dependent tactile texture-sensitivity in monkey M1 and S1 cortex', *Journal of Neurophysiology*, 120(5), pp. 2334–2350. doi: 10.1152/jn.00081.2018.

Ju, N. *et al.* (2018) 'Long-term all-optical interrogation of cortical neurons in awake-behaving nonhuman

primates', *PLoS Biol*. 2018/08/09, 16(8), p. e2005839. doi: 10.1371/journal.pbio.2005839.

Kaiju, T. *et al.* (2021) 'High-density mapping of primate digit representations with a 1152-channel μECoG array', *Journal of Neural Engineering*. Available at: http://iopscience.iop.org/article/10.1088/1741-2552/abe245.

Kells, A. P. *et al.* (2009) 'Efficient gene therapy-based method for the delivery of therapeutics to primate cortex', *Proceedings of the National Academy of Sciences of the United States of America*, 106(7), pp. 2407–2411. doi: 10.1073/pnas.0810682106.

Khateeb, Karam, Yao, Z., *et al.* (2019) 'A Practical Method for Creating Targeted Focal Ischemic Stroke in the Cortex of Nonhuman Primates(.)', *Conf Proc IEEE Eng Med Biol Soc*. 2020/01/18. IEEE, 2019, pp. 3515–3518. doi: 10.1109/EMBC.2019.8857741.

Khateeb, K *et al.* (2019) 'A Practical Method for Creating Targeted Focal Ischemic Stroke in the Cortex of Nonhuman Primates(.)', *Conf Proc IEEE Eng Med Biol Soc*. 2020/01/18, 2019, pp. 3515–3518. doi: 10.1109/EMBC.2019.8857741.

Khateeb, Karam, Griggs, D. J., *et al.* (2019) 'Convection Enhanced Delivery of Optogenetic Adeno-associated Viral Vector to the Cortex of Rhesus Macaque Under Guidance of Online MRI Images', *J Vis Exp*. 2019/06/11, (147), pp. 1–8. doi: 10.3791/59232.

Khateeb, K. *et al.* (2022) 'A versatile toolbox for studying cortical physiology in primates', *Cell Reports Methods*. The Author(s), p. 100183. doi: 10.1016/j.crmeth.2022.100183.

Klapoetke, N. C. *et al.* (2014) 'Independent optical excitation of distinct neural populations', *Nature Methods*, 11(3), pp. 338–346. doi: 10.1038/nmeth.2836.

Kleinbart, J. E. *et al.* (2018) 'A Modular Implant System for Multimodal Recording and Manipulation of the Primate Brain', *Proceedings of the Annual International Conference of the IEEE Engineering in Medicine and Biology Society, EMBS*. IEEE, 2018-July, pp. 3362–3365. doi: 10.1109/EMBC.2018.8512993.

Kleiner, M., Brainard, D. H. and Pelli, D. G. (2007) 'What's new in Psychtoolbox-3?', in *Perception 36 ECVP Abstract Supplement*.

Komatsu, M. *et al.* (2017) 'A chronically implantable bidirectional neural interface for non-human primates', *Frontiers in Neuroscience*, 11(SEP), pp. 1–9. doi: 10.3389/fnins.2017.00514.

Krauze, M T *et al.* (2005) 'Reflux-free cannula for convection-enhanced high-speed delivery of therapeutic agents', *J Neurosurg*. 2005/11/25, 103(5), pp. 923–929. doi: 10.3171/jns.2005.103.5.0923.

Krauze, Michal T. *et al.* (2005) 'Reflux-free cannula for convection-enhanced high-speed delivery of therapeutic agents', *J Neurosurg*. 2005/11/25, 103(5), pp. 923–929. doi: 10.3171/jns.2005.103.5.0923.

Kuzum, D. *et al.* (2014) 'Transparent and flexible low noise graphene electrodes for simultaneous electrophysiology and neuroimaging', *Nature Communications*. Nature Publishing Group, 5(May), pp. 1–10. doi: 10.1038/ncomms6259.

Kwon, K. Y. *et al.* (2012) 'Opto-μECoG array: Transparent μeCoG electrode array and integrated LEDs for optogenetics', *2012 IEEE Biomedical Circuits and Systems Conference: Intelligent Biomedical Electronics and Systems for Better Life and Better Environment, BioCAS 2012 - Conference Publications*. IEEE, pp. 164–167. doi: 10.1109/BioCAS.2012.6418471.

De La Crompe, B., Coulon, P. and Diester, I. (2020) 'Functional interrogation of neural circuits with virally

transmitted optogenetic tools', *Journal of Neuroscience Methods*. Elsevier, 345(March), p. 108905. doi: 10.1016/j.jneumeth.2020.108905.

Lanius, R. A. *et al.* (2015) 'Restoring large-scale brain networks in ptsd and related disorders: A proposal for neuroscientifically-informed treatment interventions', *European Journal of Psychotraumatology*, 6, pp. 1–12. doi: 10.3402/ejpt.v6.27313.

Ledochowitsch, P. *et al.* (2015) 'Strategies for optical control and simultaneous electrical readout of extended cortical circuits', *J Neurosci Methods*, 256, pp. 220–231. doi: 10.1016/j.jneumeth.2015.07.028.

Li, H. J. *et al.* (2015) 'Putting age-related task activation into large-scale brain networks: A meta-analysis of 114 fMRI studies on healthy aging', *Neuroscience and Biobehavioral Reviews*. Elsevier Ltd, 57(16), pp. 156–174. doi: 10.1016/j.neubiorev.2015.08.013.

Li, M. *et al.* (2017) 'Long-Term Two-Photon Imaging in Awake Macaque Monkey', *Neuron*. Elsevier Inc., 93(5), pp. 1049-1057.e3. doi: 10.1016/j.neuron.2017.01.027.

Libey, T. and Fetz, E. E. (2017) 'Open-source, low cost, free-behavior monitoring, and reward system for neuroscience research in non-human primates', *Frontiers in Neuroscience*, 11(MAY), pp. 1–12. doi: 10.3389/fnins.2017.00265.

Lieberman, D. M. *et al.* (1995) 'Convection-enhanced distribution of large molecules in gray matter during interstitial drug infusion', *Journal of Neurosurgery*. Journal of Neurosurgery Publishing Group, 82(6), pp. 1021–1029. doi: 10.3171/jns.1995.82.6.1021.

Liu, X. *et al.* (2018) 'A compact closed-loop optogenetics system based on artifact-free transparent graphene electrodes', *Frontiers in Neuroscience*, 12(MAR), pp. 1–13. doi: 10.3389/fnins.2018.00132.

Lonser, R. R. *et al.* (1998) 'Direct convective delivery of macromolecules to the spinal cord', *Journal of Neurosurgery*. Journal of Neurosurgery Publishing Group, 89(4), pp. 616–622. doi: 10.3171/jns.1998.89.4.0616.

Lonser, R. R. *et al.* (2002) 'Successful and safe perfusion of the primate brainstem: in vivo magnetic resonance imaging of macromolecular distribution during infusion', *Journal of Neurosurgery*. Journal of Neurosurgery Publishing Group, 97(4), pp. 905–913. doi: 10.3171/jns.2002.97.4.0905.

Lozano, A. M. *et al.* (2019) 'Deep brain stimulation: current challenges and future directions', *Nat Rev Neurol*. 2019/01/27, 15(3), pp. 148–160. doi: 10.1038/s41582-018-0128-2.

Lu, H. D. *et al.* (2010) 'A Motion Direction Map in Macaque V2', *Neuron*. Elsevier, 68(5), pp. 1002–1013. doi: 10.1016/j.neuron.2010.11.020.

Lucas, T. H. and Fetz, E. E. (2013) 'Myo-cortical crossed feedback reorganizes primate motor cortex output', *J Neurosci*. 2013/03/22, 33(12), pp. 5261–5274. doi: 10.1523/JNEUROSCI.4683-12.2013.

Macknik, S L *et al.* (2019) 'Advanced Circuit and Cellular Imaging Methods in Nonhuman Primates', *J Neurosci*. 2019/10/18, 39(42), pp. 8267–8274. doi: 10.1523/JNEUROSCI.1168-19.2019.

Macknik, Stephen L. *et al.* (2019) 'Advanced Circuit and Cellular Imaging Methods in Nonhuman Primates', *J Neurosci*. 2019/10/18, 39(42), pp. 8267–8274. doi: 10.1523/JNEUROSCI.1168-19.2019.

Mandell, D. J. and Sackett, G. P. (2010) 'Standard and Computer Testing Methods', *Gene*, 51(1), pp. 1–13. doi: 10.1002/dev.20329.Comparability.

Mao, T. *et al.* (2011) 'Long-Range Neuronal Circuits Underlying the Interaction between Sensory and Motor Cortex', *Neuron*. Elsevier Inc., 72(1), pp. 111–123. doi: 10.1016/j.neuron.2011.07.029.

May, T. *et al.* (2014) 'Detection of optogenetic stimulation in somatosensory cortex by non-human primates--towards artificial tactile sensation', *PLoS One*. 2014/12/30, 9(12), p. e114529. doi: 10.1371/journal.pone.0114529.

Mehta, A. M., Sonabend, A. M. and Bruce, J. N. (2017) 'Convection-Enhanced Delivery', *Neurotherapeutics*. Neurotherapeutics, 14(2), pp. 358–371. doi: 10.1007/s13311-017-0520-4.

Michikawa, T. *et al.* (2017) 'Automatic extraction of endocranial surfaces from CT images of crania', *PLoS One*. 2017/04/14, 12(4), p. e0168516. doi: 10.1371/journal.pone.0168516.

Mihalko, A. (2016) *CH340G CH34G CH34X Mac OS X driver: CH34x_Install_V1.3.pkg*. Available at: https://github.com/adrianmihalko/ch340g-ch34g-ch34x-mac-os-x-driver.

Milton, R., Shahidi, N. and Dragoi, V. (2020) 'Dynamic states of population activity in prefrontal cortical networks of freely-moving macaque', *Nature Communications*, 11(1), p. 1948. doi: 10.1038/s41467-020-15803-x.

Miranda, H. *et al.* (2010) 'HermesD: A High-Rate Long-Range Wireless Transmission System for Simultaneous Multichannel Neural Recording Applications', *IEEE Transactions on Biomedical Circuits and Systems*, 4(3), pp. 181–191. doi: 10.1109/TBCAS.2010.2044573.

Mitchell, A. S. *et al.* (2018) 'Continued need for non-human primate neuroscience research', *Current Biology*. doi: 10.1016/j.cub.2018.09.029.

Miyakawa, N. *et al.* (2018) 'Heterogeneous redistribution of facial subcategory information within and outside the face-selective domain in primate inferior temporal cortex', *Cerebral Cortex*, 28(4), pp. 1416–1431. doi: 10.1093/cercor/bhx342.

Nassi, J. J. *et al.* (2015) 'Optogenetic Activation of Normalization in Alert Macaque Visual Cortex', *Neuron*. Elsevier Inc., 86(6), pp. 1504–1517. doi: 10.1016/j.neuron.2015.05.040.

NIDCD (2021) *Cochlear Implants*. Available at: https://www.nidcd.nih.gov/health/cochlear-implants.

Nishimura, Y. *et al.* (2013) 'Spike-timing-dependent plasticity in primate corticospinal connections induced during free behavior', *Neuron*, 80(5), pp. 1301–1309. doi: 10.1016/j.neuron.2013.08.028.

Obi, K., Amano, I. and Takatsuru, Y. (2018) 'Role of dopamine on functional recovery in the contralateral hemisphere after focal stroke in the somatosensory cortex', *Brain Research*. Elsevier B.V., 1678, pp. 146–152. doi: 10.1016/j.brainres.2017.10.022.

Oh, J., Hofer, R. and Fitch, W. T. (2017) 'An open source automatic feeder for animal experiments', *HardwareX*. The Authors, 1, pp. 13–21. doi: 10.1016/j.ohx.2016.09.001.

Oh, S. *et al.* (2007) 'Improved distribution of small molecules and viral vectors in the murine brain using a hollow fiber catheter', *Journal of Neurosurgery*, 107(3), pp. 568–577. doi: 10.3171/JNS-07/09/0568.

Ojemann, W. K. S. *et al.* (2020) 'A mri-based toolbox for neurosurgical planning in nonhuman primates', *Journal of Visualized Experiments*, 2020(161), pp. 1–16. doi: 10.3791/61098.

Olmstead, T. A. *et al.* (2018) 'Transcranial and pulsed focused ultrasound that activates brain can accelerate remyelination in a mouse model of multiple sclerosis', *Journal of Therapeutic Ultrasound*.

Journal of Therapeutic Ultrasound, 6(1), pp. 1–11. doi: 10.1186/s40349-018-0119-1.

Orsborn, A. L. *et al.* (2015) 'Semi-chronic chamber system for simultaneous subdural electrocorticography, local field potentials, and spike recordings', *International IEEE/EMBS Conference on Neural Engineering, NER*. IEEE, 2015-July, pp. 398–401. doi: 10.1109/NER.2015.7146643.

Overton, J. A. *et al.* (2017) 'Improved methods for acrylic-free implants in nonhuman primates for neuroscience research', *J Neurophysiol*. 2017/09/01, 118(6), pp. 3252–3270. doi: 10.1152/jn.00191.2017.

Paxinos, G., Petrides, M. and Toga, A. W. (2008) *The Rhesus Monkey Brain in Stereotaxic Coordinates*. 2nd Editio. Elsevier Science.

Pelli, D. G. (1997) 'The VideoToolbox software for visual psychophysics: Transforming numbers into movies', *Spatial Vision*, 10(4), pp. 437–442.

Perdue, B. M., Beran, M. J. and Washburn, D. A. (2018) 'A computerized testing system for primates: Cognition, welfare, and the Rumbaughx', *Behavioural Processes*. Elsevier, 156(January 2017), pp. 37–50. doi: 10.1016/j.beproc.2017.12.019.

Phillips, K. A. *et al.* (2014) 'Why primate models matter', *American Journal of Primatology*, 76(9), pp. 801–827. doi: 10.1002/ajp.22281.

Pomfret, R., Miranpuri, G. and Sillay, K. (2013) 'The substitute brain and the potential of the gel model', *Annals of Neurosciences*, 20(3), pp. 118–122. doi: 10.5214/ans.0972.7531.200309.

Prescott, M. J. and Poirier, C. (2021) 'The role of MRI in applying the 3Rs to non-human primate neuroscience', *NeuroImage*. Elsevier Inc., 225(October 2020), p. 117521. doi: 10.1016/j.neuroimage.2020.117521.

Prezelski, K. *et al.* (2021) 'Design and Validation of a Multi-Point Injection Technology for MR-Guided Convection Enhanced Delivery in the Brain', *Frontiers in Medical Technology*, 3(October), pp. 1–12. doi: 10.3389/fmedt.2021.725844.

Rajalingham, R. *et al.* (2020) 'Chronically implantable LED arrays for behavioral optogenetics in primates', *bioRxiv*, p. 2020.09.10.291583. Available at: https://doi.org/10.1101/2020.09.10.291583.

Rajalingham, R. *et al.* (2021) 'Chronically implantable LED arrays for behavioral optogenetics in primates', *Nature Methods*. Springer US, 18(9), pp. 1112–1116. doi: 10.1038/s41592-021-01238-9.

Reddy, J. W. *et al.* (2019) 'Flexible, Monolithic, High-Density µlED Neural Probes for Simultaneous Optogenetics Stimulation and Recording', *International IEEE/EMBS Conference on Neural Engineering, NER*. IEEE, 2019-March, pp. 831–834. doi: 10.1109/NER.2019.8717116.

René, C. A. and Parks, R. J. (2021) 'Delivery of therapeutic agents to the central nervous system and the promise of extracellular vesicles', *Pharmaceutics*, 13(4). doi: 10.3390/pharmaceutics13040492.

Renz, A. F. *et al.* (2020) 'Opto-E-Dura: A Soft, Stretchable ECoG Array for Multimodal, Multiscale Neuroscience', *Advanced Healthcare Materials*, 9(17), pp. 1–26. doi: 10.1002/adhm.202000814.

Richardson, W. K. *et al.* (1990) 'The NASA/LRC computerized test system', *Behavior Research Methods, Instruments, & Computers*, 22(2), pp. 127–131. doi: 10.3758/BF03203132.

Richner, T. J. *et al.* (2014) 'Optogenetic micro-electrocorticography for modulating and localizing

cerebral cortex activity', *Journal of Neural Engineering*, 11(1). doi: 10.1088/1741-2560/11/1/016010.

Ruggiero, R. N. *et al.* (2017) 'Cannabinoids and vanilloids in schizophrenia: Neurophysiological evidence and directions for basic research', *Frontiers in Pharmacology*, 8(JUN), pp. 1–27. doi: 10.3389/fphar.2017.00399.

Ruiz, O. *et al.* (2013) 'Optogenetics through windows on the brain in the nonhuman primate', *J Neurophysiol*. 2013/06/14, 110(6), pp. 1455–1467. doi: 10.1152/jn.00153.2013.

Russell, W. and Burch, R. (1959) *The principles of humane experimental technique*. London, UK: Methuen.

Sahel, J. A. *et al.* (2021) 'Partial recovery of visual function in a blind patient after optogenetic therapy', *Nature Medicine*. doi: 10.1038/s41591-021-01351-4.

Sanftner, L. M. *et al.* (2005) 'AAV2-mediated gene delivery to monkey putamen: Evaluation of an infusion device and delivery parameters', *Experimental Neurology*, 194(2), pp. 476–483. doi: 10.1016/j.expneurol.2005.03.007.

Schwarz, D. A. *et al.* (2014) 'Chronic, wireless recordings of large-scale brain activity in freely moving rhesus monkeys', *Nature Methods*, 11(6), pp. 670–676. doi: 10.1038/nmeth.2936.

Schweizer-Gorgas, D. *et al.* (2018) 'Magnetic resonance imaging features of canine gliomatosis cerebri', *Vet Radiol Ultrasound*. 2017/11/08, 59(2), pp. 180–187. doi: 10.1111/vru.12570.

Sedaghat-Nejad, E. *et al.* (2019) 'Behavioral training of marmosets and electrophysiological recording from the cerebellum', *J Neurophysiol*. 2019/08/08, 122(4), pp. 1502–1517. doi: 10.1152/jn.00389.2019.

Seeman, S. C. *et al.* (2017) 'Paired stimulation for spike-timing-dependent plasticity in primate sensorimotor cortex', *Journal of Neuroscience*, 37(7), pp. 1935–1949. doi: 10.1523/JNEUROSCI.2046-16.2017.

Seidemann, E. *et al.* (2016) 'Calcium imaging with genetically encoded indicators in behaving primates', *eLife*, 5(2016JULY), pp. 1–19. doi: 10.7554/eLife.16178.

Seok, J. *et al.* (2013) 'Genomic responses in mouse models poorly mimic human inflammatory diseases', *Proc Natl Acad Sci U S A*. 2013/02/13, 110(9), pp. 3507–3512. doi: 10.1073/pnas.1222878110.

Shahidi, N. *et al.* (2019) 'Population coding of strategic variables during foraging in freely-moving macaques', *bioRxiv*. Cold Spring Harbor Laboratory. doi: 10.1101/811992.

Shi, L. *et al.* (2018) 'Large-scale brain network connectivity underlying creativity in resting-state and task fMRI: Cooperation between default network and frontal-parietal network', *Biological Psychology*. Elsevier, 135(2), pp. 102–111. doi: 10.1016/j.biopsycho.2018.03.005.

Shtoyerman, E. *et al.* (2000) 'Long-term optical imaging and spectroscopy reveal mechanisms underlying the intrinsic signal and stability of cortical maps in V1 of behaving monkeys', *Journal of Neuroscience*, 20(21), pp. 8111–8121. doi: 10.1523/jneurosci.20-21-08111.2000.

Simmons, J. M. *et al.* (2008) 'Mapping prefrontal circuits in vivo with manganese-enhanced magnetic resonance imaging in monkeys', *Journal of Neuroscience*, 28(30), pp. 7637–7647. doi: 10.1523/JNEUROSCI.1488-08.2008.

Slovin, H. *et al.* (2002) 'Long-term voltage-sensitive dye imaging reveals cortical dynamics in behaving

monkeys', *Journal of Neurophysiology*, 88(6), pp. 3421–3438. doi: 10.1152/jn.00194.2002.

Soliman, A. S. *et al.* (2017) 'A realistic phantom for validating MRI-based synthetic CT images of the human skull', *Med Phys*. 2017/06/24, 44(9), pp. 4687–4694. doi: 10.1002/mp.12428.

Spellman, T. *et al.* (2015) 'Hippocampal-prefrontal input supports spatial encoding in working memory', *Nature*, 522(7556), pp. 309–314. doi: 10.1038/nature14445.

Stamatakis, A. M. *et al.* (2018) 'Simultaneous optogenetics and cellular resolution calcium imaging during active behavior using a miniaturized microscope', *Frontiers in Neuroscience*, 12(JUL), pp. 1–16. doi: 10.3389/fnins.2018.00496.

Strange, B. A. *et al.* (2014) 'Functional organization of the hippocampal longitudinal axis', *Nature Reviews Neuroscience*. Nature Publishing Group, 15(10), pp. 655–669. doi: 10.1038/nrn3785.

Su, Y. *et al.* (2016) 'A wireless 32-channel implantable bidirectional brain machine interface', *Sensors (Switzerland)*, 16(10), pp. 1–18. doi: 10.3390/s16101582.

Szerlip, N. J. *et al.* (2007) 'Real-time imaging of convection-enhanced delivery of viruses and virus-sized particles.', *Journal of neurosurgery*. United States, 107(3), pp. 560–567. doi: 10.3171/JNS-07/09/0560.

Ting, J. T. and Feng, G. (2014) 'Recombineering strategies for developing next generation BAC transgenic tools for optogenetics and beyond', *Frontiers in Behavioral Neuroscience*, 8(APR), pp. 1–13. doi: 10.3389/fnbeh.2014.00111.

Tønnesen, J. (2013) 'Optogenetic cell control in experimental models of neurological disorders', *Behavioural Brain Research*. Elsevier B.V., 255, pp. 35–43. doi: 10.1016/j.bbr.2013.07.007.

Tremblay, S. *et al.* (2020) 'An Open Resource for Non-human Primate Optogenetics', *Neuron*, pp. 1–16. doi: 10.1016/j.neuron.2020.09.027.

Truppa, V. *et al.* (2010) 'Identity concept learning in matching-to-sample tasks by tufted capuchin monkeys (Cebus apella)', *Animal Cognition*, 13(6), pp. 835–848. doi: 10.1007/s10071-010-0332-y.

Tulip, J. *et al.* (2017) 'An automated system for positive reinforcement training of group-housed macaque monkeys at breeding and research facilities', *Journal of Neuroscience Methods*. Elsevier B.V., 285, pp. 6–18. doi: 10.1016/j.jneumeth.2017.04.015.

Wang, S. *et al.* (2020) 'Ultrasonic Neuromodulation and Sonogenetics: A New Era for Neural Modulation', *Frontiers in Physiology*, 11. doi: 10.3389/fphys.2020.00787.

Washburn, D. A. and Rumbaugh, D. M. (1992) 'Testing primates with joystick-based automated apparatus: Lessons from the Language Research Center's Computerized Test System', *Behavior Research Methods, Instruments, & Computers*, 24(2), pp. 157–164. doi: 10.3758/BF03203490.

Weed, M. R. *et al.* (1999) 'Performance norms for a rhesus monkey neuropsychological testing battery: Acquisition and long-term performance', *Cognitive Brain Research*, 8(3), pp. 185–201. doi: 10.1016/S0926-6410(99)00020-8.

WHO (2006) *Neurological disorders: Public health challenges*. World Health Organization.

Womelsdorf, T. *et al.* (2021) 'A Kiosk Station for the Assessment of Multiple Cognitive Domains and Cognitive Enrichment of Monkeys', *Frontiers in Behavioral Neuroscience*, 15(August), pp. 1–13. doi: 10.3389/fnbeh.2021.721069.

Yang, X. *et al.* (2018) 'A novel mechanism of memory loss in Alzheimer's disease mice via the degeneration of entorhinal-CA1 synapses', *Molecular Psychiatry*, 23(2), pp. 199–210. doi: 10.1038/mp.2016.151.

Yao, Z. and Yazdan-Shahmorad, A. (2018) 'A Quantitative Model for Estimating the Scale of Photochemically Induced Ischemic Stroke', *Conf Proc IEEE Eng Med Biol Soc*. 2018/11/18, 2018(C), pp. 2744–2747. doi: 10.1109/EMBC.2018.8512880.

Yazdan-Shahmorad, A. *et al.* (2013) 'A novel technique for infusion of optogenetics viral vectors in nonhuman primates (NHPs) cortex using MR-guided convection enhanced delivery (CED)', *6th International IEEE EMBS Conference on Neural Engineering*, 14(415), p. Nov 5-8.

Yazdan-Shahmorad, A. *et al.* (2015) 'Demonstration of a setup for chronic optogenetic stimulation and recording across cortical areas in non-human primates', *SPIE BiOS*, 9305(March 2015), p. 93052K. doi: 10.1117/12.2080405.

Yazdan-Shahmorad, A *et al.* (2016) 'A Large-Scale Interface for Optogenetic Stimulation and Recording in Nonhuman Primates', *Neuron*, 89(5), pp. 927–939. doi: 10.1016/j.neuron.2016.01.013.

Yazdan-Shahmorad, Azadeh *et al.* (2016) 'A Large-Scale Interface for Optogenetic Stimulation and Recording in Nonhuman Primates', *Neuron*. Elsevier Inc., 89(5), pp. 927–939. doi: 10.1016/j.neuron.2016.01.013.

Yazdan-Shahmorad, A., Silversmith, D. B., *et al.* (2018) 'Targeted cortical reorganization using optogenetics in non-human primates', *Elife*. 2018/05/29, 7, pp. 1–21. doi: 10.7554/eLife.31034.

Yazdan-Shahmorad, A., Tian, N., *et al.* (2018) 'Widespread optogenetic expression in macaque cortex obtained with MR-guided, convection enhanced delivery (CED) of AAV vector to the thalamus', *J Neurosci Methods*. 2017/10/19. Elsevier B.V., 293, pp. 347–358. doi: 10.1016/j.jneumeth.2017.10.009.

Yazdan-Shahmorad, A, Silversmith, D. B. and Sabes, P. N. (2018) 'Novel techniques for large-scale manipulations of cortical networks in non-human primates', *Conf Proc IEEE Eng Med Biol Soc*. 2018/11/18, 2018, pp. 5479–5482. doi: 10.1109/EMBC.2018.8513668.

Yazdan-Shahmorad, Azadeh, Silversmith, D. B. and Sabes, P. N. (2018) 'Novel techniques for large-scale manipulations of cortical networks in non-human primates', *Conf Proc IEEE Eng Med Biol Soc*. 2018/11/18, 2018, pp. 5479–5482. doi: 10.1109/EMBC.2018.8513668.

Yin, M. *et al.* (2014) 'Wireless Neurosensor for Full-Spectrum Electrophysiology Recordings during Free Behavior', *Neuron*, 84(6), pp. 1170–1182. doi: https://doi.org/10.1016/j.neuron.2014.11.010.

Yizhar, O. *et al.* (2011) 'Optogenetics in neural systems', *Neuron*. 2011/07/13. Elsevier Inc., 71(1), pp. 9–34. doi: 10.1016/j.neuron.2011.06.004.

Zanos, S. *et al.* (2011) 'The Neurochip-2: An Autonomous Head-Fixed Computer for Recording and Stimulating in Freely Behaving Monkeys', *IEEE Transactions on Neural Systems and Rehabilitation Engineering*. IEEE, 19(4), pp. 427–435. doi: 10.1109/TNSRE.2011.2158007.

Zaraza, D. *et al.* (2020) 'Going wireless: an optical imaging and optogenetics system for use in awake behaving primates', 1122705(February). doi: 10.1117/12.2546289.

Zátonyi, A. *et al.* (2018) 'Functional brain mapping using optical imaging of intrinsic signals and simultaneous high-resolution cortical electrophysiology with a flexible, transparent microelectrode

array', *Sensors and Actuators, B: Chemical*, 273(June), pp. 519–526. doi: 10.1016/j.snb.2018.06.092.

Zhou, J. *et al.* (2022) 'Neuroprotective Effects of Electrical Stimulation Following Ischemic Stroke in Non-Human Primates *', *IEEE EMBC*, 119395, pp. 1–4.

Zola, S. M. *et al.* (2000) 'Impaired recognition memory in monkeys after damage limited to the hippocampal region', *Journal of Neuroscience*, 20(1), pp. 451–463. doi: 10.1523/jneurosci.20-01-00451.2000.